Precise Three-dimensional Positioning of Spacecrafts by Multi-frequency VLBI and Doppler Measurements

Doctor of Philosophy

Yusuke Kono

Department of Astronomical Science
School of Mathematical and Physical Science
The Graduate University for Advanced Studies

2002

Abstract

The study on orbital motion and the interior structure of the Moon and planets is one of the methods to approach for the revolution as a dynamical system and the origin of the solar system. It is a powerful method to measure the gravity fields obtained by the orbital motion of a spacecraft in order to estimate the inner layer and the density structure of the Moon and the planets. Orbits or positions of spacecrafts have mainly been determined by range and Doppler measurements. These measurements provide only one-dimensional information about the position along the line of sight. On the other hand, differential VLBI (Very Long Baseline Interferometry) has the sensitivity of positioning in direction perpendicular to the line of sight, so that combining both range and Doppler measurements with differential VLBI enables us to measure three-dimensional position of a spacecraft.

VLBI methods have been used for positioning of spacecrafts since 1960's. In these methods, carrier waves were transmitted from a spacecraft because of saving its transmitting power and obtaining high SNR. Unfortunately, the phase delay of a carrier wave, however, has cycle ambiguity, therefore only phase delay rate has been mainly used so far. If plural carrier waves at different frequencies are transmitted from a spacecraft, the group delay among the plural carrier waves enables us to resolve the cycle ambiguity of the phase delay. There is an example which used two carrier waves 6.5MHz apart transmitted from the spacecraft of the Venus. A group delay between the two frequencies was only determined, in other words, bandwidth synthesis of only two frequencies was first conducted in this experiment. This method was almost same as the one of conventional VLBI. The accuracy of positioning was about 10 km for about 1 AU distance. In addition, the ionospheric effect could not be corrected because the two carrier waves were in the same frequency band. We propose a new VLBI method, "multi-frequency VLBI". The system transmits three frequency signals in S-band and one signal in X-band. These frequencies are set to resolve the cycle ambiguity from several group delays and to correct the ionospheric effect. In this system, the phase delay of RF signals at S and X-band can be estimated, so that the accuracy of positioning can be drastically improved by a factor of 1300 (8.4GHz/6.5 MHz) comparing the mission of the Venus. The author derived several conditions of the realization of this method. He also developed a ground VLBI system, software to estimate the phase delay and an interface with the software of the gravity field and orbit estimation.

The preliminary experiment was carried out by using Lunar Prospector of NASA. Unfortunately it transmitted only one carrier wave, so that the test for resolving the ambiguity of the fringe phase could not be achieved. The residual fringe phases after the correction for the ionospheric delay have systematic variations of about 1000 deg. with period of about one hour. These variations are supposed to be caused by the errors in the initial orbital elements and model errors of the lunar gravity fields used. Although these long period variations can not be estimated in this experiment, they will be estimated in SELENE mission by multi-frequency VLBI. The short period variations of the residual fringe phases will remain even if these two errors are estimated. In this point of view, the short period variations mean the potential in an accuracy of the system. The RMS of the residual fringe phases averaged for several ten seconds reaches about 4 deg., which corresponds to 1.5 m in the positioning error around the Moon. It is confirmed that the hardware and software system have enough availability to achieve the expected accuracy in "Multi-frequency VLBI".

In the study of the Doppler measurements, we pointed out that the spin and the phase pattern of the antenna considerably affect the Doppler measurements and these effects must be removed from the observed Doppler frequency data for a precise gravity determination. We analyzed the Doppler data of the spin stabilized satellite, "Nozomi" and detected the effects of the spin and the phase pattern of the antenna for the first time. Furthermore, we developed a new method to remove the effects, and confirmed the validity of this method.

Because the VLBI system uses narrow bandwidth signals and the amount of the data is much less than those in conventional one, the system has a potential of real time VLBI through the INTERNET. This means that the system can be widely used in real time positioning of various spacecrafts.

Table of Contents

Chapter 1

Introduction

1.1 Short history of positioning of spacecrafts by VLBI and Doppler tracking

Gravity fields of planets and the Moon are obtained by observations of the orbits and their time variations of spacecrafts flying around the center bodies. The gravity field of the Moon has been investigated since 1966. Russian Luna 10 was placed in orbit around the Moon and provided dynamical proof that the oblateness of the Moon's gravitational potential was static equilibrium [Akim et al., 1966]. Thereafter a lot of spacecrafts explored the gravity fields until the latest lunar explore, Lunar Prospector [Konopliv et al., 1998]. The gravity fields have been estimated by the observations of orbits or position of the spacecrafts by using range and Doppler measurements. Doppler methods measure range rate or line-of-sight velocity between a spacecraft and a ground station on the Earth. Range methods measure range between a spacecraft and a ground station on the Earth. Range measurements are useful to operate spacecrafts. Because their accuracies, however, are worse than that of Doppler measurements, they do not play important role in estimations of the lunar gravity fields. The lunar gravity fields have been estimated by Doppler measurements which are one-dimensional measurements.

VLBI is one of the most powerful methods for positioning the spacecrafts in high resolution [Counselman et al., 1973]. A simple VLBI positioning system is basically composed of two radio telescope antennas receiving electmagnetic signals from spacecrafts and a cross correlation system (see Figure 1.1). The cross correlation system derives ideally a geometric delay which is time difference between the arrival times of the same radio signal at two VLBI stations. The delay observable is sensitive to the direction of the baseline. If two or more baselines are configured rectangularly to line-of-sight direction to the spacecrafts, the VLBI system can measure the positions of spacecrafts in two-dimension

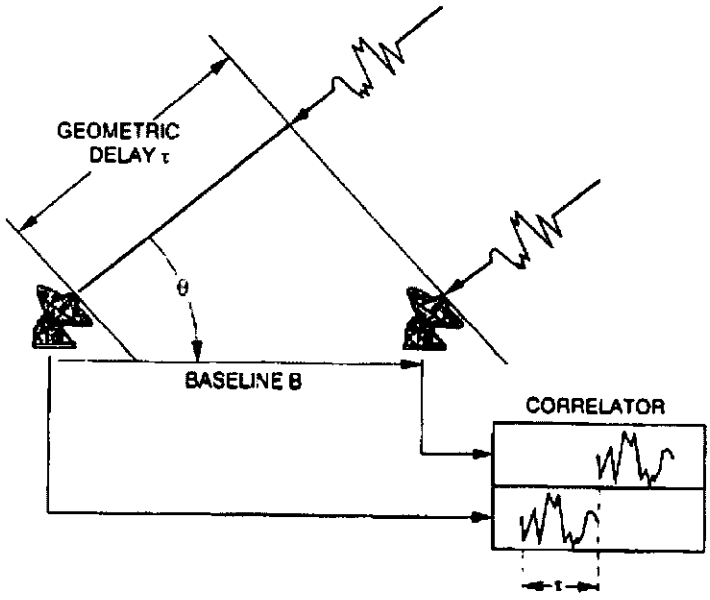

Figure 1.1: Principles of VLBI

[Heki et al., 1999, Kawano et al., 2000]. An actual cross correlation system produces time series of a complex quantity, fringe. It is composed of amplitude and phase called fringe phase. This fringe phase ϕ can be written in brief, as

$$\phi = 2\pi f \tau \tag{1.1}$$

where, f is the received frequency. τ is the time difference between the arrival times at two stations. The phase delay cannot directly be derived as,

$$\tau = \frac{\phi}{2\pi f} \tag{1.2}$$

because the fringe phase has 'integer cycle ambiguity', i.e., offset that is multiple of 2π. Several methods have been proposed to escape from the problem of the cycle ambiguity.

One of the methods is to measure the group delay of the radio signals in widening spectrum transmitted from spacecrafts [Border et al., 1982, Shiomi et al., 1984]. The group delay is obtained by differentiation of fringe phase with respect to frequency as follows,

$$\tau = \frac{1}{2\pi}\frac{\partial \phi}{\partial f} \tag{1.3}$$

A disadvantage of this method is that the accuracy of the group delay is worse than that of phase delay by a factor of f/B, where f is the mean received frequency

in the received frequency bandwidth B [Takahashi et al., 2001]. In order to improve the delay accuracy by widening the transmitting spectrum, more electrical resources of the spacecraft are required.

Another method is to track the fringe phase obtained by observations of one carrier wave. This method is only available to determine the position of a radio source placed on the Moon or a planet. As an example, ALSEP (Apollo Lunar Surface Experiments Packages) mission tracked the fringe phase of the carrier signal at S-band transmitted from ALSEP on the Moon [King et al., 1974, Counselman et al., 1973]. Another example is an observation of Magellan and Pioneer12 orbiters which tracked the fringe phase of the carrier signals in S-band and X-band transmitted from the Venus orbiters [Border et al., 1992]. All of these missions did not solve the cycle ambiguities.

Two missions to use plural carrier waves have been proposed so far. One method used two carrier waves 6.5 MHz apart at L-band [Sagdeyev et al., 1986, Sagdeyev et al.,1992]. The other method proposed to use two carrier waves 40 MHz apart at X-band [Edwards et al., 1990, Edwards et al., 1992]. This mission , however, was not carried out in actual. In both cases, actually the cycle ambiguities of the carrier signals have not been solved at all. The group delays between two carrier signals have been obtained.

The multi-frequency VLBI was proposed to solve this problem [Kawano et al., 1994, Hanada et al., 1999]. In the method, three carrier waves at S-band and one at X-band are transmitted from spacecrafts. The group delays obtained from the three frequencies at S-band contribute to resolve the cycle ambiguity of the carrier signal at X-band. The configuration of the frequencies of the carrier waves is optimized to resolve the cycle ambiguity.

1.2 Purpose and significance of this thesis

The objective of this thesis is to realize the precise three-dimensional positioning of spacecrafts. The study in this thesis can be separated to two parts. One is the research in the multi-frequency VLBI. The other is the research in the Doppler measurement.

The multi-frequency VLBI which measures the phase delay accurately without the cycle ambiguity has been proposed so far [Kawano et al., 1994, Hanada et al., 1999]. These works have shown only the idea or possibility of the multi-frequency VLBI roughly. They have not discussed the conditions to resolve the cycle ambiguity of the carrier waves under actual conditions about the radio transmitters, the ionospheric fluctuation and so on. This thesis proposes the multi-frequency VLBI

under the actual conditions about them. The conditions to realize the cycle ambiguity resolvent of the carrier waves are shown in this thesis. The ground system of the multi-frequency VLBI has also been developed. The system consists of the hardware to sample and record the carrier waves, the software to estimate phase delays and an interface with the software of gravity fields and orbits estimation. In order to test the whole system which has been developed, a preliminary experiment of multi-frequency VLBI is carried out by using Lunar Pospector.

Doppler method is carried out by measuring the frequency variation of the radio signal from a spacecraft. It has been widely used for positioning of spacecrafts so far. As the latest example, 2-way Doppler measurements has been carried out in the Lunar Prospector mission [Konopliv et al., 1998]. The accuracy of the measurement reached 0.3 mm/s in range rate in every 10 seconds. In SELENE project, the accuracy of the Doppler measurement is expected to be 0.1mm/s for every 10 seconds of sampling interval so as to study the lunar gravity field more precisely. We point out seven error sources which are the Earth's ionosphere, the Earth's troposphere, a spin of a spacecraft, a phase radiation pattern of an antenna, attitude of a spacecraft, instability of a transponder and instability of a frequency standard. In particular, the effects caused by the spin of a spacecraft and phase pattern of an antenna have not been discussed so far. There are some discussions about the effects of spin of a spacecraft on Doppler measurements [e.g., Marini 1972, Milani et al., 1996, Weischede et al., 1999, Konopliv et al., 2001]. However, the effects of combinations of the spin and the antenna phase pattern have not discussed yet. In this thesis, the method to remove the effects is proposed.

1.3 Application of Multi-frequency VLBI and the improved Doppler measurement to Lunar science

The Moon has been stimulating scientist's interests as the most familiar planetary body in the solar system. Since 1950's, the Moon has been explored repeatedly by unmanned and manned missions. Especially, the Apollo and Luna programs have provided a lot of new findings about the Moon and brought about a significant progress in the field of lunar science. In addition, there were two interesting missions in 1990's, using advanced observation technologies. The American lunar orbiters, Clementine launched in 1994 and Lunar Prospector launched in 1998, also made great contributions to lunar science.

For the origin of the Moon, four major models have been proposed. These are 1)

fission of the Earth, 2) capture of the Earth, 3) binary accretion, and 4) accretion by giant impact. These theories state, briefly, that 1) the Moon was spun out of the Earth's crust and/or asthenosphere during an early era of rapid rotation of the Earth; 2) the Moon was formed elsewhere and captured later by the Earth's gravitational field; 3) the Earth-Moon system grew up together out of a primordial swarm of small planetesimals; 4) the Moon was formed from debris thrown into space following a collision between an early-stage Earth and a Mars-sized object [e.g., Hartmann and Davis 1975, Cameron and Ward 1976]. Although the giant impact model is the most widely accepted [e.g., Russell et al.,1981, Cameron 1997] in order to address the question concerning the origin of the Moon, further exploration is required more elaborately than before as for the constitutional materials, interior structure and magnetic fields. For example, the information of the interior structure gives constraints to the model of the origin. If we assume the Moon was produced by accretion of the primitive meteoroids, then the radius of the core of the Moon is estimated to be larger than 360 km to explain the material of the abundance of metal in the lunar rocks. On the other hand, if the Moon was made of the same material of the Earth's mantle, the radius of the core must be less than 285 km [Ferrari et al., 1980]. In order to discuss the radius and the density of the core and the interior of the Moon, the moment of inertia plays an important role, because density distribution of a planet is directly reflected in the moment of inertia. For example, a sphere with uniform density has a normalized moment of inertia of $C/MR^2 = 0.4$ where R, M and C are the radius, the mass and the moment of inertia of the sphere, respectively, and the sphere with $C/MR^2 < 0.4$ means that density of the center is higher than that of the outside. To obtain the moment of inertia of the Moon, the observations of the lunar gravity field and the dynamic flattening are useful. There are relations among the stokes coefficients (C_{20} and C_{22}) and the dynamic flattening (β and γ) as follows,

$$C_{20} = \frac{1}{MR^2}\Big(\frac{A+B}{2} - C\Big), \tag{1.4}$$

$$C_{22} = \frac{1}{4MR^2}(B-A), \tag{1.5}$$

$$\frac{4C_{22}}{\gamma} = \frac{C}{MR^2}, \tag{1.6}$$

$$\frac{2C_{20}(1+\beta)}{\gamma - 2\beta - \beta\gamma} = \frac{C}{MR^2}, \tag{1.7}$$

where A, B, C ($A < B < C$) are the moments of inertia around the principal axis of the Moon [Ferrari et al., 1980], and $\beta = (C-A)/B$ and $\gamma = (B-A)/C$, respectively. Accuracies of the moments of inertias of the Moon depend on the accuracies of the stokes coefficients and the dynamic flattening. At present, the

accuracies of the stokes coefficients are worse than those of dynamic flattening by one order[Hanada et al., 2000]. For this reason, the improvement of the stokes coefficients of the lunar gravity field contributes to improve the moment of inertia of the Moon.

Observations of the lunar gravity field by the precise three-dimensional positioning of spacecrafts using multi-frequency VLBI and Doppler measurements which are presented in this thesis will be carried out in SELENE project. Simulations show that the new observations will improve the lunar gravity model, including the low degree harmonics of the lunar gravitational fields, by more than 1.5 orders (see Figure 1.2). Although the improvement of the moment of inertia of the Moon will be limited by the accuracies of the dynamic flattening after SELENE project, the improvement will be one order. To set the limitation free, another observation of the dynamic flattening are expected. The In-situ Lunar Orientation Measurement (ILOM) mission, which is a small optical telescope mission, is proposed as a post-SELENE project [e.g., Takanezawa et al., 2000]. The improvement of the moments of inertia of the Moon in one order enables precise discussions of density of the lunar core if the radius of the core and depth and density of the crust are assumed [Hanada et al., 2000]. According to this study, the improvement of the moment of inertia enables to discuss the density of the core within the accuracy of 500 kg/m^3 from 2000 kg/m^3 at present (see Figure 1.3 and Figure 1.4) and to give a strong constraint of the core.

1.4 Brief summary of the content

In Chapter 2, a method to improve accuracy in the Doppler measurement is discussed. It is pointed out that spin and a phase pattern of an antenna considerably affect the Doppler measurements and the effects must be removed from the observed Doppler frequency data for the precise lunar gravity field estimation. As a practical application, the Doppler data from a spin stabilized satellite, "Nozomi" is analyzed , and the effects of the spin and the phase pattern of the antenna are detected for the first time. Furthermore, a new method is proposed to remove the effects from observed Doppler frequency data, and the validity of the method.

In Chapter 3 a new VLBI method, multi-frequency VLBI, and its theory to derive the phase delay from observed raw data are presented. Several conditions about frequency, its variation of the radio transmitter and the ionospheric condition for realization of this method are also discussed in this chapter.

In Chapter 4 an application of the multi-frequency VLBI to the actual lunar mission (VRAD: Vlbi RADio source) is described. The developed ground sys-

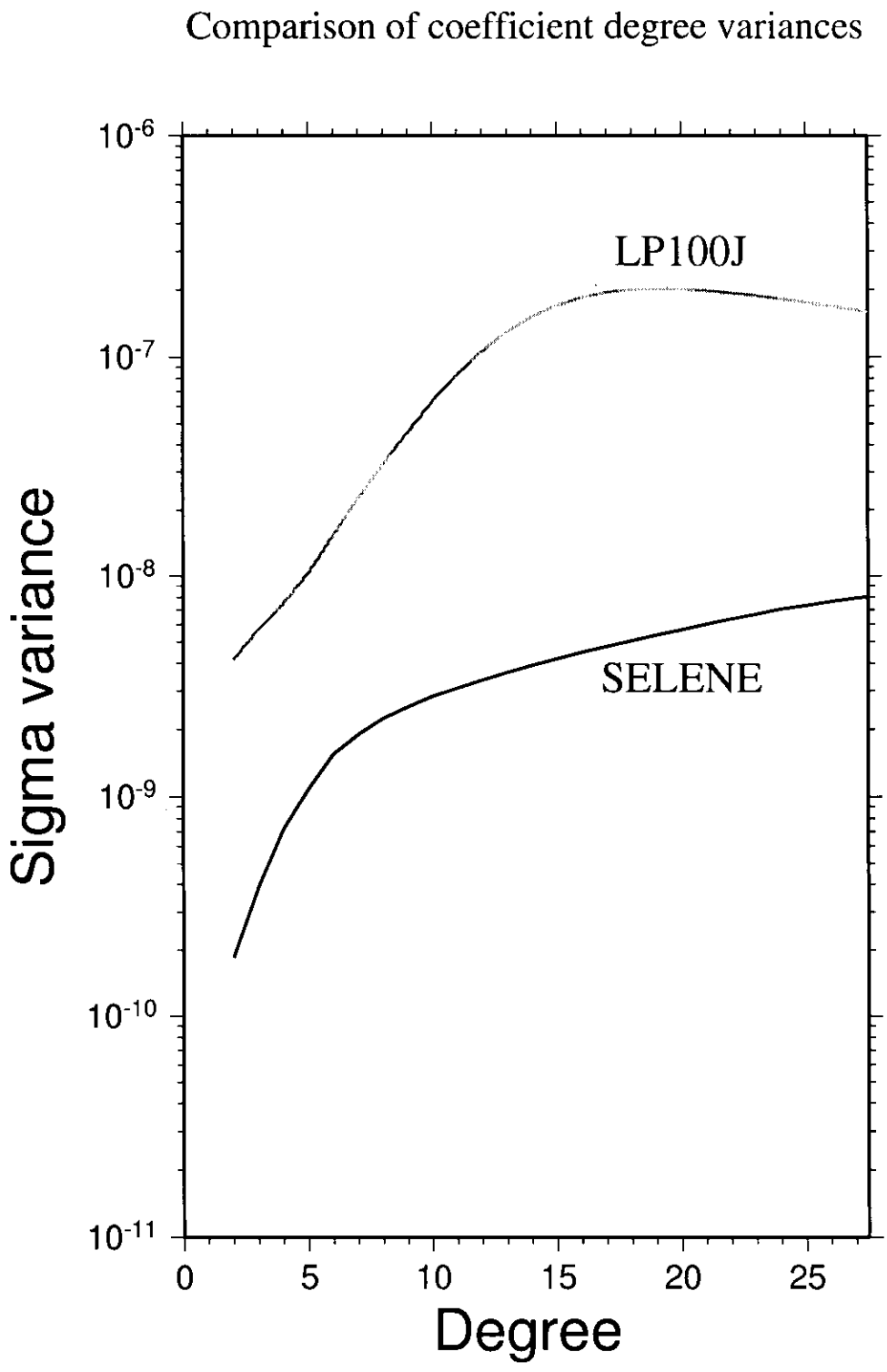

Figure 1.2: Coefficient sigma variances of the lunar gravity fields

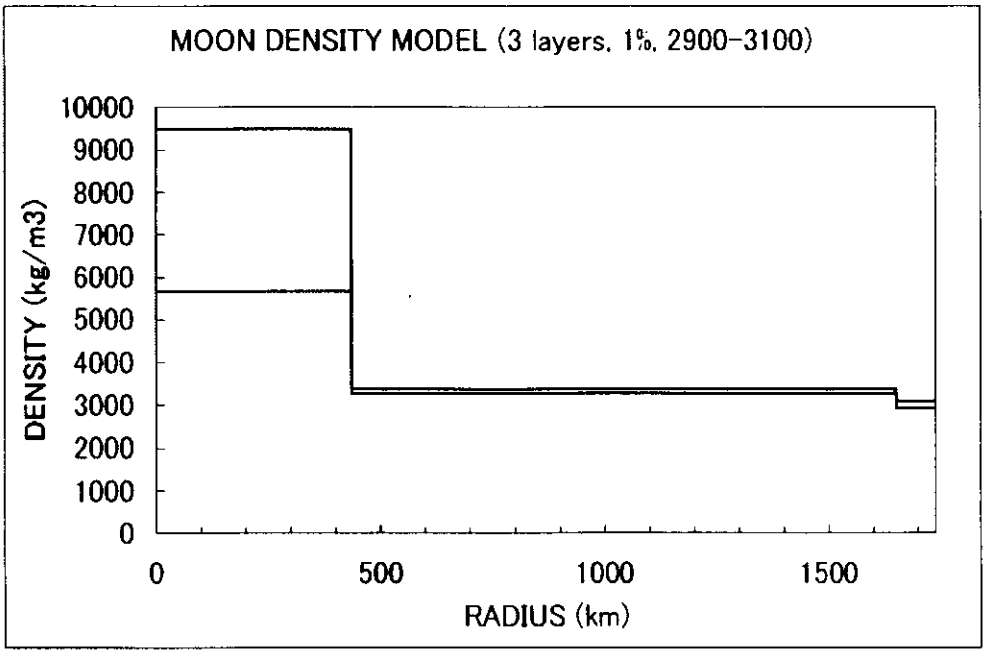

Figure 1.3: A three-layer density model of the Moon constrained by moment inertia of 0.1 % accuracy. Crustal depth and core radius are supposed to be 2.9g/cm^3 $\sim$ 3.1g/cm^3, 55 km and 450 km, respectively.

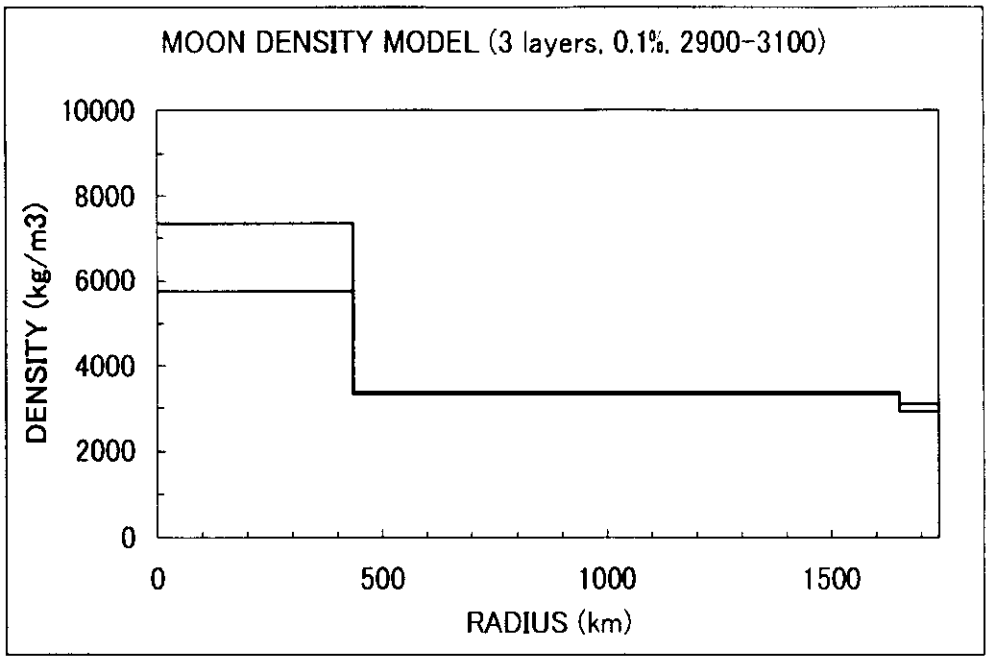

Figure 1.4: A three-layer density model of the Moon constrained by moment inertia of 1.0 % accuracy. Crustal depth and core radius are supposed to be 2.9g/cm^3 $\sim$ 3.1g/cm^3, 55 km and 450 km, respectively.

tem which consists of the narrow-bandwidth recording system and phase delay estimation software is also described.

In Chapter 5, the VLBI observation of Lunar Prospector as a preliminary experiment of the multi-frequency VLBI is described. In particular, the validity of the ground system which is developed in this study is investigated. As a result of this experiment, residual fringe phases from predicted ones are also discussed.

In Chapter 6, the concluding remarks and expected applications of the developed ground system are described.

Chapter 2

Improvement of the accuracy of Doppler measurements

2.1 Error sources of Doppler measurements and short period variations of Doppler frequency caused by spin of an antenna

An integrated Doppler measurement (see, Appendix A1) is one of the major methods of positioning of spacecrafts in space. In order to study the lunar gravity field precisely, SELENE project measures the Doppler frequency of the spacecraft with an accuracy of 0.7mHz in S-band or of 0.1mm/s in range rate every few tens seconds of sampling interval. This accuracy is the highest one in measurements that have ever been carried out so far. Here we summarize the error sources of Doppler measurements that exceed the accuracy of 0.1mm/s.

- Fluctuation of a propagation delay caused by the ionosphere
- Fluctuation of a propagation delay caused by the troposphere
- Frequency instability of a transmitter on a ground station
- Phase instability of a transponder in a spacecraft
- Phase variation caused by a phase pattern of an antenna on a spacecraft
- Doppler frequency variation caused by spin of a spacecraft
- Attitude variation of a spacecraft

Although all error sources should be carefully considered, the first four sources have ever been discussed. However the last three error sources have never discussed in

detail. Hereafter we discuss the two error sources of the phase pattern of an antenna on a spacecraft and the spin of a spacecraft.

Attitudes of many spacecrafts are spin-stabilized. They have sometimes a crossed dipole antenna or a micro strip antenna on board for Doppler measurements. The antennas have complicated phase pattern in general. The rotation of such a phase pattern of the antenna on a spin-stabilized satellite affect phase of a transmitting or receiving signal as well as Doppler measurements. Furthermore the phase center of the antenna cannot be placed just on the spin axis and this displacement also affects the Doppler measurements [Ping et al., 2000, Marini 1972].

2.2 Analysis of short period variations of Doppler frequency caused by spin of an antenna

2.2.1 Relationship between an integrated Doppler measurement and its sampling frequency

Before a discussion on the effect of spin and a phase pattern, we discuss the integration time that is equivalent to the sampling period of Doppler measurements. The integration time in the Doppler measurement limits the maximum degree of spherical harmonics expansion of the gravity field to be estimated. In the case of 4-way Doppler measurements [Namiki et al., 1999] in SELENE project, the lunar gravity field up to at least 100th degree in spherical harmonics expansion will be estimated precisely. Because the 100th degree gravity field corresponds to about 100km spatial wave length on the Moon and the spacecraft of SELENE flies over the Moon at the speed of 1.7km/s, the integration time of Doppler measurements must be less than 30 seconds. For this reason, the integration time is set to 10 seconds in SELENE project.

2.2.2 Antenna phase pattern and short period variation and its harmonics

An antenna phase pattern shows the phase dependence of a signal in the direction of transmission. This is equivalent to the movement of a phase center of an antenna in the transmitting direction. In the case of a spin-stabilized satellite, displacement of the average phase center of an antenna from the spin axis causes the Doppler variation at the spin frequency, and the phase pattern also causes Doppler variations at the spin frequency and at its harmonics [Ping et al., 2000].

These Doppler frequency variations are mixed with observed Doppler frequency variations by the lunar gravity field. If the twice sampling frequency of the Doppler measurement is lower than the frequency of the Doppler variations, the spin frequency and its harmonics variations are folded in the frequency bandwidth of the gravity field. The folded frequency of the n-th harmonics of spin frequency is expressed as follows [Ping et al., 2000],

$$f_{fold} = \frac{f_{sa}}{N} Abs[Int[\frac{nf_{spin}}{f_{sa}} N - mN]] \tag{2.1}$$

where,

$$\begin{aligned}
f_{fold} &: Frequency\ to\ be\ folded\ as\ n-th\ harmonics \\
N &: Data\ number\ of\ FFT \\
f_{sa} &: Sampling\ frequency \\
nf_{spin} &: The\ n-th\ harmonics\ of\ spin\ frequency \\
m &: The\ number\ of\ folds \\
&= Int[\frac{nf_{spin}}{f_{sa}}] \\
Abs[\ ] &: Operator\ of\ the\ absolute\ value \\
Int[\ ] &: Operator\ of\ the\ nearest\ integer
\end{aligned}$$

2.3 Analysis of 'Nozomi' Doppler frequency

2.3.1 Estimation of frequency of the spin and its harmonics by observed Doppler frequency

'Nozomi', see Figure 2.1 [1], is a spin-stabilized spacecraft launched by ISAS of Japan to explore the Mars. A crossed dipole antenna is used for link to the Earth. Figure 2.2 shows an integrated Doppler frequency observed at Kagoshima Space Center in Aug. 27, 1998. During this observation 'Nozomi' were orbiting around the Earth.

In order to detect Doppler frequency variations caused by a phase pattern and spin in the Doppler frequency data, several steps of data processing are taken. In Figure 2.2 a increase of the Doppler frequency over whole period is predominant and shows orbital motion around the Earth. At first we removed the increase of the Doppler frequency by the approximation of 5-order polynomials, and we get the short period variation of Doppler frequency as shown in Figure 2.3. By the

[1] http://www.isas.ac.jp/e/enterp/missions/nozomi/

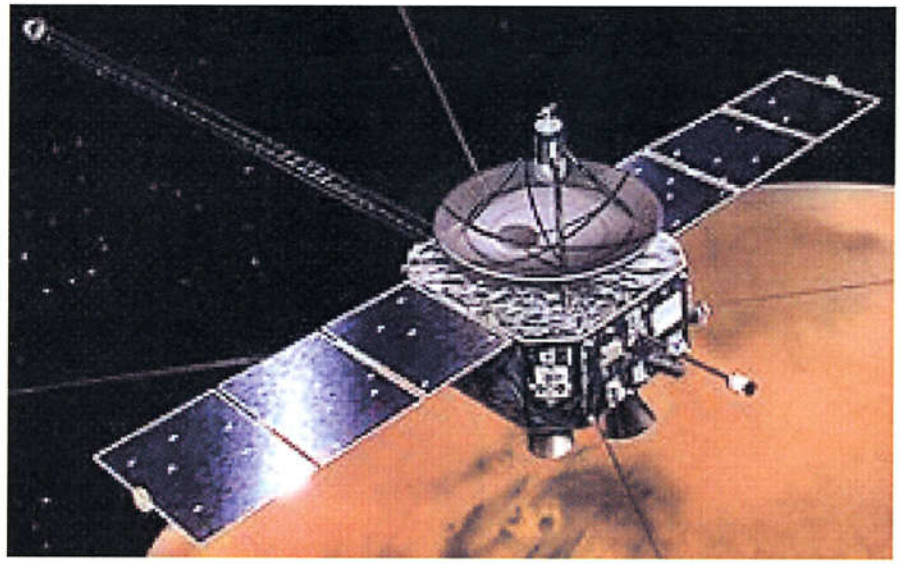

Figure 2.1: Mars spacecraft, 'Nozomi'

Fourier transformation of this variation, we find four peaks in the spectrum in Figure 2.4. Because these frequencies of the peaks are absolutely constant all over the two hour observation, these peaks are expected to be the effect of the phase pattern of the antenna on 'Nozomi'.

The spin period of 'Nozomi' has been known previously to be from 6 to 7 seconds by the design of the spacecraft and telemetry. Doppler data obtained at the integration time of less than 3 seconds is desirable according to the sampling theory. We, however, have only the data at the integration time of 4 seconds. The spin frequency and its harmonics would be folded in the observation bandwidth shown in Figure 2.4 so that we cannot know the real spin frequency directly from the Doppler data. Assuming that the frequencies of the four peaks described by the relationship of Equation (2.1), we try to estimate the spin frequency. Firstly, we assume that the spin frequency results in the highest peak at 0.0931Hz by folding. Substituting $f_{obs} = 0.0931$, $n = 1$ and $m = 1$ into Equation (2.1), we have

$$0.0931 = \frac{0.25}{2048} Abs[Int[\frac{1 f_{spin}}{0.25} \times 2048\text{–}2048]] \tag{2.2}$$

$$f_{spin} = 0.1567\ [Hz] \tag{2.3}$$

$$1/f_{spin} = 6.382\ [sec.]. \tag{2.4}$$

This result of the spin period is consistent with the predicted one from the design and the telemetry. Assuming this value of the spin frequency, Equation (2.1) gives us all the harmonics of the spin frequency. The results are shown in Table 2.1. All

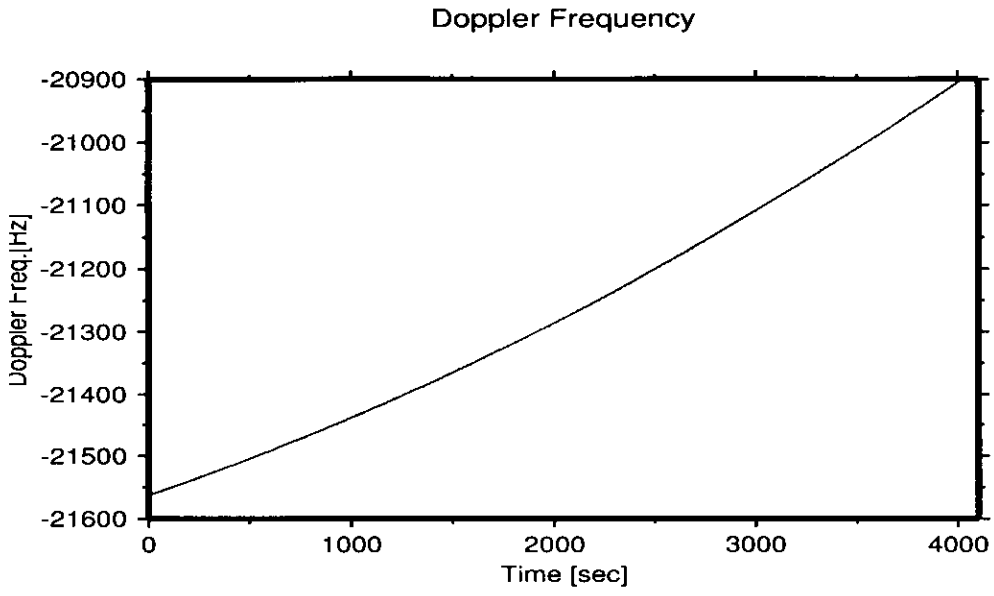

Figure 2.2: Doppler frequency observed at Kagoshima Space Center. Increase with time shows a Doppler frequency variation by orbital motion around the Earth.

the calculated frequency from Equation (2.1) is equal to the observed frequency of the peak in the spectrum within the observation error.

We have assumed that the spin frequency results in the highest peak by folding so far. However the spin frequency results in another peak by folding. Then we assume that the spin frequency results in the second highest peak at 0.0634Hz by folding. The folded frequencies of the harmonics are shown in Table 2.2 in the case. In the same way, the other cases are shown in Tables 2.3 and 2.4, respectively. Comparing the four results, it is clear that only the first case is consistent with the observed frequency. Therefore we decide that the highest peak is the spin frequency folded in observation bandwidth, and the spin frequency is 0.1567 Hz.

Some features of the amplitude can be found in Figure 2.4. The peak of the spin frequency is the highest, and its amplitude is 0.025 Hz. This can be explained by considering that the spin frequency is caused by displacement of the average phase center of the antenna from the spin axis. Another feature is that the third order harmonics is extremely lower than the second and fourth order harmonics. This can be explained by considering that the antenna is a crossed dipole antenna that is a combination of two dipole elements, and therefore the even order harmonics have large amplitude.

As the results mentioned above, we detected the effects of the phase pattern of

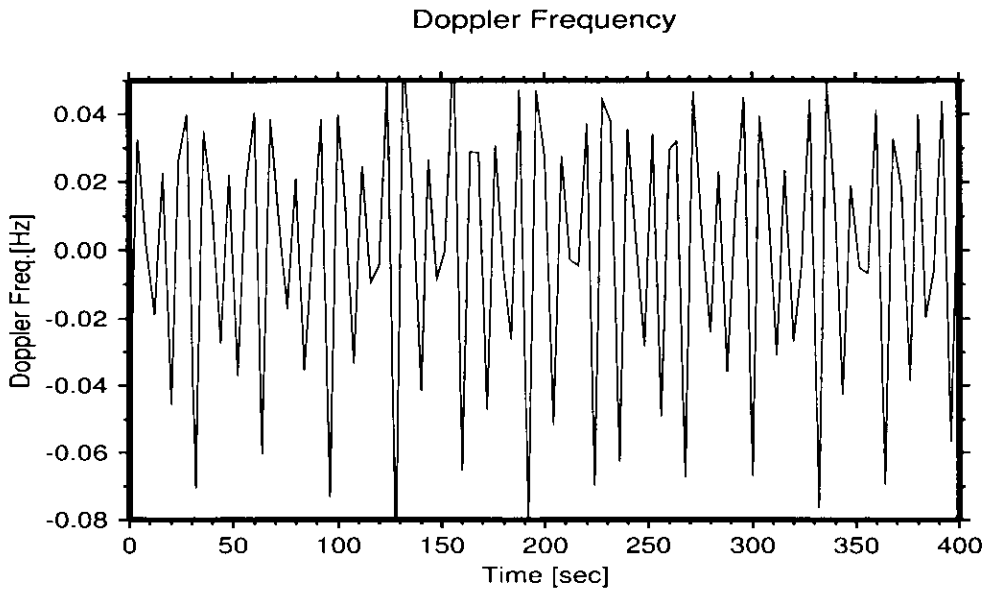

Figure 2.3: Residual of Doppler frequency subtracted by 5-order polynomials. The short period variations are found in this figure

the antenna and spin in the Doppler data of 'Nozomi'. These effects appear as four harmonics of the spin frequency, and the amplitudes exceed that of the expected accuracy of the lunar gravity field in SELENE project.

2.4 Proposal of a new method to remove the effect of spin

As the results of data processing described in the former section, a phase pattern of an antenna and spin actually affect Doppler frequency beyond the expected accuracy. Hereafter, we propose a method to remove the harmonics from the low frequency band of which variations caused by the lunar gravity field and show the validity of the method by using the 'Nozomi' Doppler data.

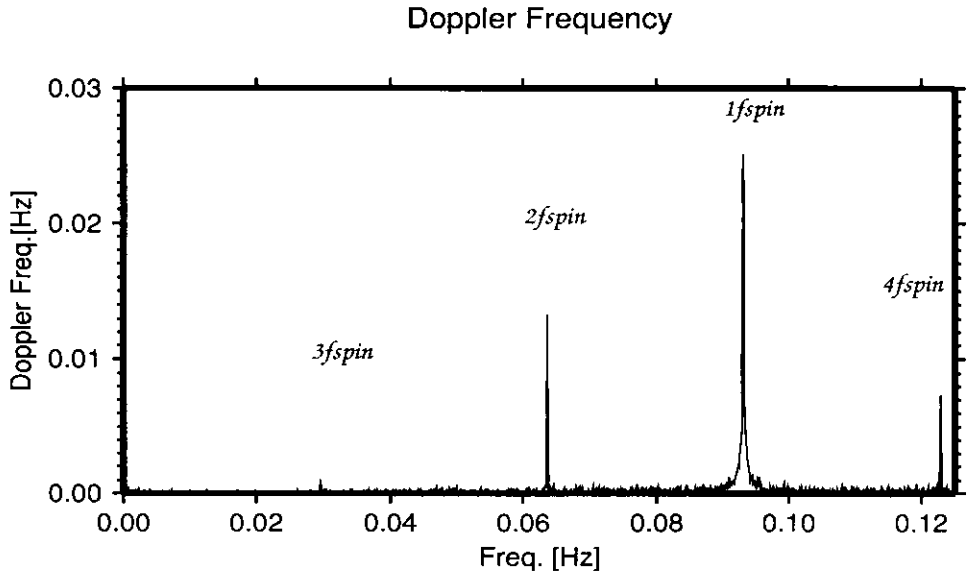

Figure 2.4: Spectrum of residual Doppler frequency subtracted by 5-order polynomials. Four peaks appear in this spectrum.

2.4.1 Frequency band of the variations caused by the lunar gravity field

Relationship between the effect of the spin and frequency of the gravity field information is discussed in this section. As shown in Section 2.3.1, a spin frequency and the number of harmonics can be estimated from Doppler data even if they are sampled at a certain sampling frequency lower than the spin frequency. After these estimations, we can predict the frequencies of the harmonics folded in the observation bandwidth for any sampling frequency. Figure 2.5 shows the folded frequency of the first to fourth harmonics for sampling period of 1 to 20 seconds. As shown in Figure 2.5, even if the sampling period is long, the harmonics do not disappear and fold in the observation band. The observation band can be separated into two parts. The first is lower frequency band caused by the variation of the lunar gravity field. The second is the higher frequency band which is unnecessary for the gravity estimation. The longer sampling period is, the more frequently the harmonics are folded in the lower band of the variations caused by the lunar gravity field. For example, the sampling period of 1 second generates no harmonics in the band $0 \sim 1/20$ Hz which will be used for the gravity estimation in SELENE project.

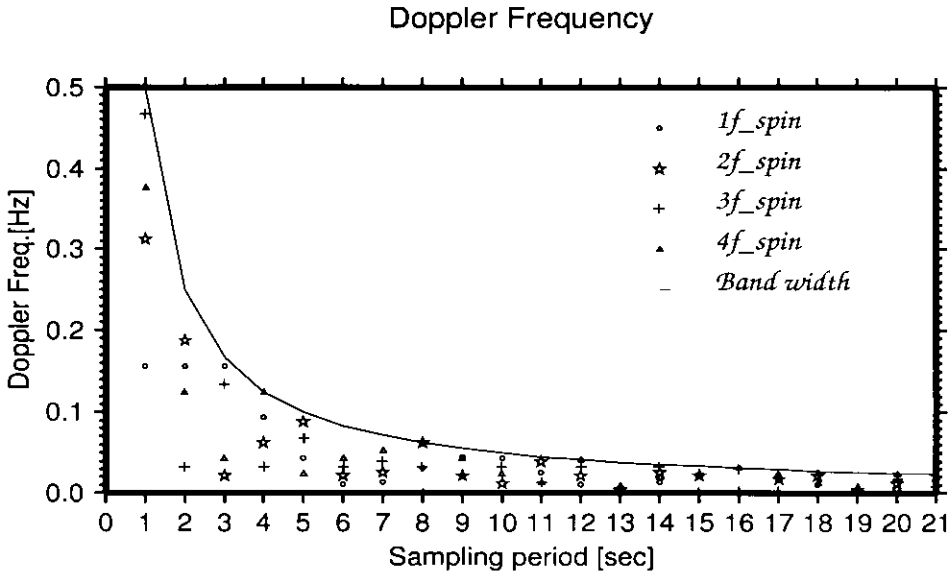

Figure 2.5: Relation between frequency of harmonics of spin frequency and sampling one. From this figure, we can predict the frequency of each harmonics of spin frequency for any sampling frequency.

2.4.2 New method to remove the effects of spin

In the case that a spin frequency is f_{spin} and a sampling frequency is higher than $2nf_{spin}$, any harmonics up to n-th order does not appears in the lower frequency band of the variation of the lunar gravity field because the spin frequency is generally higher than the lower band. Therefore, any harmonics of which frequency is nf_{spin} can be easily separated from the lower frequency band by filtering. If the spin frequency of the SELENE relay satellite is 0.25 Hz (nominal value, [Iwata et al., 2001]) and harmonics up to fourth order are generated, sampling frequency should be higher than 2 Hz. The total amount of data accumulated at a high sampling rate (for example, more than 1 Hz), however, charges too heavy burden for real-time operation of a ground station. A lower sampling rate is desirable for this reason. Then we propose a new method to remove the effects of the phase pattern and the spin, without increasing the data produced at a ground station. The method is separated in two steps. The first is determination of the most proper sampling frequency. The second is removal of the effect of the phase pattern and the spin.

Table 2.1: Calculated and observed frequencies assuming that the highest peak is yielded from the spin frequency

Estimated f_{spin}=0.1567Hz			
Order of Harmonics	Calculated Freq.[mHz]	Observed Freq.[mHz]	Cal. - Obs. [mHz]
1	93.2	93.1	-
2	63.4	63.5	-0.1
3	29.7	29.5	0.2
4	123.0	127.1	-4.1

Table 2.2: Calculated and observed frequencies assuming that the second highest peak is yielded from the spin frequency

Estimated f_{spin}=0.1863Hz			
Order of Harmonics	Calculated Freq.[mHz]	Observed Freq.[mHz]	Cal. - Obs. [mHz]
1	63.7	63.5	-
2	122.5	127.1	-4.6
3	58.8	93.1	-34.3
4	4.8	29.5	-24.6

1) Determination of the most proper sampling frequency

Firstly, a preliminary determination of the most proper sampling frequency is carried out as follows. Using observed data sampled at an arbitrary frequency, the frequencies of the spin and its n-th order harmonics are estimated at first in the same as is Section 2.3.1. We try to find out the lowest sampling frequency in which any harmonics does not appear in the lower frequency band of the gravity fields.

2) Removal of effects of the phase pattern and the spin and reconstruction of the Doppler data

Here, several processes are carried out by using the data sampled at the lowest sampling frequency mentioned above. Firstly, the main trend of long period is removed by a postfit function. The postfit residuals are Fourier-transformed, and the harmonics are removed in the spectrum which is inverse-Fourier-transformed

Table 2.3: Calculated and observed frequencies assuming that the third highest peak is yielded from the spin frequency

Estimated f_{spin}=0.2203Hz			
Order of Harmonics	Calculated Freq.[mHz]	Observed Freq.[mHz]	Cal. - Obs. [mHz]
1	29.6	29.5	-
2	59.3	63.5	-4.2
3	88.9	93.1	-4.1
4	131.3	127.1	4.1

Table 2.4: Calculated and observed frequencies assuming that the lowest peak is yielded from the spin frequency

Estimated f_{spin}=0.1273Hz			
Order of Harmonics	Calculated Freq.[mHz]	Observed Freq.[mHz]	Cal. - Obs. [mHz]
1	127.2	127.1	-
2	4.6	29.5	-24.9
3	118.0	93.1	24.9
4	9.2	63.5	-54.3

after all harmonics is removed. Next, this time-series data are added to the long period trend and corrected Doppler data without the harmonics of the phase pattern and the spin are reproduced. Finally, averaging processes are carried out in order to obtain the Doppler data sampled at the appropriate sampling frequency for the estimation of the gravity field. For example, Doppler data sampled at the period of 10 seconds are obtained by averaging of 10 Doppler data sampled every 1 second. The processes mentioned above are summarized in Figure 2.6.

2.4.3 Application of the method to 'Nozomi' Doppler data

In order to show the validity of the method mentioned in Section 2.4.2, we apply it to the Doppler data of 'Nozomi'.

We omit the first process which estimates the spin frequency and the number of harmonics since we have already known them in Section 2.3.1. Figure 2.5 indicates that some harmonics would be folded in the lower frequency band of the gravity field (here, $0 \sim 1/20$ Hz) if the sampling period was longer than 2

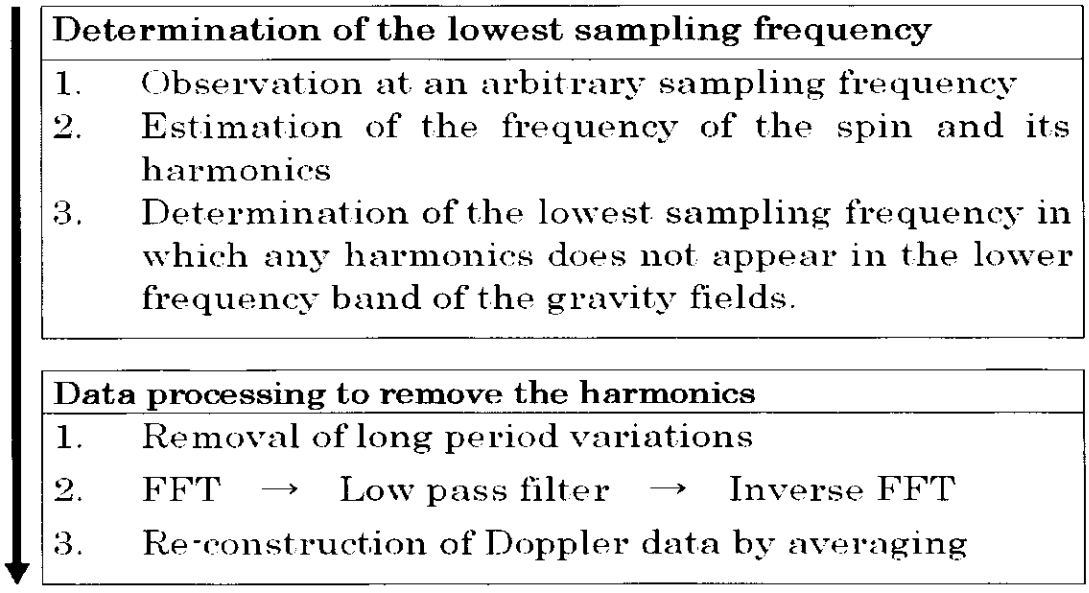

Figure 2.6: The method to remove effects of spin

seconds. This means that the proper sampling frequencies should be shorter than 1 second. We, however, can get only the Doppler data sampled every 4 seconds at present due to the restriction of the ground station. Figure 2.5 shows that Doppler data sampled every 4 seconds include only the third order harmonics of the spin frequency in the lower band of the gravity field. Fortunately the amplitude of the third order harmonics is rather small (amplitude: 0.8mHz) compared with the expected accuracy of 1 mHz, and can be negligible. Hereafter we remove the first, second and fourth order harmonics from the Doppler data sampled every 4 seconds.

Removal of the harmonics mentioned above is processed in the same way of Section 2.4.2. The main trend of long period has already been removed by a postfit polynomial and Fourier transformation has been done, in Section 2.3.1. Any spectrum outside the lower band of the gravity field ($0 \sim 1/20$ Hz) are removed from the data in frequency domain. Then, the Doppler data obtained by the inverse Fourier transformation are free from the effects of the phase pattern and the spin. Furthermore, this 4 second data are reconstructed to 12 second sampled data and 20 second sampled data by the following process. The 12 sampled seconds and 20 second sampled data are obtained by averaging 3 and 5 data, respectively. The 12 second sampling period is selected because it is close to 10 seconds which is the most appropriate sampling period for the analysis in the SELENE project. The 20 seconds sampling period is for comparison. The data obtained by the

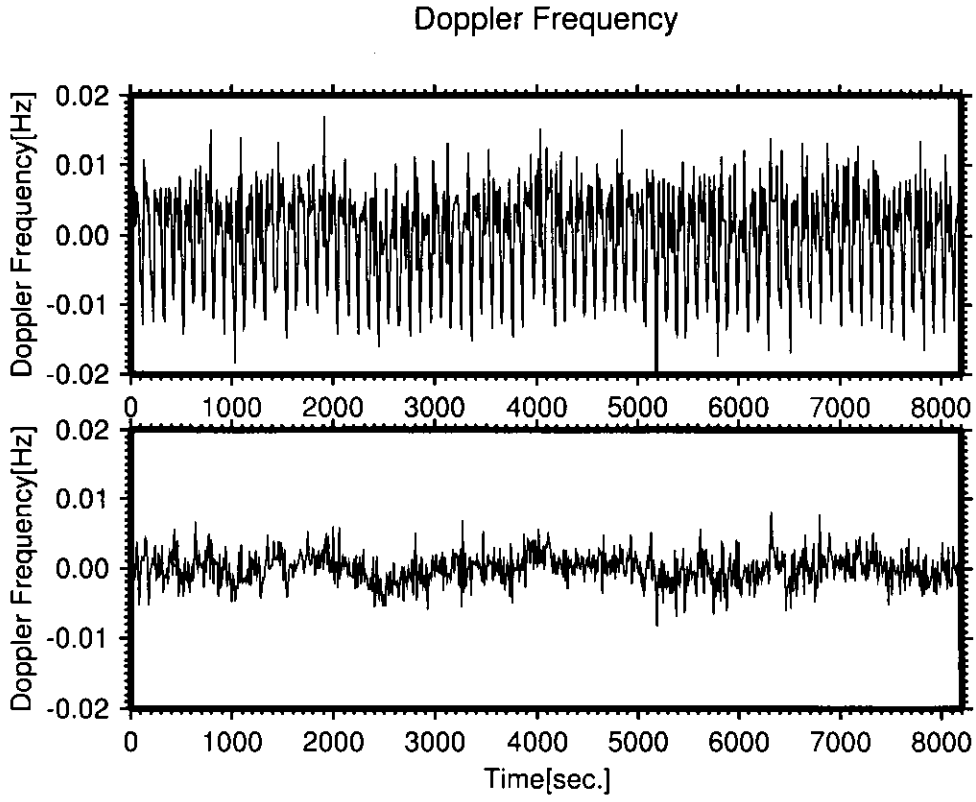

Figure 2.7: The Doppler frequency variations converted to 12 second sampled data. Upper figure: before filtering, lower figure:after filtering

processes mentioned above are shown in Figures 2.7 and 2.8. The 12 second and 20 second data obtained by the processes without the removal of the effect of the phase pattern are also shown in the same figures. Furthermore the spectra of the 12 and 20 second sampled data are shown in Figure 2.9 and Figure 2.10. It is obvious that the effects of the phase pattern and the spin can be removed in both time domain and frequency domain by the application of the method.

2.5 Limitation of spin frequency

It is essential to estimate the most proper sampling frequency in the method in Section 2.4.2. However, there is a case that some harmonics are already folded in the lower band of the gravity field even if we sample the Doppler data at the highest possible frequency in the ground system. In this case, the spin frequency should be changed to have an appropriate spin frequency in order to avoid folding of the harmonics in the lower band of the gravity field. We discuss the appropriate

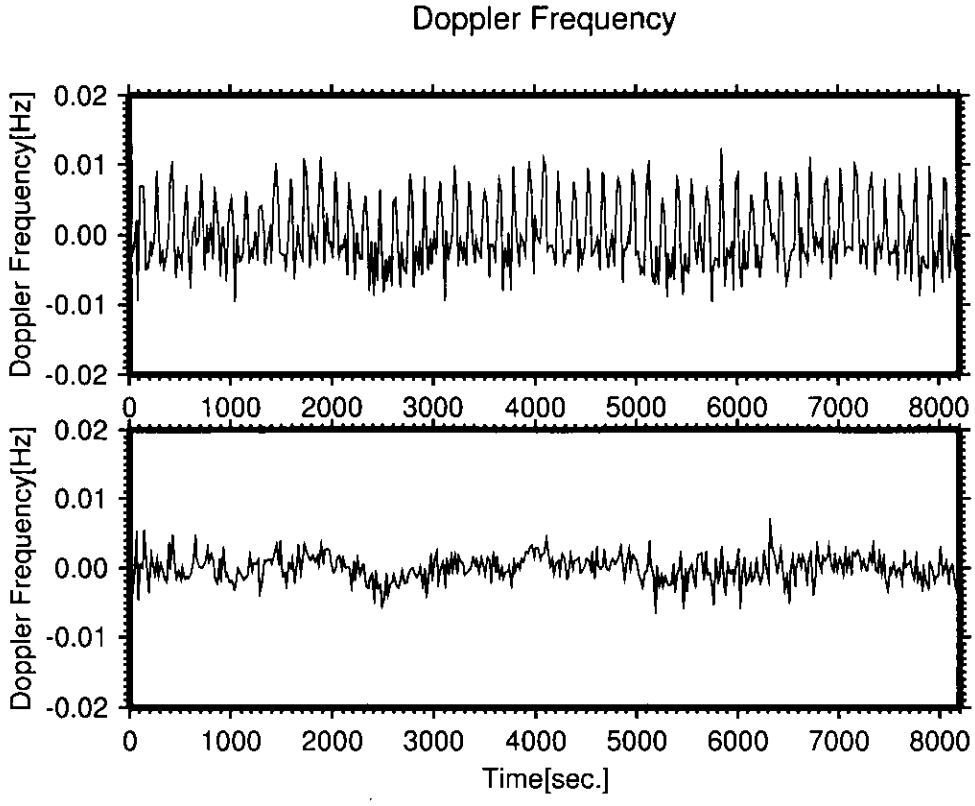

Figure 2.8: The Doppler frequency variations converted to 20 second sampled data. Upper figure: before filtering, lower figure: after filtering

spin frequency. As an example, the SELENE 4way Doppler tracked at Usuda Deep Space Center (UDSC), ISAS of Japan. The following parameters are assumed.

- The highest sampling frequency of UDSC is 1Hz
- Spin frequency is about 4 seconds (nominal value)
- The first, second, third and fourth order harmonics exist.
- The lower band of the gravity field is $0 \sim 1/20$Hz

Let's calculate frequencies of harmonics of the spin for various spin frequency by using Equation (2.1) and estimated the spin frequency which does not produce any harmonics in the lower frequency band of the gravity field. Finally, the condition of the spin period is yielded as shown in Figure 2.11.

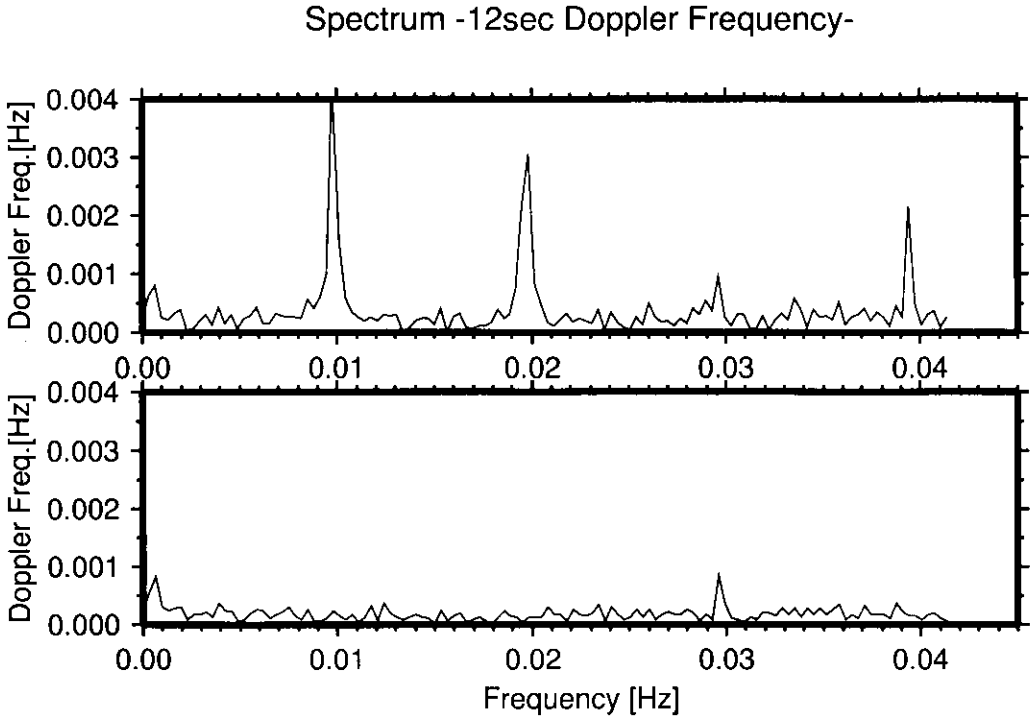

Figure 2.9: The Spectrum of Doppler frequency variations converted to 12 second sampled data. Upper figure: before filtering, lower figure: after filtering

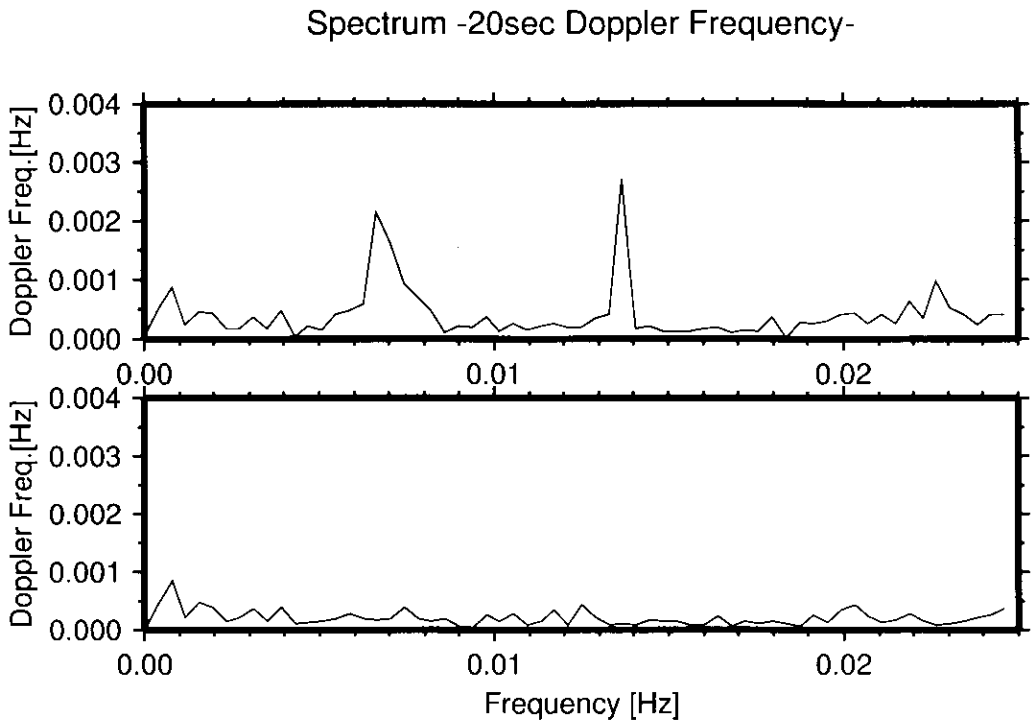

Figure 2.10: The Spectrum of Doppler frequency variations converted to 20 second sampled data. Upper figure: before filtering, lower figure: after filtering

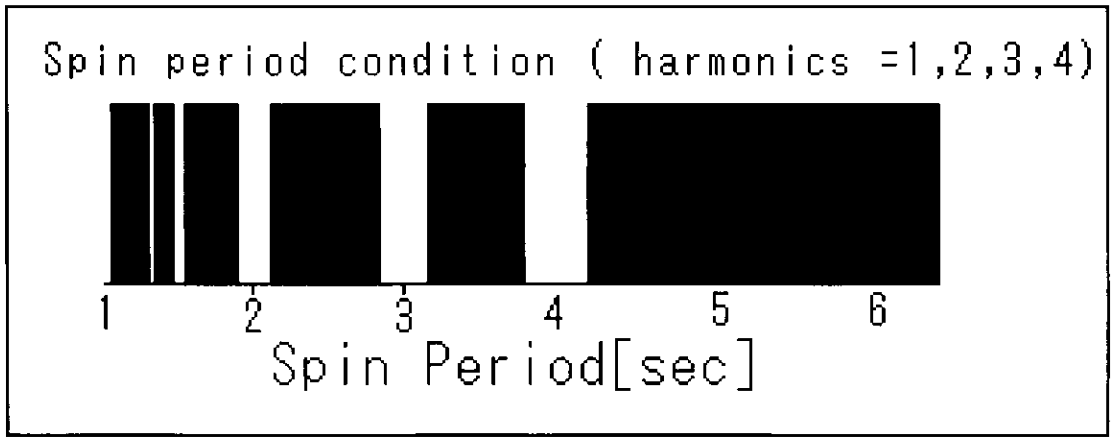

Figure 2.11: The spin period (white zone) which does not produce any frequency folded in the band of the gravity field variations, when the sampling frequency is 1 Hz and harmonics up to 4 th order exist.

Chapter 3

Multi-frequency VLBI method

3.1 Basic concepts of differential VLBI

VLBI [e.g., Hinteregger et al., 1972, Whitney 1974, Kawaguchi et al., 1983] is a powerful technique capable of measuring precise differences of the arrival times of the same radio wave from a radio source at distant place, and its application fields can be roughly divided into three areas. These areas are geodesy, astronomy and tracking an artificial planetary radio source which is treated in this thesis. The most important observable in VLBI is delay of arrival times of a wave front from a radio source at two ground stations. The wave front of the radio signal is approximated to be parallel planar in the case of radio sources beyond the solar system, i.e. the radio stars, pulsars, and the extra galactic radio sources. In the case of near radio sources, i.e. the celestial bodies in the solar system, the curved, or co-centered spherical surface of the wave front should be considered to calculate the delay. The definition of the delay in the case of curved wave front is clearly described in some papers [e.g., Sovers and Jacobs 1996].

The differential VLBI method is illustrated in Figure 3.1. A simple differential VLBI observation is basically composed of two sets of conventional VLBI (Single VLBI) systems together with two nearby radio sources to be observed at the same frequency. Considering the single VLBI model, a delay τ_{obs} obtained by the VLBI observation of a radio source $v1$ is given as

$$\tau_{obs} = \rho_s - \rho_r + n_{rs}, \tag{3.1}$$

where ρ_r and ρ_s are durations in propagation of the same radio wave from the transmitting time at the radio source $v1$ to the receiving time at ground VLBI stations r and s, respectively. n_{rs} is an error to be added in the observation. n_{rs} contains effects of the atmosphere above the VLBI stations and of the instruments at the VLBI stations [e.g., Shiomi et al., 1984, Asaki et al., 1996].

The delay τ'_{obs} obtained by the VLBI observation of a radio source v' at almost the same time of the former observation is also given as

$$\tau'_{obs} = \rho'_s - \rho'_r + n'_{rs}, \tag{3.2}$$

where ρ'_r and ρ'_s are durations in propagation of the same radio wave from the transmitting time at the radio source v' to the receiving time at ground VLBI stations r and s, respectively. n'_{rs} is a noise to be added in the observation. By differencing the two delays τ_{obs} and τ'_{obs}, an observable of differential VLBI is obtained as,

$$\tau_{obs} - \tau'_{obs} = \rho_s - \rho_r - \rho'_s + \rho'_r + n_{rs} - n'_{rs}. \tag{3.3}$$

If the angular distance between two radio sources is close enough and the two observations are carried out simultaneously for the two radio sources, the errors which are almost equal to each other in Equation (3.3) can be cancelled out perfectly. In particular, it is advantageous for cancellation of the tropospheric fluctuation because there is no effective method to remove the effect of the fluctuation so far [Asaki et al., 1996].

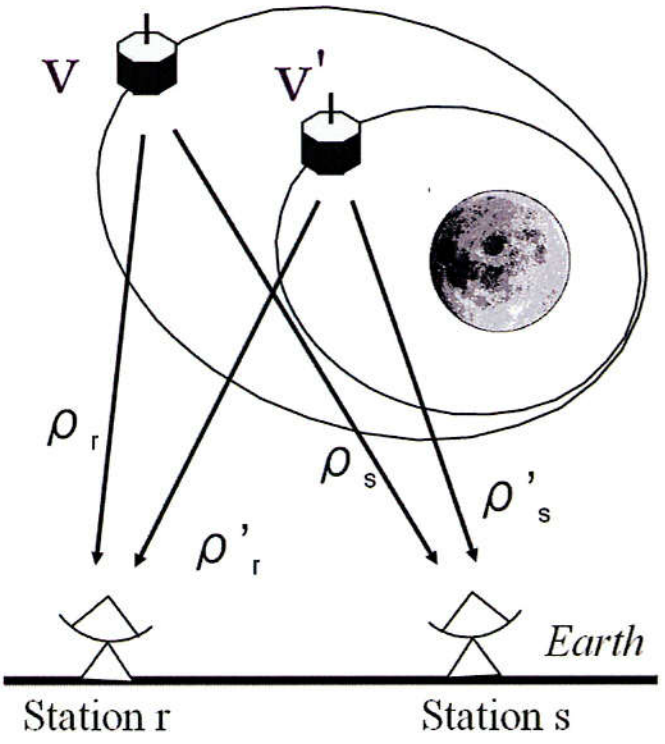

Figure 3.1: Basic concept of differential VLBI

3.2 Outline of Multi-frequency VLBI method

Although the group delay observable is commonly used in VLBI geodesy and astrometry, however, in the high precision differential VLBI observation, the phase delay observable is used for the natural radio source with a narrow signal bandwidth being detected or for the artificial radio source with carrier point bandwidth signal being observed. For this reason, the differential VLBI is also called 'phase referencing VLBI'. In the former section, the delay in the differential VLBI $\tau_{obs} - \tau'_{obs}$ is simply described. In an actual case for the phase delay observable, the differential phase $2\pi f(\tau_{obs} - \tau'_{obs})$ is obtained by cross correlation instead of the differential delay, where f is the center or point frequency of the radio signal. For a spacecraft, usually a carrier wave is transmitted so as to save the transmitting power and to obtain the signal with high signal to noise ratio (SNR). Unfortunately, the integer cycle ambiguity is involved in the differential phase, so that the differential delay cannot be derived directly from the phase delay observable. In order to solve this problem in conventional VLBI methods, the phase shift with parallax angle has been used so far [Counselman et al., 1973]. This differential VLBI method can be restrictively applied to the radio sources where position is not changed, such as the transmitter on the Moon or QSO.

If plural carrier waves of different frequencies can be transmitted from a spacecraft, the group delay of these carrier waves gives a possibility to resolve the cycle ambiguity for the phase delays of each carrier wave. A typical example is the differential VLBI measurements of the Venus atmosphere dynamics by balloons in VEGA mission. It used two carrier waves 6.5 MHz apart were transmitted from the balloon transmitters hovering in the atmosphere of the Venus [Sagdeyev et al.,1992]. In this mission, many ground VLBI stations of baseline lengths covering from 100 km to 5000 km were involved to try to determine the group delay between two carrier waves without cycle ambiguity. In addition to the difficulty of this experiment, the ionospheric effect could not be corrected because the two carrier waves were at the same frequency band. After all the cycle ambiguity resolution to determine the differential phase delay is not realized in the mission.

A new VLBI method, "multi-frequency VLBI" is proposed to resolve the cycle ambiguity. The radio transmitting system of the spacecraft transmits three carrier waves at S-band and one wave at X-band. The essential point to use plural carrier waves is that the combination of the carrier waves yields the group delays which help to resolve the cycle ambiguity of the phase delays of the carrier waves. The frequencies of these signals are chosen to resolve the cycle ambiguities of phase delays from the group delays.

3.3 Theory of the multi-frequency VLBI

3.3.1 Model of recorded signals

We show a cross correlation between two signals recorded at ground stations, r (reference station) and s (slave station) from one radio source v of two. The recorded signals $x_r^v(t_e)$ and $x_s^v(t_e)$ at time t_e at the reference station and the slave station are expressed as follows,

$$x_r^v(t_e) = e^{i\phi_r^v(t_e)} \tag{3.4}$$

$$x_s^v(t_e) = e^{i\phi_s^v(t_e)}, \tag{3.5}$$

where $\phi_r^v(t_e)$ and $\phi_s^v(t_e)$ are phases of the signals recorded at the two stations, respectively. In this section, data processing in respect of the radio source v is discussed, so that we omit the subscript v hereafter.

Let a phase of the transmitting signal k at the time t_e be $\phi_k(t_e)$. The subscript k indicates a signal of the four carrier waves of multi frequency VLBI. Let durations in propagations from transmitting time to receiving time be $\tau_r(t_e)$ and $\tau_s(t_e)$ at the two stations, respectively. The phases $\phi_r(t_e)$ and $\phi_s(t_e)$ of the signals received at the antennas of the stations at the time t_e after propagations are respectively given as,

$$\phi_r(t_e) = \phi_k(t_e - \tau_r(t_e)) \tag{3.6}$$

$$\phi_s(t_e) = \phi_k(t_e - \tau_s(t_e)). \tag{3.7}$$

The signals are recorded after two frequency-conversions. We consider one frequency-conversion for simple description. Since the frequency conversion is regarded as a subtraction of a phase of the local oscillator from a phase of a received signal, the phases $\phi_r'(t_e)$ and $\phi_s'(t_e)$ of the signals recorded at the stations after the frequency conversion are respectively given as,

$$\phi_r'(t_e) = \phi_k(t_e - \tau_r(t_e)) - \phi_{Lr}(t_e) \tag{3.8}$$

$$\phi_s'(t_e) = \phi_k(t_e - \tau_s(t_e)) - \phi_{Ls}(t_e), \tag{3.9}$$

where $\phi_{Lr}(t_e)$ and $\phi_{Ls}(t_e)$ are phases of the local signals at the two stations respectively.

3.3.2 Delay tracking, fringe stopping and cross correlation

The cross correlation is carried out between the signal recorded at the reference station and the signal recorded at the slave station. The latter signal should

be corrected so as to cancel the geometric delay by delay tracking by predicted one. The delay tracking is carried out by shifting the signal in time as a unit of the sampling interval. This process is called "bit shift". In addition the phase correction called fringe stopping is needed as well as the bit shift by using prediction of the geometric delay. The bit shift and the fringe stopping mean conversions of the signal recorded at the slave station to the signal recorded at the reference station by the prediction. If the prediction is real, the signal recorded at the slave station will be consistent with the signal recorded at the reference station.

Before describing the bit shift and the fringe stopping, we define the geometric delays by $\tau_r(t_e)$ and $\tau_s(t_e)$. Geometric delays are defined a the time difference between the time when a wave front transmitted from a radio source arrives at the reference station and the time when the same wave front arrives at the slave station [Sovers and Jacobs 1996]. The geometric delay $\tau_g(t_e)$ is defined as,

$$\tau_g(t_e) = \tau_s(t_e + \tau_g(t_e)) - \tau_r(t_e). \tag{3.10}$$

Now, we try to bit-shift the signal recorded at the slave station. Assuming the predicted geometric delay and the sampling period to be $\hat{\tau}_g(t_c)$ and T_{smp}, respectively, the amount of the shift τ_b is as follows,

$$\tau_b = T_{smp} NINT(\frac{\hat{\tau}_g(t_c)}{T_{smp}}), \tag{3.11}$$

where $NINT(x)$ means a operator to obtain the nearest integer of x. After the bit shift of τ_b, the phase of the signal recorded at the slave station is given as,

$$\phi'_s(t_e + \tau_b) = \phi_k(t_e + \tau_b - \tau_s(t_e + \tau_b)) - \phi_{Ls}(t_e + \tau_b). \tag{3.12}$$

Next, the fringe stopping is carried out by phase correction of the signal recorded at the slave station in respect of the phase rotation caused by $\tau_g(t_e)$. Let's the phase of the signal for the correction be $\phi_F(t_e)$. We obtain the phase $\phi''_s(t_e + \tau_b)$ of the signal corrected of the bit shift and the fringe stopping as,

$$\phi''_s(t_e + \tau_b) = \phi_k(t_e + \tau_b - \tau_s(t_e + \tau_b)) - \phi_{Ls}(t_e + \tau_b) - \phi_F(t_e). \tag{3.13}$$

Assuming that the central epoch of the time series data to be processed is t_c, the recording time t_e is written as,

$$t_e = t_c + t, \tag{3.14}$$

where t is shorter than several seconds in general. Substituting Equation (3.14) into Equation (3.6) and Equation (3.13), the phases are rewritten as,

$$\phi'_r(t_c + t) = \phi_k(t_c + t - \tau_r(t_c + t)) - \phi_{Lr}(t_c + t) \tag{3.15}$$

$$\phi''_s(t_c + t) = \phi_k(t_c + t + \tau_b - \tau_s(t_c + t + \tau_b)) - \phi_{Ls}(t_c + t + \tau_b) - \phi_F(t_c + t). \tag{3.16}$$

We expand $\phi_k(t_e)$, $\phi_{Lr}(t_e)$, $\phi_{Ls}(t_e)$, $\tau_r(t_e)$, $\tau_r(t_e+\tau_g(t_e))$, $\tau_g(t_e)$ around the epoch t_c for duration of t, as follows,

$$\begin{aligned}
\phi_k(t_c+t) &= 2\pi f_k t + \phi_k^{(0)} && (3.17)\\
\phi_{Lr}(t_c+t) &= 2\pi f_L t + \phi_{Lr}^{(0)} && (3.18)\\
\phi_{Ls}(t_c+t) &= 2\pi f_L t + \phi_{Ls}^{(0)} && (3.19)\\
\tau_r(t_c+t) &= \dot{\tau}_r t + \tau_r^{(0)} && (3.20)\\
\tau_s(t_c+t+\tau_g(t_c+t)) &= \dot{\tau}_s t + \tau_s^{(0)} && (3.21)\\
\tau_g(t_c+t) &= \dot{\tau}_g t + \tau_g^{(0)}, && (3.22)
\end{aligned}$$

where f_k is the frequency of the transmitted signal, $\phi_k^{(0)}$ is the initial phase of the transmitted signal, f_L is the frequency of the local oscillator signal, $\phi_{Lr}^{(0)}$ and $\phi_{Ls}^{(0)}$ are the initial phase of the local oscillator signals at stations r and s, respectively, $\tau_r^{(0)}$ and $\tau_s^{(0)}$ are the initial durations in propagations from transmitting time to receiving time at station r and s, respectively, $\dot{\tau}_r$ and $\dot{\tau}_s$ are the time derivatives of them, respectively, $\tau_g^{(0)}$ is the initial the geometric delay and, $\dot{\tau}_g$ is its time derivative. Note that the expansion of Equation (3.21) is not expansion around the epoch t_c, but around the epoch $t_c+\tau_g(t_e)$. Using the expansion in Equation (3.21), we obtain the expansion of $\tau_s(t_c+t+\tau_b)$ in Equation (3.16) as,

$$\begin{aligned}
\tau_s(t_c+t+\tau_b) &= \tau_s^{(0)} - \dot{\tau}_s[\tau_g(t_c+t)-\tau_b] && (3.23)\\
&= \tau_s^{(0)} - \dot{\tau}_s[\dot{\tau}_g t + \tau_g^{(0)} - \tau_b]. && (3.24)
\end{aligned}$$

The phase of the fringe stopping is expanded as

$$\phi_F(t_c+t) = 2\pi f_F[\hat{\dot{\tau}}_g t + \hat{\tau}_g{}^{(0)}], \quad (3.25)$$

where f_F is the frequency of the fringe stopping, and the prediction of the geometric delay $\hat{\tau}_g(t_e)$ is expanded as

$$\hat{\tau}_g(t_c+t) = \hat{\dot{\tau}}_g t + \hat{\tau}_g{}^{(0)}. \quad (3.26)$$

The phases in Equations (3.15) and (3.16) are expanded as,

$$\begin{aligned}
\phi_r'(t_c+t) &= [2\pi f_k[1-\dot{\tau}_r] - 2\pi f_L]t - 2\pi f_k \tau_r^{(0)} + \phi_k^{(0)} + \phi_{Lr}^{(0)} && (3.27)\\
\phi_s''(t_c+t+\tau_b) &= \left[2\pi f_k[1-\dot{\tau}_s+\dot{\tau}_s\dot{\tau}_g] - 2\pi f_L + 2\pi f_F\hat{\dot{\tau}}_g\right]t\\
&\quad +2\pi f_k[\tau_b - \tau_s^{(0)} + \dot{\tau}_s[\tau_g^{(0)} - \tau_b]]\\
&\quad +\phi_k^{(0)} - 2\pi f_L\tau_b + \phi_{Ls}^{(0)} + 2\pi f_F\hat{\tau}_g{}^{(0)}. && (3.28)
\end{aligned}$$

In order to simplify these phases, we define initial phases $\phi_r^{(0)}$ and $\phi_s^{(0)}$ and frequencies f_r and f_s as,

$$
\begin{aligned}
f_r &= f_k[1-\dot{\tau}_r] - f_L && (3.29)\\
f_s &= f_k[1-\dot{\tau}_s+\dot{\tau}_s\dot{\tau}_g] - f_L + f_F\dot{\hat{\tau}}_g && (3.30)\\
\phi_r^{(0)} &= -2\pi f_k\tau_r^{(0)} + \phi_k^{(0)} + \phi_{Lr}^{(0)} && (3.31)\\
\phi_s^{(0)} &= 2\pi f_k[\tau_b - \tau_s^{(0)} + \dot{\tau}_s[\tau_g^{(0)} - \tau_b]] + \phi_k^{(0)} - 2\pi f_L\tau_b + \phi_{Ls}^{(0)} \\
&\quad +2\pi f_F\hat{\tau}_g{}^{(0)}. && (3.32)
\end{aligned}
$$

The phases in Equations (3.27) and (3.28) are given as,

$$
\begin{aligned}
\phi_r(t_c+t) &= \phi_r^{(0)} + 2\pi f_r t && (3.33)\\
\phi_s''(t_c+t+\tau_b) &= \phi_s^{(0)} + 2\pi f_s t. && (3.34)
\end{aligned}
$$

Finally, the signals $x_r'(t_c+t)$ and $x_s''(t_c+t+\tau_b)$ which should be cross-correlated in the next section are expressed as follows,

$$
\begin{aligned}
x_r'(t_c+t) &= e^{i\phi_r'(t_c+t)} && (3.35)\\
x_s''(t_c+t+\tau_b) &= e^{i\phi_s''(t_c+t+\tau_b)}. && (3.36)
\end{aligned}
$$

3.3.3 Cross Spectrum

There are two types of correlators, XF type and FX type. Here we show the processing of the FX type correlator. It Fourier-transforms the signals at first and then does multiplication of them in a frequency domain and evaluates phase delay.

Firstly, we Fourier-transform the signal recorded at the reference station $x_r(t_c+t)$ to the spectral function $X_r(f)$ around the epoch t_c,

$$
\begin{aligned}
X_r(f) &= \frac{1}{2T}\int_{-T}^{T} x_r'(t_c+t)e^{-i2\pi ft}dt && (3.37)\\
&= sinc(2\pi(f_r-f)T)e^{i\phi_r^{(0)}}, && (3.38)
\end{aligned}
$$

where $sinc(x) = sin(x)/x$ and $2T$ is the integration time in the Fourier transformation. We also obtain the spectrum $X_s(f)$ of the signal recorded at the slave station,

$$
\begin{aligned}
X_s(f) &= \frac{1}{2T}\int_{-T}^{T} x_s''(t_c+t)e^{-i2\pi ft}dt && (3.39)\\
&= sinc(2\pi(f_s-f)T)e^{i\phi_s^{(0)}}. && (3.40)
\end{aligned}
$$

Correction of fractional bit

Before processing of the cross spectrum, fractional bit correction of the phase of the signal recorded at the slave station is carried out. This correction is due to the fact that delay is tracked by the bit shift in unit of bit. The amount of the correction depends on the frequency of the fringe stopping. We carry out the fringe stopping at the frequency of the local oscillator, that is,

$$f_F = f_L. \tag{3.41}$$

The fractional bit correction is carried out by multiplying the spectral function $X_s(f)$ of the slave station and the spectral function $X_{fra}(f)$ for the correction as follows [Takahashi et al., 2001],

$$X_{fra}(f) = e^{-i2\pi f[\tau_b - \hat{\tau}_g^{(0)}]}. \tag{3.42}$$

The spectral function $X_s(f)'$ corrected of the fractional bit is given as,

$$X_s'(f) = sinc(2\pi(f_s - f)T)e^{i\phi_s^{(0)}} \times e^{-i2\pi f[\tau_b - \hat{\tau}_g^{(0)}]}. \tag{3.43}$$

Cross Spectrum

A cross spectral function $C_{rs}(f)$ is obtained by multiplying $X_s'(f)$ which has been corrected of fractional bit and the complex conjugate of $X_r(f)$ as follows,

$$\begin{aligned} C_{rs}(f) &= X_s'(f) \times X_r^*(f)e^{-i2\pi f[\tau_b - \hat{\tau}_g^{(0)}]} && (3.44)\\ &= sinc(2\pi(f_s - f)T)sinc(2\pi(f_r - f)T)e^{i(\phi_s^{(0)} - \phi_r^{(0)} - 2\pi f[\tau_b - \hat{\tau}_g^{(0)}])} && (3.45)\\ &= A(f, f_s, f_r)e^{i\Delta\phi_{rs}^{(0)}(f)}, && (3.46) \end{aligned}$$

where x^* means the complex conjugate of x. We introduce the amplitude $A(f, f_s, f_r)$ and the phase $\Delta\phi_{rs}^{(0)}(f)$ to simplify the equation as follows,

$$\begin{aligned} A(f, f_s, f_r) &= sinc(2\pi(f_s - f)T)sinc(2\pi(f_r - f)T) && (3.47)\\ \Delta\phi_{rs}^{(0)}(f) &= \phi_s^{(0)} - \phi_r^{(0)} - 2\pi f[\tau_b - \hat{\tau}_g^{(0)}] && (3.48)\\ &= -2\pi f_k\tau_g^{(0)} + 2\pi[f_k - f_L]\tau_b + 2\pi f_F\hat{\tau}_g^{(0)} + 2\pi f_k\dot{\tau}_s[\tau_g^{(0)} - \tau_b] \\ &\quad + \Delta\psi_{rs} - 2\pi f[\tau_b - \hat{\tau}_g^{(0)}], && (3.49) \end{aligned}$$

where $\tau_g^{(0)}$=$\tau_s^{(0)} - \tau_r^{(0)}$ and $\Delta\psi_{rs} = \psi_s - \psi_r$.

Residual fringe phase

We extract "residual fringe phase" in the cross spectral function. Since f_r is almost equal to f_s by the fringe stopping, the spectral function has the largest

amplitude at f_s. The residual fringe phase is regarded as the phase at f_s of the cross spectral function in Equation (3.49),

$$\Delta\phi_{rs}^{(0)}(f_s) = -2\pi f_k[1-\dot{\tau}_s][\tau_g^{(0)}-\hat{\tau}_g^{(0)}] + \Delta\psi_{rs} - 2\pi f_k\dot{\tau}_s\dot{\tau}_g[\tau_b-\tau_g^{(0)}]. \quad (3.50)$$

The third term comes from the fact that delay is tracked by the bit shift in bit units. We try to do the order estimation of the term in the case of multi-frequency VLBI in SELENE project. The parameters in the term are as follows,

$$f_k \sim 8\times 10^9[Hz] \quad (3.51)$$
$$\dot{\tau}_s \sim 6\times 10^{-6}[sec/sec] \quad (3.52)$$
$$\tau_b-\tau_g^{(0)} \sim 3\times 10^{-6}[sec] \quad (3.53)$$
$$\dot{\tau}_g \sim 3\times 10^{-6}[sec/sec]. \quad (3.54)$$

Applying these vales to the third term, we obtain,

$$2\pi f_k\dot{\tau}_s\dot{\tau}_g[\tau_b-\tau_g^{(0)}] \sim 10^{-5}[deg.]. \quad (3.55)$$

From Equation (3.55), this term is negligible. Finally we obtain the residual fringe phase as follows,

$$\Delta\phi_{rs}^{(0)}(f_s) = -2\pi f_k[1-\dot{\tau}_s][\tau_g^{(0)}-\hat{\tau}_g^{(0)}] + \Delta\psi_{rs}. \quad (3.56)$$

This residual fringe phase is the important observable in multi-frequency VLBI because it includes $\tau_g^{(0)}-\hat{\tau}_g^{(0)}$ the residual delay which we should be obtained.

Effects on the residual fringe phase by frequency variations

The residual fringe phase depends on the frequency of the transmitted radio signal, and the variation of it affects the residual fringe phase. In order to know the phase error by the frequency variation, we introduce f_k' instead of f_k as follows,

$$f_k' = f_k + \delta f_k. \quad (3.57)$$

Substituting f_k' into Equation (3.56), we obtain,

$$\Delta\phi_{rs}^{(0)}(f_s) = -2\pi f_k[1-\dot{\tau}_s][\tau_g^{(0)}-\hat{\tau}_g^{(0)}] - 2\pi\delta f_k[1-\dot{\tau}_s][\tau_g^{(0)}-\hat{\tau}_g^{(0)}] + \Delta\psi_{rs}. \quad (3.58)$$

The second term corresponds to the phase error by the frequency variation. The term introduces a condition of the frequency variation to achieve the accuracy of the phase 4 [deg.]. If $\tau_s \sim 10^{-6}$, $\tau_g^{(0)}-\hat{\tau}_g^{(0)}$ is a accuracy of the geometric delay

of prediction and expected to be less than 10^{-7} which will be described in later section, we obtain,

$$|-2\pi\delta f_k[1-\dot{\tau}_s][\tau_g^{(0)}-\hat{\tau}_g^{(0)}]| < 2\pi\frac{4}{360} \quad (3.59)$$

$$\delta f_k < 100[kHz]. \quad (3.60)$$

3.4 The cycle ambiguity resolution

3.4.1 Doubly differenced residual fringe phase

The Differential VLBI observes two nearby radio sources. The effects of delays which are introduced by the ionosphere, the troposphere, frequency standards and instruments of the ground station are almost the same for this pair of radio sources, they are reduced by the differencing the two fringe phases. The differenced phases mentioned above are called the doubly differenced fringe phase. The observations of the two nearby radio sources should be carried out at the same time. The angler distance, however, is bigger than the beam-width of the antenna in general. The antenna-switching method, in which two radio sources are observed alternatively in time, is usually used. The effect on the doubly differenced fringe phase due to the differencing of the fringe phases of antenna-switching method is discussed here.

An observation sequence of the antenna-switching method is like $v1$ at $t_c - T_{sw}$, $v2$ at t_c and $v1$ at $t_c + T_{sw}$ where $v1$ and $v2$ are radio sources, T_{sw} is a switching interval and the times, $t_c - T_{sw}$, t_c and $t_c + T_{sw}$ mean the central epoch of each observation as shown in Figure 3.2. We obtain the three residual fringe phases $\Delta\phi^{v1}(t_c - T_{sw})$, $\Delta\phi^{v2}(t_c)$, $\Delta\phi^{v1}(t_c + T_{sw})$ in each observation. The doubly differenced residual fringe phase at the time t_c is obtained by differencing the phase of $v2$ and the phase interpolated between two $v1$ observations. The interpolation is carried out by the simple averaging in general, and the doubly differenced residual fringe phase $\Delta\Delta\phi^{v12}(t_c)$ is given as

$$\Delta\Delta\phi^{v12}(t_c) = \Delta\phi^{v2}(t_c) - \frac{1}{2}\left[\Delta\phi^{v1}(t_c - T_{sw}) + \Delta\phi^{v1}(t_c + T_{sw})\right]. \quad (3.61)$$

This processing is illustrated in Figure 3.2. Hereafter, the doubly differenced residual fringe phase is discussed in more detail. In Equation (3.56), the residual fringe phase of a radio source v ($=v1$ or $v2$) at the time t_c is given as follows,

$$\Delta\phi^{v(0)}(t_c) = -2\pi f_k^v[1 - \dot{\tau}_s^v][\tau_g^{v(0)} - \hat{\tau}_g^{v(0)}] + \Delta\psi_{rs,k}, \quad (3.62)$$

where f_k^v is the frequency of the radio signal v around the time t_c, $\dot{\tau}_s^v$ is the propagation delay rate at the slave station, $\tau_g^{v(0)} - \hat{\tau}_g^{v(0)}$ is the residual geometric delay from the predicted one, and $\Delta\psi_{rs}^v$ is the initial phase difference of the local oscillators. The residual fringe phase $\Delta\phi^{v(0)}(t_c)$ of the radio signals at the time t_c can be simplified as

$$\Delta\phi^{v(0)}(t_c) = -2\pi f_{k,s}^v(t_c)\delta\tau_g^v(t_c) + \Delta\psi_{rs,k}, \quad (3.63)$$

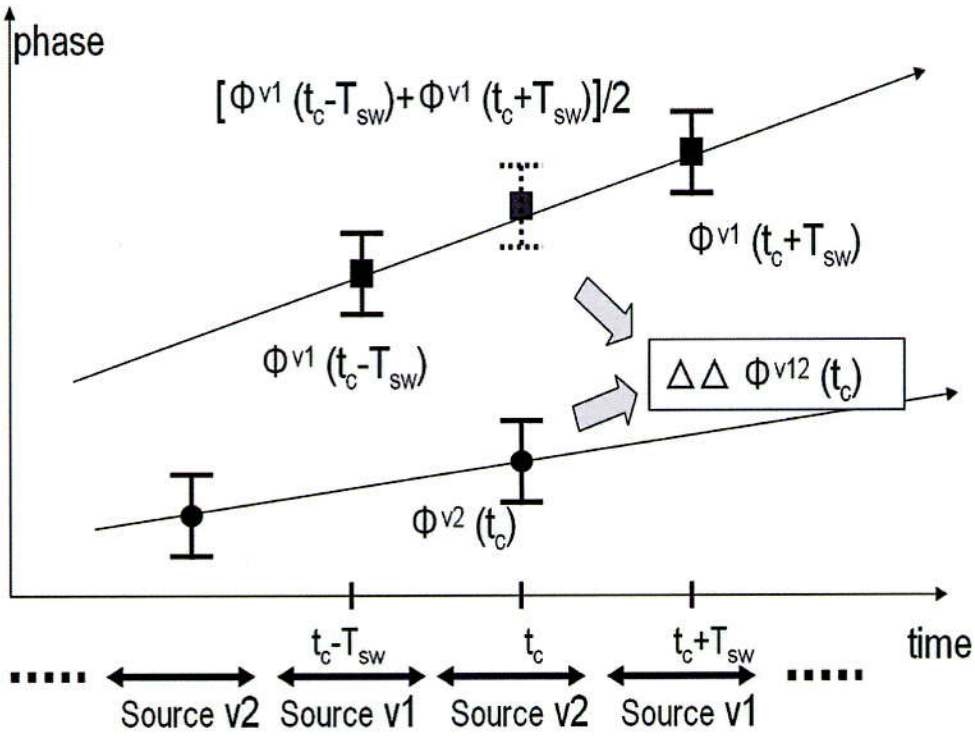

Figure 3.2: Residual fringe phases observed by an antenna-switching VLBI

where $f^v_{k,s}$ is $f^v_k[1-\dot{\tau}^v_s]$ at the time t_c. In the same way, the three residual fringe phases at $t_c - T_{sw}$, t_c and $t_c + T_{sw}$ are obtained as follows,

$$\begin{aligned}
\Delta\phi^{v1}_{rs,k}(t_c - T_{sw}) &= -2\pi f^{v1}_{k,s}(t_c - T_{sw})\delta\tau^{v1}_g(t_c - T_{sw}) + \Delta\psi_{rs,k} && (3.64)\\
\Delta\phi^{v1}_{rs,k}(t_c) &= -2\pi f^{v2}_{k,s}(t_c)\delta\tau^{v2}_g(t_c) + \Delta\psi_{rs,k} && (3.65)\\
\Delta\phi^{v1}_{rs,k}(t_c + T_{sw}) &= -2\pi f^{v1}_{k,s}(t_c + T_{sw})\delta\tau^{v1}_g(t_c + T_{sw}) + \Delta\psi_{rs,k}. && (3.66)
\end{aligned}$$

The doubly differenced residual fringe phase $\Delta\Delta\phi^{v12}(t_c)$ is obtained as follows,

$$\begin{aligned}
\Delta\Delta\phi^{v12}(t_c) &= -2\pi f^{v2}_{k,s}(t_c)\left[\delta\tau^{v2}_g(t_c) - \frac{1}{2}[\tau^{v1}_g(t_c - T_{sw}) + \delta\tau^{v1}_g(t_c + T_{sw})]\right]\\
&\quad -\pi[f^{v1}_{k,s}(t_c) - f^{v2}_{k,s}(t_c)]\left[\delta\tau^{v1}_g(t_c - T_{sw}) + \delta\tau^{v1}_g(t_c + T_{sw})\right]\\
&\quad -\pi[f^{v1}_{k,s}(t_c - T_{sw}) - f^{v1}_{k,s}(t_c)]\delta\tau^{v1}_g(t_c - T_{sw})\\
&\quad -\pi[f^{v1}_{k,s}(t_c + T_{sw}) - f^{v1}_{k,s}(t_c)]\delta\tau^{v1}_g(t_c + T_{sw}). && (3.67)
\end{aligned}$$

The first term of the right side of Equation (3.67) is the doubly differenced residual fringe phase which should be obtained. The second term is the effect of the frequency difference between the two radio signals at the time t_c. The third and fourth terms are the effects of the frequency variations of the radio signals in the time interval T_{sw}. In order to simplify the description of the equation, two variables is introduced as follows,

$$\begin{aligned}
\delta\delta\tau^{v12}_g(t_c) &= \delta\tau^{v2}_g(t_c) - \frac{1}{2}[\tau^{v1}_g(t_c - T_{sw}) + \delta\tau^{v1}_g(t_c + T_{sw})] && (3.68)\\
\sigma_{\Delta\Delta\phi_{f,\delta\tau_g}} &= -\pi[f^{v1}_{k,s}(t_c) - f^{v2}_{k,s}(t_c)]\left[\delta\tau^{v1}_g(t_c - T_{sw}) + \delta\tau^{v1}_g(t_c + T_{sw})\right]\\
&\quad -\pi[f^{v1}_{k,s}(t_c - T_{sw}) - f^{v1}_{k,s}(t_c)]\delta\tau^{v1}_g(t_c - T_{sw})\\
&\quad -\pi[f^{v1}_{k,s}(t_c + T_{sw}) - f^{v1}_{k,s}(t_c)]\delta\tau^{v1}_g(t_c + T_{sw}), && (3.69)
\end{aligned}$$

where $\delta\delta\tau^{v12}_g$ means the observable of the differential VLBI to be obtained; $\sigma_{\Delta\Delta\phi_{f,\delta\tau_g}}$ means the effect of the frequency difference between the two radio signals and the effects of the frequency variations of the radio signals. The doubly differenced residual fringe phase is re-written simply as,

$$\Delta\Delta\phi^{v12}(t_c) = -2\pi f^{v2}_{k,s}(t_c)\delta\delta\tau^{v12}_g(t_c) + \sigma_{\Delta\Delta\phi_{f,\delta\tau_g}}. \quad (3.70)$$

The term $\sigma_{\Delta\Delta\phi_{f,\delta\tau_g}}$ must be less than the expected accuracy of the doubly differenced residual fringe phase. This error will be discussed quantitatively in later Section 3.4.12 because this quantity depends on the accuracy of the prediction of the geometric delay which is discussed in Section 3.4.12. Assuming $\sigma_{\Delta\Delta\phi_{f,\delta\tau_g}} \ll 1$, the doubly differenced fringe phase at the time t_c is obtained as follow,

$$\Delta\Delta\phi^{v12}(t_c) \sim -2\pi f^{v2}_{k,s}(t_c)\delta\delta\tau^{v12}_g(t_c). \quad (3.71)$$

3.4.2 Various effects on the doubly differenced residual fringe phase

The doubly differenced residual fringe phase has been derived under a simplified condition that only geometric delay has been considered. Let's consider all the delays introduced by the ionosphere, the troposphere and instrument in the ground stations. The following term of the delay is introduced instead of $\delta\delta\tau_g^{v12}(t_c)$ in Equation (3.71) as follows,

$$\delta\delta\tau_g^{v12}(t_c) + \delta\delta\tau_{ion}^{v12}(t_c) + \delta\delta\tau_{tro}^{v12}(t_c) + \delta\delta\tau_{gnd}^{v12}(t_c). \tag{3.72}$$

Note that $\delta\delta\tau_{ion}^{v12}(t_c)$, $\delta\delta\tau_{tro}^{v12}(t_c)$ and $\delta\delta\tau_{gnd}^{v12}(t_c)$ are the doubly differenced delays between the radio source $v1$ and $v2$.

In general, a delay τ_{ion} in the ionosphere for a radio signal at a frequency f is given as

$$\tau_{ion} = \frac{kD}{f^2}, \tag{3.73}$$

where k is the constant ($k = 1.34 \times 10^{-7}[m^2/el\ s]$) and D is the total electron content (TEC) $[el/m^2]$ in the ionosphere along the signal propagation path. In this manner, $\delta\delta\tau_{ion}^{v12}(t_c)$ at the frequency $f_{k,s}^{v2}$ is given as

$$\delta\delta\tau_{ion}^{v12}(t_c) = \frac{k\delta\delta D^{v12}}{f_{k,s}^{v2}(t_c)^2}, \tag{3.74}$$

where $\delta\delta D^{v12}$ is the doubly differenced TEC between the radio sources $v1$ and $v2$. $\delta\delta\tau_g^{v12}(t_c)$, $\delta\delta\tau_{tro}^{v12}(t_c)$ and $\delta\delta\tau_{gnd}^{v12}(t_c)$ affect the phase linearly to its frequencies. They can be combined to $\delta\delta\tau_{all}^{v12}(t_c)$ for simple description as,

$$\delta\delta\tau_{all}^{v12}(t_c) = \delta\delta\tau_g^{v12}(t_c) + \delta\delta\tau_{tro}^{v12}(t_c) + \delta\delta\tau_{gnd}^{v12}(t_c). \tag{3.75}$$

Phase noises are also included in the doubly differenced residual fringe phase in Equation (3.71). The total phase noise to be observed in the doubly differenced residual fringe phase can be expressed as follows,

$$[[\sigma_{\phi_k^{v12}}]], \tag{3.76}$$

where $[[x]]$ indicates the error which obeys the error theorem. For example, the following relation stands up.

$$[[a]] \pm [[b]] = \left[\left[\sqrt{a^2 + b^2}\right]\right]. \tag{3.77}$$

The doubly differenced residual fringe phase actually includes the cycle ambiguity of 2π. The doubly differenced residual fringe phase can be separated to the

observed raw phase $\Delta\Delta\phi^{v12}_{obs}$ and the cycle ambiguities $2\pi N^{v12}_k$ (where N^{v12}_k is an integer as $..., -2, -1, 0, 1, 2, ...$), that is,

$$\Delta\Delta\phi^{v12}(t_c) = \Delta\Delta\phi^{v12}_{obs} + 2\pi N^{v12}_k. \tag{3.78}$$

Considering all the effects mentioned above, the doubly differenced residual fringe phase can be modeled as follows,

$$\Delta\Delta\phi^{v12}_{obs} + 2\pi N^{v12}_k = -2\pi f^{v2}_{k,s}(t_c)\delta\delta\tau^{v12}_{all}(t_c) + \frac{2\pi k\delta\delta D^{v12}}{f^{v2}_{k,s}(t_c)} + [[\sigma_{\phi^{v12}_k}]]. \tag{3.79}$$

3.4.3 Four observables in the multi-frequency VLBI

In multi-frequency VLBI, four carrier waves are observed with three waves in S-band ($s1$, $s2$, $s3$) and one in X-band (x). From them, four of the doubly differenced residual fringe phases can be obtained. We consider Equation (3.79) at frequencies of $s1$, $s2$, $s3$ and x. Assuming all the phase noise $[[\sigma_{\phi^{v12}_k}]]$ is equal to $[[\sigma_{\phi_{obs}}]]$. The four doubly differenced residual fringe phases are simply given as,

$$\phi_{obs,s1} = 2\pi f_{s1}\tau_{all,s} - 2\pi N_{s1} - 2\pi kD\frac{1}{f_{s1}} + [[\sigma_{\phi_{obs}}]] \tag{3.80}$$

$$\phi_{obs,s2} = 2\pi f_{s2}\tau_{all,s} - 2\pi N_{s2} - 2\pi kD\frac{1}{f_{s2}} + [[\sigma_{\phi_{obs}}]] \tag{3.81}$$

$$\phi_{obs,s3} = 2\pi f_{s3}\tau_{all,s} - 2\pi N_{s3} - 2\pi kD\frac{1}{f_{s3}} + [[\sigma_{\phi_{obs}}]] \tag{3.82}$$

$$\phi_{obs,x} = 2\pi f_x\tau_{all,x} - 2\pi N_x - 2\pi kD\frac{1}{f_x} + [[\sigma_{\phi_{obs}}]], \tag{3.83}$$

where the notation t_c is omitted. Note that $\tau_{all,s}$ is defferent from $\tau_{all,x}$ in Equations (3.80) $\sim$ (3.83), because the two antenna for S-band and X-band share neither the signal phase center nor the geometric center. So, the $\tau_{all,s}$ and $\tau_{all,x}$ are introduced separatedly for S-band and X-band signals.

In the following sections, the resolvent of the cycle ambiguities will be discussed quantitatively. In the discussions, the following values for frequencies are used.

$$f_{s1} = 2212MHz \tag{3.84}$$

$$f_{s2} = 2218MHz \tag{3.85}$$

$$f_{s3} = 2287MHz \tag{3.86}$$

$$f_x = 8456MHz. \tag{3.87}$$

These values are given in SELENE project [Hanada et al., 2001].

3.4.4 Basic concept of the resolvent of the cycle ambiguity

The four observation equations of the multi-frequency VLBI have been derived in Equations (3.80), (3.81), (3.82) and (3.83). The accuracy of the phase delay is proportional to the frequency of the carrier signal on an assumption that the phase error is independent of the frequency. It is the most advantageous to determine the phase delay of X-band signal from Equation (3.83). Other three equations are used for only the resolvent of the cycle ambiguities of the signals at both S and X-band. In order to obtain the phase delay of the carrier wave in X-band, four procedures are taken as follows,

1. Cycle ambiguity resolvent of the wide lane $[s1 - s2]$
2. Cycle ambiguity resolvent of the wide lane $[s1 - s3]$
3. Cycle ambiguity resolvent of the carrier wave $[s1]$
4. Cycle ambiguity resolvent of the carrier wave $[x]$

where the wide lane is one kind of linear combinations of two carrier waves [Hatch 1982]. The phase of the wide lane is formed by subtraction of the phase of one carrier wave from that of the other carrier wave. For example, a wide lane ϕ_{w12} between fringe phase ϕ_1 and fringe phase ϕ_2 is defines as $\phi_{w12}=\phi_1 - \phi_2$. Let's $\phi_1 = 2\pi f_1 \tau$ and $\phi_2 = 2\pi f_2 \tau$, the wide lane ϕ_{w12} is given as $\phi_{w12}=2\pi[f_1 - f_2]\tau$. The frequency of the wide lane corresponds to the frequency difference of the two carrier signals. The name, "wide lane" comes from the fact that the interval between the cycle ambiguities is wide. The wide lane yields the group delay. The basic concept and target of the four procedures is to resolve the cycle ambiguity in order of wider interval.

3.4.5 Cycle ambiguity resolvent of the wide lane $[s1 - s2]$

First of all, the cycle ambiguity of the wide lane of $s1$ and $s2$ carrier waves will be solved. The wide lane is formed by Equation (3.80) and Equation (3.81), then the phase $\phi_{obs,ws2s1}$ of the wide lane is given as,

$$\begin{aligned} \phi_{obs,ws2s1} &= 2\pi f_{ws2s1}\tau_{all,s} + 2\pi[N_{s2} - N_{s1}] - 2\pi kD(\frac{1}{f_{s2}} - \frac{1}{f_{s1}}) \\ &\quad +[[\sqrt{2}\sigma_{\phi_{obs}}]]. \end{aligned} \tag{3.88}$$

The term $N_{s2} - N_{s1}$ is given as follows,

$$N_{s2} - N_{s1} = \frac{\phi_{obs,ws2s1}}{2\pi} - f_{ws2s1}\tau_{all,s} + kD(\frac{1}{f_{s2}} - \frac{1}{f_{s1}}) + [[\frac{\sqrt{2}\sigma_{\phi_{obs}}}{2\pi}]], \tag{3.89}$$

where f_{ws2s1}=$f_{s2} - f_{s1}$= 6MHz.

In order to resolve the cycle ambiguity of $N_{s2} - N_{s1}$ in Equation (3.89),all term in the right side must be less than $\pm$ 1/2 cycle or π. The first term is the differential of the doubly differenced residual fringe phase in the wide lane. The second term is the difference between the observation delay and the predicted oneincludes $\tau_{all,s}$ which is ambiguous. The condition of $\tau_{all,s}$ depends on the accuracy of the prediction of the geometric delay as follows,

$$|f_{ws2s1}\tau_{all,s}| \ < \ \frac{1}{2}. \tag{3.90}$$

Substituting f_{ws2s1}=$f_{s2} - f_{s1}$= 6MHz, the following condition about $\tau_{all,s}$ is obtained,

$$\tau_{all,s} \ < \ 8.3 \times 10^{-8}[sec.]. \tag{3.91}$$

The result corresponds to 4.8 km of position accuracy around the Moon for 2000 km baseline length. This condition can be easily satisfied by using current positioning techniques such as range and range rate measurements.

The third term in right side of Equation (3.89) is the differenced phase fluctuated by the ionosphere. The condition is yielded as well as the second term,

$$\left|-kD(\frac{1}{f_{s2}} - \frac{1}{f_{s1}})\right| \ < \ \frac{1}{2}. \tag{3.92}$$

Substituting the values of f_{s2} and f_{s1}, the condition about D is obtained as,

$$D \ < \ 3.1 \times 10^{18}[el/m^2]. \tag{3.93}$$

Because the order of magnitude of this value is equal to that of the maximum value (10^{18}) of the Earth ionosphere, the doubly differenced TEC always satisfies this condition easily.

The fourth term in the right side of Equation (3.89) is caused by the phase noise of the received signal. The condition is also yielded as follows,

$$[[\frac{\sqrt{2}\sigma_{\phi_{obs}}}{2\pi}]] \ < \ \frac{1}{2} \tag{3.94}$$

$$\sigma_{\phi_{obs}} \ < \ 130[deg.]. \tag{3.95}$$

The validity of these conditions will be discussed in the latter section.

In the case of the three conditions in Equations (3.91), (3.93) and (3.95) are satisfied, the cycle ambiguity $N_{s2} - N_{s1}$ of s1-s2 wide lane can be resolved.

3.4.6 Cycle ambiguity resolvent of the wide lane $[s1 - s3]$

The cycle ambiguity of the wide lane of $s1$ and $s3$ carrier waves will be resolved. The wide lane is formed by Equations (3.80) and (3.82), and the phase $\phi_{obs,ws3s1}$ of the wide lane is given as follows,

$$\begin{aligned}\phi_{obs,ws3s1} &= 2\pi f_{ws3s1}\tau_{all,s} + 2\pi[N_{s3} - N_{s1}] - 2\pi kD(\frac{1}{f_{s3}} - \frac{1}{f_{s1}}) \\ &\quad +[[\sqrt{2}\sigma_{\phi_{obs}}]]. \end{aligned} \tag{3.96}$$

where f_{ws3s1}=$f_{s3} - f_{s1}$= 75MHz. In order to eliminate $\tau_{all,s}$ in Equation (3.96), the following equation is formed by Equations (3.96) and (3.88) as follows,

$$\begin{aligned}\frac{\phi_{obs,ws3s1}}{2\pi f_{ws3s1}} - \frac{\phi_{obs,ws2s1}}{2\pi f_{ws2s1}} &= \frac{[N_{s3} - N_{s1}]}{f_{ws3s1}} - \frac{[N_{s2} - N_{s1}]}{f_{ws2s1}} \\ &\quad -kD\left[[\frac{1}{f_{s3}} - \frac{1}{f_{s1}}]\frac{1}{f_{ws3s1}} - [\frac{1}{f_{s2}} - \frac{1}{f_{s1}}]\frac{1}{f_{ws2s1}}\right] \\ &\quad +[[\frac{\sqrt{2}\sigma_{\phi_{obs}}}{2\pi f_{ws3s1}}]] - [[\frac{\sqrt{2}\sigma_{\phi_{obs}}}{2\pi f_{ws2s1}}]] \end{aligned} \tag{3.97}$$

$$\begin{aligned}N_{s3} - N_{s1} &= \frac{\phi_{obs,ws3s1}}{2\pi} - \left[\frac{\phi_{obs,ws2s1}}{2\pi} - [N_{s2} - N_{s1}]\right]\frac{f_{ws3s1}}{f_{ws2s1}} \\ &\quad +kD\frac{[f_{s3} - f_{s2}][f_{s3} - f_{s1}]}{f_{s3}f_{s2}f_{s1}} \\ &\quad +[[\frac{\sqrt{2}\sigma_{\phi_{obs}}}{2\pi}]] - [[\frac{\sqrt{2}f_{ws3s1}\sigma_{\phi_{obs}}}{2\pi f_{ws2s1}}]]. \end{aligned} \tag{3.98}$$

The first and the second terms are obtained from observed data and the result of the former section.

The conditions for the third and fourth terms are given in the same way as Section 3.4.5 as follows,

$$D < 8.1 \times 10^{18}[el/m^2] \tag{3.99}$$

$$\sigma_{\phi_{obs}} < 10.1[deg.]. \tag{3.100}$$

The validity of these conditions will be discussed in the latter section.

In the case that the two conditions are satisfied, the cycle ambiguity $N_{s3} - N_{s1}$ of $s1 - s3$ wide lane can be resolved.

3.4.7 Cycle ambiguity resolvent of carrier wave $[s1]$

The cycle ambiguity of the carrier wave $s1$ is resolved. In order to eliminate the $\tau_{all,s}$ in Equation (3.80), the following equation is formed by Equations (3.80) and

(3.96) as follows,

$$\frac{\phi_{obs,s1}}{2\pi f_{s1}} - \frac{\phi_{obs,ws3s1}}{2\pi f_{ws3s1}} = \frac{N_{s1}}{f_{s1}} - \frac{[N_{s3} - N_{s1}]}{f_{ws3s1}} - kD\left[\frac{1}{f_{s1}^2} - [\frac{1}{f_{s3}} - \frac{1}{f_{s1}}]\frac{1}{f_{ws3s1}}\right] + [[\frac{\sigma_{\phi_{obs}}}{2\pi f_{s1}}]] - [[\frac{\sqrt{2}\sigma_{\phi_{obs}}}{2\pi f_{ws3s1}}]] \quad (3.101)$$

$$N_{s1} = \frac{\phi_{obs,s1}}{2\pi} - \left[\frac{\phi_{obs,ws3s1}}{2\pi} - [N_{s3} - N_{s1}]\right]\frac{f_{s1}}{f_{ws1s3}} + kD\frac{f_{s3} + f_{s1}}{f_{s3}f_{s1}} - [[\frac{\sigma_{\phi_{obs}}}{2\pi}]] + [[\frac{\sqrt{2}f_{s1}\sigma_{\phi_{obs}}}{2\pi f_{ws2s1}}]]. \quad (3.102)$$

The first and the second terms are obtained from observed data and the result of the former section.

The conditions for the third, fourth and fifth terms are given in the same way as Section 3.4.5 as follows,

$$D < 4.2 \times 10^{15}[el/m^2] \quad (3.103)$$

$$\sigma_{\phi_{obs}} < 4.3[deg]. \quad (3.104)$$

The validity of these conditions will be discussed in the later section.

In the case that the two conditions are satisfied, the cycle ambiguity N_{s1} of the carrier wave $s1$ can be resolved.

3.4.8 Cycle ambiguity resolvent of the carrier wave $[x]$

Finally the cycle ambiguity of the carrier wave x will be resolved. Before eliminating $\tau_{all,x}$ in Equations (3.80) and (3.83), we consider that the delay $\tau_{all,x}$ is not equal to $\tau_{all,s}$, because of the displacement between the antennas of S-band and X-band. The delay difference $\delta\tau_{all}$ is introduced as,

$$\delta\tau_{all} = \tau_{all,x} - \tau_{all,s}. \quad (3.105)$$

Equation (3.83) is re-written as follows,

$$\phi_{obs,x} = 2\pi f_x[\tau_{all,s} + \delta\tau_{all}] + 2\pi N_x - 2\pi kD\frac{1}{f_x} + [[\sigma_{\phi_{obs}}]]. \quad (3.106)$$

In order to eliminate the $\tau_{all,s}$ in Equation (3.106), the following equation is formed by Equations (3.80) and (3.106) as,

$$\frac{\phi_{obs,x}}{2\pi f_x} - \frac{\phi_{obs,s1}}{2\pi f_{s1}} = \delta\tau_{all} + \frac{N_x}{f_x} - \frac{N_{s1}}{f_{s1}} - kD[\frac{1}{f_x^2} - \frac{1}{f_{s1}^2}] + [[\frac{\sigma_{\phi_{obs}}}{2\pi f_x}]] - [[\frac{\sigma_{\phi_{obs}}}{2\pi f_{s1}}]] \quad (3.107)$$

$$N_x = \frac{\phi_{obs,x}}{2\pi} - [\frac{\phi_{obs,s1}}{2\pi} - N_{s1}]\frac{f_x}{f_{s1}} - kD\frac{f_x^2 - f_{s1}^2}{f_x f_{s1}^2}$$
$$-[[\frac{\sigma_{\phi_{obs}}}{2\pi}]] + [[\frac{f_x \sigma_{\phi_{obs}}}{2\pi f_{s1}}]] - f_x \delta\tau_{all}. \quad (3.108)$$

The first and the second terms are obtained from observed data and the result of the former section.

The conditions for the third, fourth and fifth terms are given in the same way as Section 3.4.5 as follows,

$$D < 2.3 \times 10^{15} \ [el/m^2] \quad (3.109)$$
$$\sigma_{\phi_{obs}} < 91[deg.]. \quad (3.110)$$

The validity of these conditions will be discussed in the later section.

The condition for the last term is given as

$$|f_x \delta\tau_{all}| < \frac{1}{2} \quad (3.111)$$
$$< 5.9 \times 10^{-11}[sec.]. \quad (3.112)$$

This value of the geometric delay difference corresponds to position displacement between S-band antenna and X-band antenna of 3.4 m at the moon in the case of 2000km baseline. The antennas of the relay satellite of SELENE are placed within 20 cm actually.

The ambiguity N_x in Equation (3.108) is resolved finally, when all the conditions is satisfied.

3.4.9 Condition about the phase noise of received signal

The four conditions have been obtained about the phase noise of the received signal in Equations (3.95), (3.100), (3.104) and (3.110). In order to resolve all ambiguity, the condition about the phase noise should be less than the minimum one of them as follows

$$\sigma_{\phi_{obs}} < 4.3[deg.]. \quad (3.113)$$

This condition should be considered in realization of the multi-frequency VLBI.

3.4.10 TEC error

TEC can be estimated by using the phases of s1 and x carrier wave. The geometric free combination is formed from Equations (3.80) and (3.83) as follows,

$$\frac{\phi_{obs,x}}{2\pi f_x} - \frac{\phi_{obs,s1}}{2\pi f_{s1}} = \delta\tau_{all} + \frac{N_x}{f_x} - \frac{N_{s1}}{f_{s1}} - kD[\frac{1}{f_x^2} - \frac{1}{f_{s1}^2}]$$

$$+[[\frac{\sigma_{\phi_{obs}}}{2\pi f_x}]] - [[\frac{\sigma_{\phi_{obs}}}{2\pi f_{s1}}]] \tag{3.114}$$

$$D = -\frac{f_{s1}^2 f_x^2}{2\pi k[f_x^2 - f_{s1}^2]}\left[\frac{\phi_{obs,s1}}{f_{s1}} - \frac{\phi_{obs,x}}{f_x} - \frac{2\pi N_{s1}}{f_{s1}} + \frac{2\pi N_x}{f_x}\right] + \frac{f_{s1}^2 f_x^2}{k[f_x^2 - f_{s1}^2]}\delta\tau_{all} + \frac{f_{s1} f_x \sqrt{f_{s1}^2 + f_x^2}[[\sigma_{\phi_{obs}}]]}{2\pi k[f_x^2 - f_{s1}^2]}. \tag{3.115}$$

The second term in the right side of Equation (3.115) means the effect of the displacement between the antennas of S-band and X-band. Assuming that the displacement of the antennas is 20cm in the case of the relay satellite of SELENE, $\delta\tau_{all}$ is $3.5 \times 10^{-12}[sec.]$ in delay difference for 2000 km baseline. The second term $\sigma_{D_{\tau_{SX}}}$ is calculated as,

$$\sigma_{D_{\tau_{SX}}} = 1.4 \times 10^{14}[el/m^2]. \tag{3.116}$$

The third term in Equation (3.115) means the phase noise errors $\sigma_{\phi_{obs}}$ in observation on the estimation of the TEC. Substitution $\sigma_{\phi_{obs}}$ of 4.3 [deg.] in Equation (3.113), the third term is given as,

$$\sigma_{D_{obs}} = 3.9 \times 10^{13}[el/m^2]. \tag{3.117}$$

From the Equations (3.116) and (3.117), the third term in Equation (3.115) is dominant than the second term. In order to improve the estimation accuracy of TEC, the displacement of the two antennas should be as small as possible.

3.4.11 Geometric delay

The geometric delay $\tau_{all,x}$ is obtained from Equation (3.83) as follows,

$$\tau_{all,x} = \frac{\phi_{obs,x} + 2\pi N_x}{2\pi f_x} - kD\frac{1}{f_x^2} + \frac{[[\sigma_{\phi_{obs}}]]}{2\pi f_x}. \tag{3.118}$$

The estimation errors $\sigma_{D_{\tau_{SX}}}$ in Equation (3.116) and $\sigma_{D_{obs}}$ in Equation (3.117) of the TEC result in the geomeric delay estimation error $\sigma_{\tau_{\sigma_D}}$ as follows,

$$\sigma_{\tau_{\sigma_D}} < 3.4 \times 10^{-13}[sec.]. \tag{3.119}$$

This error yields a small position error of 1.5 cm around the Moon for the 2000 km baseline.

Substituting Equation (3.113) to the third term, the effect of the phase noise error on the estimation of the geometric delay is obtained as,

$$\sigma_\tau = \frac{[[\sigma_{\phi_{obs}}]]}{2\pi f_x} \tag{3.120}$$

$$= 1.4 \times 10^{-12}[sec.]. \tag{3.121}$$

This error yields a small position error of 8 cm around the Moon for the 2000 km baseline.

3.4.12 Conditions of position prediction and the ionosphere to resolve the cycle ambiguity

Finally we summarize the conditions to resolve the cycle ambiguity of the carrier waves. There are four factors which affect of the cycle ambiguity. They are (1) the ionospheric fluctuation, (2) prediction accuracy of the geometric delay, (3) frequency difference between the two radio frequencies transmitted from the radio sources v_1 and v_2 and (4) frequency variations of the radio signals.

We have obtained four conditions of the ionospheric fluctuation in Equations (3.93), (3.99), (3.103) and (3.109). The most severe one is shown in Equation (3.109) as follows,

$$D \;<\; 2.3 \times 10^{15}[el/m^2]. \tag{3.122}$$

This condition can be satisfied easily, considering the results of the daily TEC variations estimated from the global GPS surveying [Tsuchiya and Tsuji 1995].

The condition of the prediction accuracy of the geometric delay is given by Equation (3.91) as follows,

$$\tau_{all,s} \;<\; 8.3 \times 10^{-8}[sec.]. \tag{3.123}$$

Validity of this condition has been discussed in Section 3.4.5.

Equation (3.69) yields a condition which includes the last two factors as follows,

$$\begin{aligned}\Big|-\pi[f^{v1}_{k,s}(t_c) - f^{v2}_{k,s}(t_c)]\left[\delta\tau^{v1}_g(t_c - T_{sw}) + \delta\tau^{v1}_g(t_c + T_{sw})\right] \\ -\pi[f^{v1}_{k,s}(t_c - T_{sw}) - f^{v1}_{k,s}(t_c)]\delta\tau^{v1}_g(t_c - T_{sw}) \\ -\pi[f^{v1}_{k,s}(t_c + T_{sw}) - f^{v1}_{k,s}(t_c)]\delta\tau^{v1}_g(t_c + T_{sw})\Big| \;<\; \sigma_{\phi_{obs}}.\end{aligned} \tag{3.124}$$

We impose conditions for the three terms in Equation (3.124) separately as the severest one. They are,

$$\Big|-\pi[f^{v1}_{k,s}(t_c) - f^{v2}_{k,s}(t_c)]\left[\delta\tau^{v1}_g(t_c - T_{sw}) + \delta\tau^{v1}_g(t_c + T_{sw})\right]\Big| \;<\; \frac{\sigma_{\phi_{obs}}}{\sqrt{3}} \tag{3.125}$$

$$\Big|-\pi[f^{v1}_{k,s}(t_c - T_{sw}) - f^{v1}_{k,s}(t_c)]\delta\tau^{v1}_g(t_c - T_{sw})\Big| \;<\; \frac{\sigma_{\phi_{obs}}}{\sqrt{3}} \tag{3.126}$$

$$\Big|-\pi[f^{v1}_{k,s}(t_c + T_{sw}) - f^{v1}_{k,s}(t_c)]\delta\tau^{v1}_g(t_c + T_{sw})\Big| \;<\; \frac{\sigma_{\phi_{obs}}}{\sqrt{3}}. \tag{3.127}$$

The terms $\delta\tau_g^{v1}(t_c - T_{sw})$ and $\delta\tau_g^{v1}(t_c + T_{sw})$ mean the prediction errors of delays for the radio source $v1$. According to error theory, $\delta\tau_g^{v1}(t_c - T_{sw})$ and $\delta\tau_g^{v1}(t_c + T_{sw})$ are related to the doubly differenced residual delay ($\tau_{all,s}$) as,

$$max[\delta\tau_g^{v1}(t_c - T_{sw})] \sim max[\delta\tau_g^{v1}(t_c + T_{sw})] \sim max[\tau_{all,s}]/\sqrt{2} \quad (3.128)$$

$$max[\delta\tau_g^{v1}(t_c - T_{sw}) + \delta\tau_g^{v1}(t_c + T_{sw})] \sim max[\tau_{all,s}], \quad (3.129)$$

where $max[x]$ is a operator which maximize the value of x. The condition of $|f_{k,s}^{v1}(t_c) - f_{k,s}^{v2}(t_c)|$ in Equation (3.125) becomes severer if we use Equations (3.128) and (3.129) as,

$$\left|f_{k,s}^{v1}(t_c) - f_{k,s}^{v2}(t_c)\right| < \frac{\sigma_{\phi_{obs}}}{\sqrt{3}\pi max\left[\delta\tau_g^{v1}(t_c - T_{sw}) + \delta\tau_g^{v1}(t_c + T_{sw})\right]} \quad (3.130)$$

$$< \frac{\sigma_{\phi_{obs}}}{\sqrt{3}\pi\ max[\tau_{all,s}]}. \quad (3.131)$$

Substituting actual values into Equations (3.124) and (3.113), we obtain the condition of the frequency difference as follows,

$$\left|f_{k,s}^{v1}(t_c) - f_{k,s}^{v2}(t_c)\right| < 170\ [kHz]. \quad (3.132)$$

Radio transmitters on spacecrafts should be designed to satisfy this condition.

On the other hand, $f_{k,s}^{v1}(t_c - T_{sw}) - f_{k,s}^{v1}(t_c)$ and $f_{k,s}^{v1}(t_c - T_{sw}) - f_{k,s}^{v1}(t_c)$ in Equations (3.126) and (3.127) means frequency variations in the duration of T_{sw}. In general, a frequency variation Δf can be roughly expressed with normalized frequency stability $y(\tau)$ as follows

$$\Delta f = y(\tau)f, \quad (3.133)$$

where τ is a duration and f is a frequency. In order to estimate the effect of the frequency variations, we introduce the following approximations,

$$|f_{k,s}^{v1}(t_c - T_{sw}) - f_{k,s}^{v1}(t_c)| \sim y(T_{sw})f_{k,s}^{v1} \quad (3.134)$$

$$|f_{k,s}^{v1}(t_c + T_{sw}) - f_{k,s}^{v1}(t_c)| \sim y(T_{sw})f_{k,s}^{v1}. \quad (3.135)$$

Substituting them into Equations (3.126) and (3.127), we obtain the following conditions as

$$\left|-\pi y(T_{sw})f_{k,s}^{v1} max[\delta\tau_g^{v1}(t_c - T_{sw})]\right| < \frac{\sigma_{\phi_{obs}}}{\sqrt{3}} \quad (3.136)$$

$$\left|-\pi y(T_{sw})f_{k,s}^{v1} max[\delta\tau_g^{v1}(t_c + T_{sw})]\right| < \frac{\sigma_{\phi_{obs}}}{\sqrt{3}}. \quad (3.137)$$

Since $max[\delta\tau_g^{v1}(t_c + T_{sw})] \sim max[\delta\tau_g^{v1}(t_c - T_{sw})]$ as shown in the Equation (3.128), the two conditions are the same. Finally the condition of frequency variations is summarized as follows,

$$\left|y(T_{sw})f_{k,s}^{v1}\right| < 2.4 \times 10^5[Hz] \quad (3.138)$$

$$y(T_{sw}) < 2.8 \times 10^{-5}[Hz/Hz]. \quad (3.139)$$

where $f_{k,s}^{v1} = 8456MHz$ is used. Radio transmitters on spacecrafts should be designed to satisfy also this condition.

Chapter 4

Application of Multi-frequency VLBI

Multi-frequency VLBI method described in Chapter 3 will be applied to an actual space mission. The mission is VRAD (VLBI RADio source) mission of SELENE (SELenological and ENgineering Explore) project. Ground system for multi-frequency VLBI has been developed under the project. The system consists of a hardware to sample and record the four carrier waves, a software to estimate phase delays and an interface between the estimated phase delay and a software for gravity field and orbit estimation.

4.0.13 Multi-frequency VLBI method in SELENE project: VRAD mission

A Moon-orbiting mission SELENE is prepared as a joint space program by ISAS (The Institute of Space and Astronautical Science) and NASDA(National Space Development Agency of Japan) for lunar science and technology development for future lunar exploration. The SELENE mission is summarized in Table 4.1, and the mission profile is shown in Figure 4.1 [SELENE project team 2000]. The spacecraft will be launched by Japanese H-IIA rocket and will reach the lunar orbit in about 5 days. The spacecraft is captured by the Moon into an elliptical orbit with apolune at 15,000 km and perilune at 100 km. The apolune is lowered by 6 orbit-transfer maneuvers and finally the orbiter reaches the mission orbit at about 100 km altitude. During the orbit transition, a relay satellite is released from the main orbiter in an elliptical orbit with the apolune at 2,400 km and the VRAD satellite in an elliptical orbit with the apolune at 800 km. Three lunar orbiters share the same polar orbit plane. Upon arriving at the mission orbit, the main orbiter extends antennas for radar sounder experiments and a mast for mag-

netometers. Remote-sensing observations of the lunar surface and observations of the lunar and the solar-terrestrial environment will be performed for one year. If extra fuel to keep and control the orbit is available, the mission will be extended for optional observations. One option is to lower the orbiter to 50-70 km altitude for observations with a higher resolution.

Table 4.1: SELENE system summary

Launch	H-IIA Launch in 2005 from Tanegashima
System	Main orbiter (2 x 2 x 4.2 m), Relay satellite and VRAD satellite (1 m ϕ x 0.65 m)
Orbit	Direct injection to the lunar transfer orbit 100 km circular, Inclination 90°(Main orbiter) 100 km x 2400 km elliptical, Inclination 90° (Relay satellite) 100 km x 800 km elliptical, Inclination 90° (VRAD satellite)
Mission Period	1 year nominal plus optional observation
Attitude Control System	Main orbiter: 3-axis control, 2 Star sensors, 2 IMUs, 4 Sun sensors 4 Reaction wheels(20 Nms), Pointing $\pm 0.1°(3\sigma)$, Determination $\pm 0.025°(3\sigma)$ Stability $\pm 0.003°/s(3\sigma)$ Relay/VRAD satellite: Spin stabilization(>10 rpm)
Thruster System	Main orbiter: 500 N x 1, 20 N x 12, 1 N x 8
Power System	Main orbiter: GaAs solar array paddle 3.5 kW, Battery Ni-H2, 50 AH x 3, 50 V Relay/VRAD satellite: High efficiency Si Solar Cell 70 W, NiMH 13 AH, 26 V
Communication System	Mian orbiter: S and X bands, High gain antenna(S, X), 2 Omni antennas (S), 10 Mbps(X downlink), 40 or 2 kbps(S downlink), 1 kbps(uplink) Relay/VRAD satellite:128 bps
Orbiter Data Recorder	Main orbiter: 10 GBytes
Weight	Launch 2885 kg Orbiter(Dry Weight) 1660 kg Science Payload 270 kg(approx) Relay Satellite 40 kg VRAD Satellite 40 kg

VRAD, one of the missions of SELENE, installs two radio sources on the relay satellite (VRAD-1) and the VRAD satellite (VRAD-2) respectively, and we measure the angular distance between them so as to observe the lunar global gravitational fields. A specially dedicated receiving and recording system receives carrier

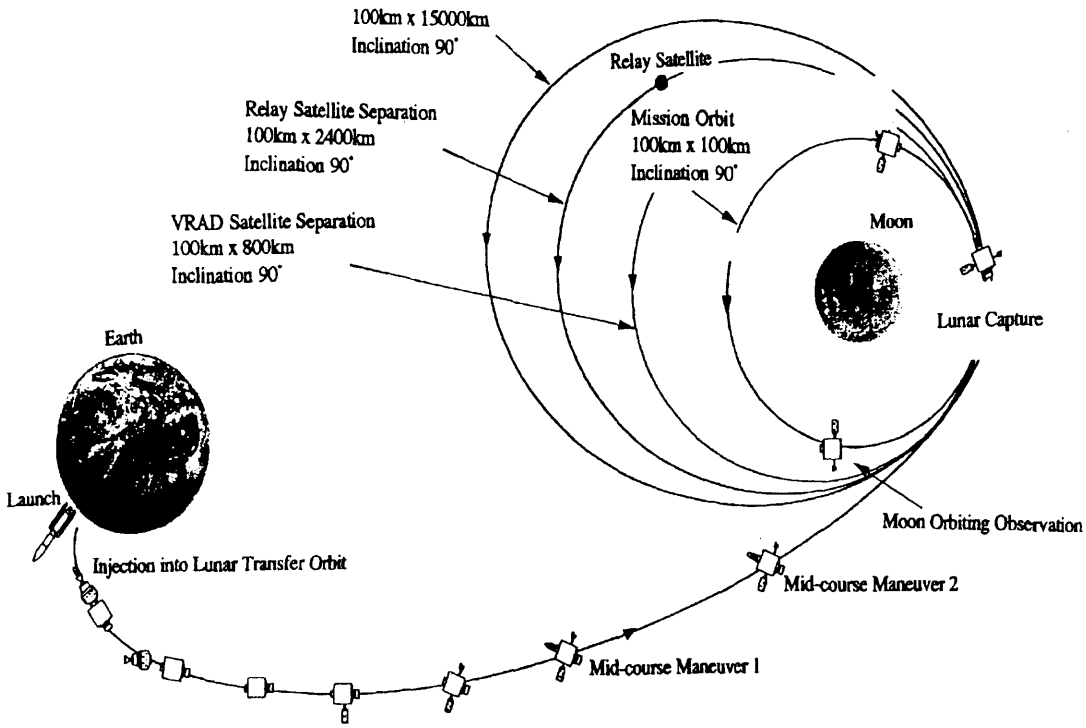

Figure 4.1: SELENE mission profile

waves from the radio sources through VLBI antennas and measures phase differences between them within an error of 4 degrees at X-band. In order to resolve cycle ambiguities with optimum frequency spacing, both VRAD-1 and VRAD-2 emit three carrier waves in S-band and one wave in X-band. A VLBI network with 2000 km baseline can determine a phase delay with accuracy of 1.4 pico-second if we measure the phase of carrier waves in X-band with 0.08 rad.(4 degrees) sensitivity, which is equivalent to the accuracy in angular distance of 2.3×10^{-10} radian or the accuracy in the position on the Moon of about 8 cm, through the relation

$$\Delta d = c\sigma_\phi A/(2\pi f D), \tag{4.1}$$

where Δd is accuracy in position of a radio source on the Moon, c is the light velocity in vacuum, σ_ϕ is the error for phase delay measurements, A the distance between the Earth and the Moon, f is frequency of the continuous wave and D is baseline length, respectively [Kawano et al., 1994].

Transmitting power of VRAD necessary for VLBI measurements is estimated from the relation between the fringe phase error σ_ϕ for each radio source and the flux density of the sources S_c ($\mathrm{Wm^{-2}Hz^{-1}}$) as

$$\sigma_\phi = \frac{8k}{\pi S_c D_1 D_2 h}\sqrt{\frac{BT_1T_2}{2(\Delta\nu)^2 t\eta_1\eta_2}}, \tag{4.2}$$

where k is Boltzmann's constant ($k = 1.38 \times 10^{-23}\mathrm{JK^{-1}}$), B is recorded bandwidth (Hz), T_i is system temperature at each station (K), D_i is diameter of each antenna (m), h is coherence factor, $\Delta\nu$ is bandwidth of the signal (Hz), t is integration time (sec.), and η_i is aperture efficiency of each antenna. The source flux density of $S_c = 1.2 \times 10^{-23}\mathrm{Wm^{-2}Hz^{-1}}$ (1200Jy) is necessary for $\sigma_\phi = 0.05$ ($4/\sqrt{2}$ degrees) in X-band with $B = 140$Hz, $T_i = 380$K, $D_i = 20$m, $h = 0.95$, $\Delta\nu = B$, $t = 100$s, and $\eta_i = 0.35$. The values of the parameters are based on VERA antenna of 20 meter in diameter of National Astronomical Observatory, Mizusawa [Honma et al., 2000]. The system temperature includes the contribution from the Moon of 200K which is the surface temperature of the Moon at noon. The total flux on the Earth becomes $F = S_c \times \Delta\nu = 1.7 \times 10^{-21}\mathrm{Wm^{-2}}$, which corresponds to the equivalent isotropic radiated power (e.i.r.p) of $P = 4\pi F l^2 = 38m\mathrm{W}$ with the distance between the Earth and the Moon of $l = 3.8 \times 10^8$m, taking an atmospheric absorption loss and a rain loss which amount to -5.8dB in all and the link margin of 5.1dB into consideration. The radiated power of the carrier wave in X-band required for the transmitter of VRAD-2 becomes 60 mW, considering the feed loss of -2dB.

The radiated power per carrier wave at S-band, on the other hand, becomes 100mW when estimating by using the same parameters as X-band except $\eta_i = 0.14$ and $T_i = 267$K which includes the contribution from the Moon of 94K with

a half power beam width of 0.4 degrees. These link designs are described in [Hanada et al., 2001].

4.0.14 Receiving system

The carrier waves at S and X-bands received by a VLBI antenna are converted into video signals by the K-4 system which is equivalent to the Mark-III system like the conventional VLBI experiment [Kiuchi et al., 1993]. In order to reduce the amount of data and to store them in a narrow bandwidth recorder developed for VRAD experiments, the bandwidth of the video signals is made to be narrower than those of a K-4 video convertor. The orbital motion of the relay satellite, the orbital motion of the Moon and the rotation of the Earth cause Doppler shift of the frequency which is proportional to the relative velocity between VRAD and the VLBI antenna. The maximum frequency variations estimated for VRAD are listed in Table 4.2. The bandwidths of 40kHz and 120kHz are necessary for S and

Table 4.2: The maximum change in Doppler frequency of VRAD

	Earth Rotation	Moon revolution	Motion of the Satellites
line-of-sight velocity	$380ms^{-1}$	$56ms^{-1}$	$2.02kms^{-1}$
S-band	2.8kHz	0.4kHz	14.8kHz
X-band	10.7kHz	1.6kHz	56.6kHz

X-band, respectively, due to the Doppler shift. The dedicated recorder (S-RTP Station, System Design Service Corp.) with 5 channels (4 channels for the video signals of the four carrier waves and one for a reference clock signal) samples and digitizes the video signals at 200kHz sampling frequency with 6 bit resolution and stores them into an 8 mm magnetic data tape with the maximum capacity of 20 Gbytes which is equivalent to the data of 7.4 hours (see, Figure 4.2 and Figure 4.3). Although the recorder has the bandwidth of only about 60kHz through a low pass filter (see, Figure 4.4) of 70kHz cutoff frequency and of -24dB/oct slope, the bandwidth of the video signal be restricted within about 50kHz. The local oscillator of the video converter adjusts the receiving frequency according to the Doppler shift.

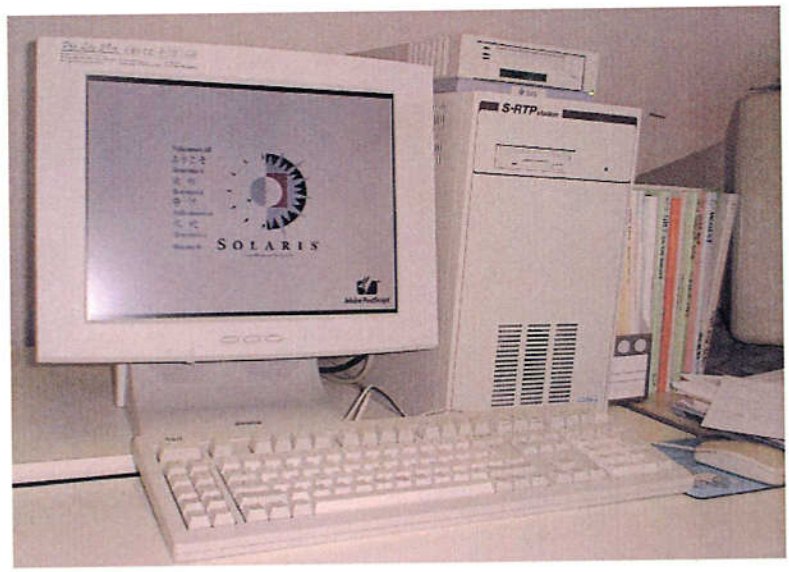

Figure 4.2: The dedicated VLBI terminal 'SRTP Station'

Figure 4.3: The backside of the dedicated VLBI terminal 'SRTP Station'

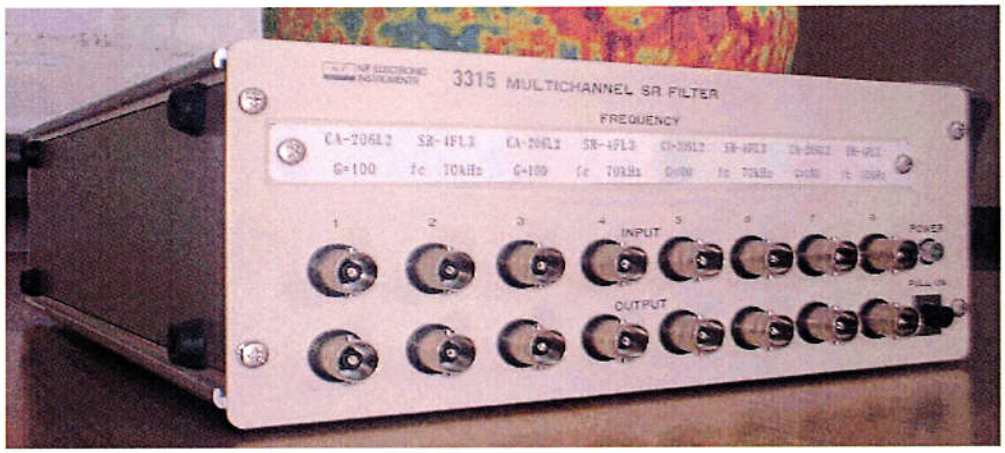

Figure 4.4: The low-pass-filter of the dedicated VLBI terminal

4.0.15 Correlation software

Data processing software system has been also developed. The software system carries out data processing to estimate the phase delay from the raw data recorded in 8 mm magnetic tapes. Phase delays obtained are converted to binary format for GEODYN-II which is the big software for the estimation of orbital elements of a spacecraft, gravity fields, etc. The flow of the data processing is shown in Figure 4.5. The computer system in which the software is installed and used for the data processing of the Experiment of Lunar Prospector is shown in Figure 4.6 [1].

[1] http://www.miz.nao.ac.jp/coop.html#Cooperation

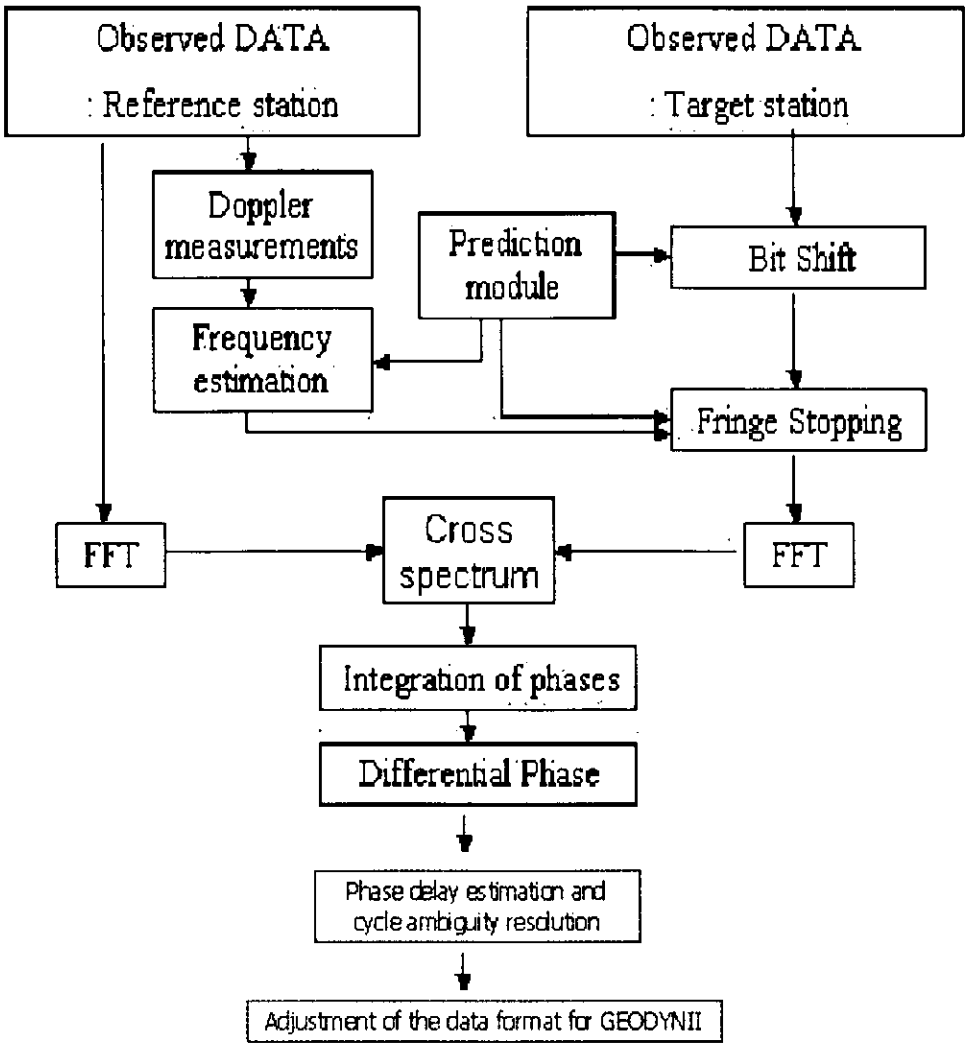

Figure 4.5: The data processing flow

Figure 4.6: The Computer system for the data analysis, IBM RS6000/SP

Chapter 5

Preliminary Experiment of multi-frequency VLBI by Lunar Prospector

5.1 Objective

As a test of the whole system, a carrier signal transmitted from Lunar Prospector was received at three VLBI ground stations.The fringe phase tracking of the carrier wave is performed to test the developed VLBI observation system and the phase delay estimating software [Kono et al., 2000].

5.2 Observation profile

The VLBI observation of Lunar Prospector was carried out from 08:00 to 17:00 in Sep. 21, 1998 (in Japan Standard Time). Target radio sources are Lunar Prospector and a nearby QSO (Quasi-Stellar Object). Lunar Prospector is one of the NASA Discovery Program missions[1]. A figure of Lunar Prospector is shown in Figure 5.1. Lunar Prospector was designed to perform observations in a low polar orbit of the Moon. They include mapping of the surface composition, location of lunar mineral resources, measurements of magnetic and gravity fields, and study of outgassing events. The various kinds of data from this mission complemented the image data from the Clementine mission which carried mainly cameras. The information gathered by the mission improved understanding of the origin, evolution and current state of the Moon.

Lunar Prospector transmits one carrier signal with frequency of 2273 MHz in S-band. The QSO, 3C273B was also observed as a reference source. This QSO was

[1]quated from web site: http://www.lpi.usra.edu/expmoon/prospector/prospector.html and http://discovery.nasa.gov/ as of Dec. 22, 2001

selected so that the angular distance from Lunar Prospector is short enough in the celestial sphere. The angular distance between the two radio sources during the observation period is shown in Figure 5.2. The antennas involved in the observa-

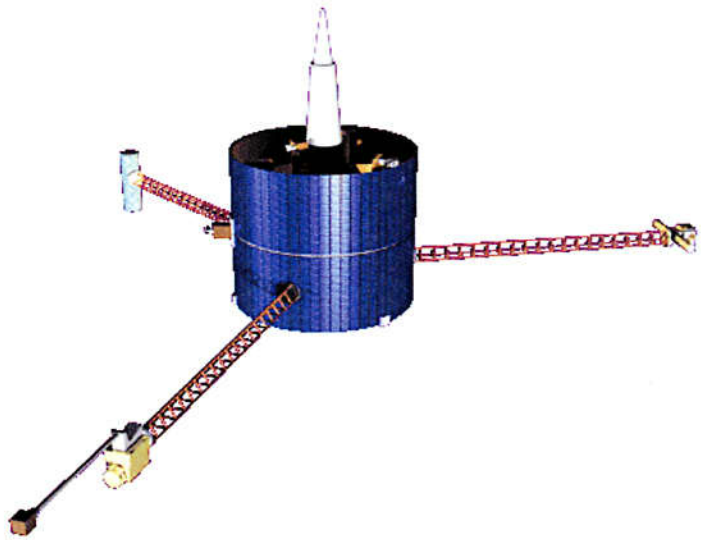

Figure 5.1: Lunar Prospector

tion were the Kashima 34m-diameter antenna at Kashima Space Research Center of Communications Research Laboratory (CRL), the Mizusawa 10m-diameter antenna at Mizusawa Astrogeodynamics Observatory of National Astronomical Observatory (NAO) and the Tsukuba 3.8m-diameter antenna at Geographical Survey Institute (GSI). The configuration of the VLBI stations are shown in Figure 5.3.

The system described in Chapter 4 was used for receiving and recording the radio signals. After two frequency conversions, received signals were recorded by two kind of recorders as shown in Figure 5.4. The signal of Lunar Prospector was recorded by the narrow-bandwidth recording system which is described in Chapter 4, and the signal from QSO was recorded by the conventional VLBI system, K-4 system with the bit rate of 64 Mbps. The recording and data acquisition system for Lunar Prospector is shown in Figure 5.5. An example of a spectrum of the signal from Lunar Prospector received at the Kashima 34m-diameter antenna is shown in Figure 5.6.

5.3 Data processing

Data processing was done by using the developed software described in Chapters 3 and 4. Cross correlation between signals from Lunar Prospector obtained at

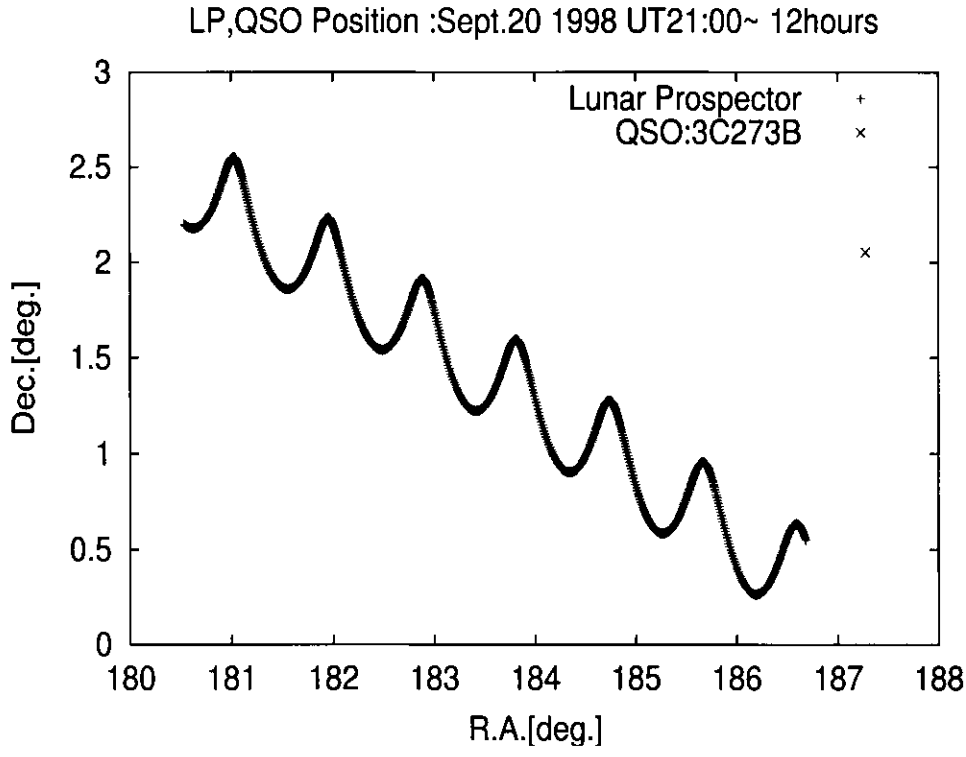

Figure 5.2: Angular distance between Lunar Prospector and QSO 3C273B during the observation

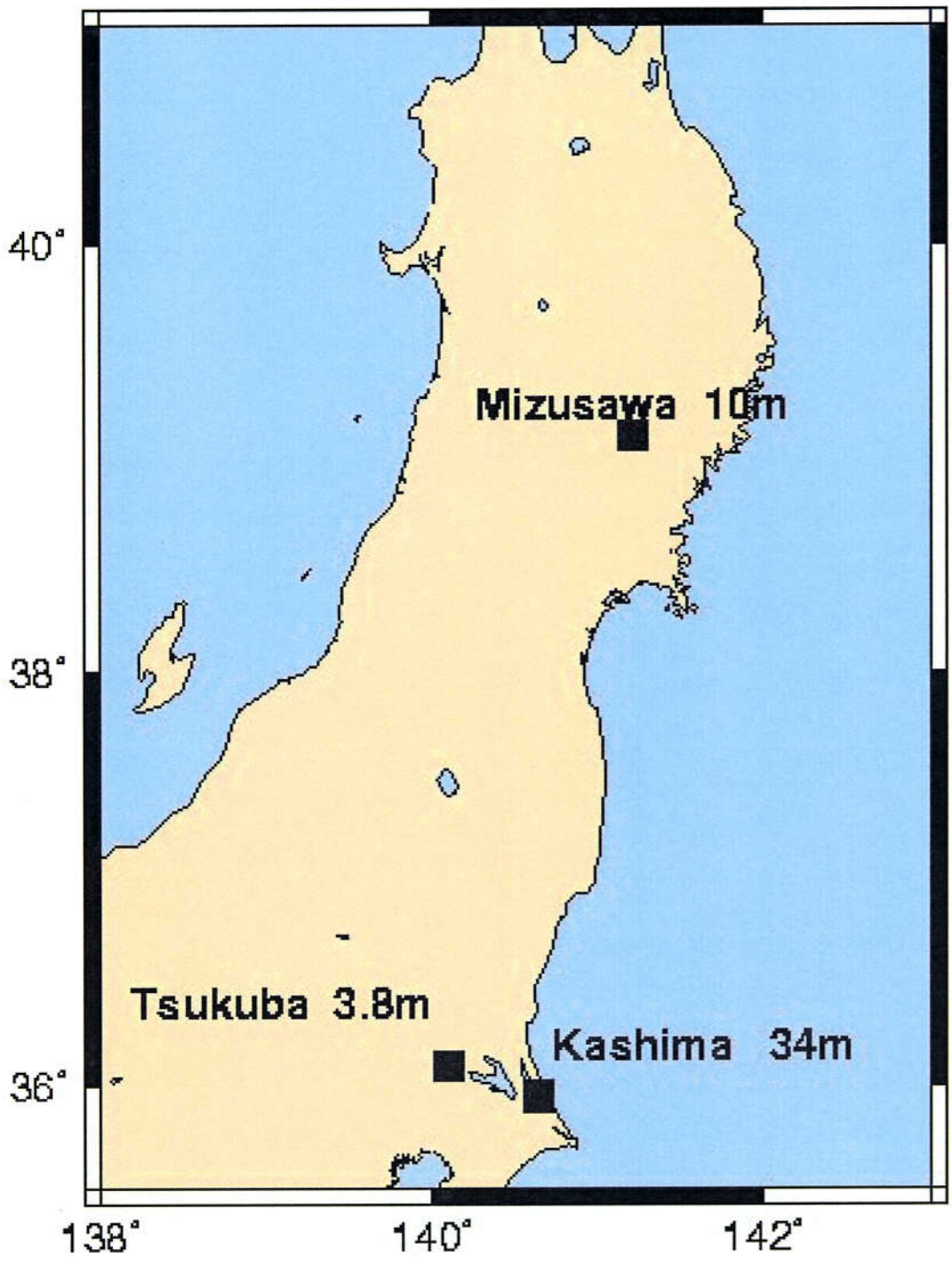

Figure 5.3: Configuration of the VLBI stations involved in the Lunar Prospector experiment

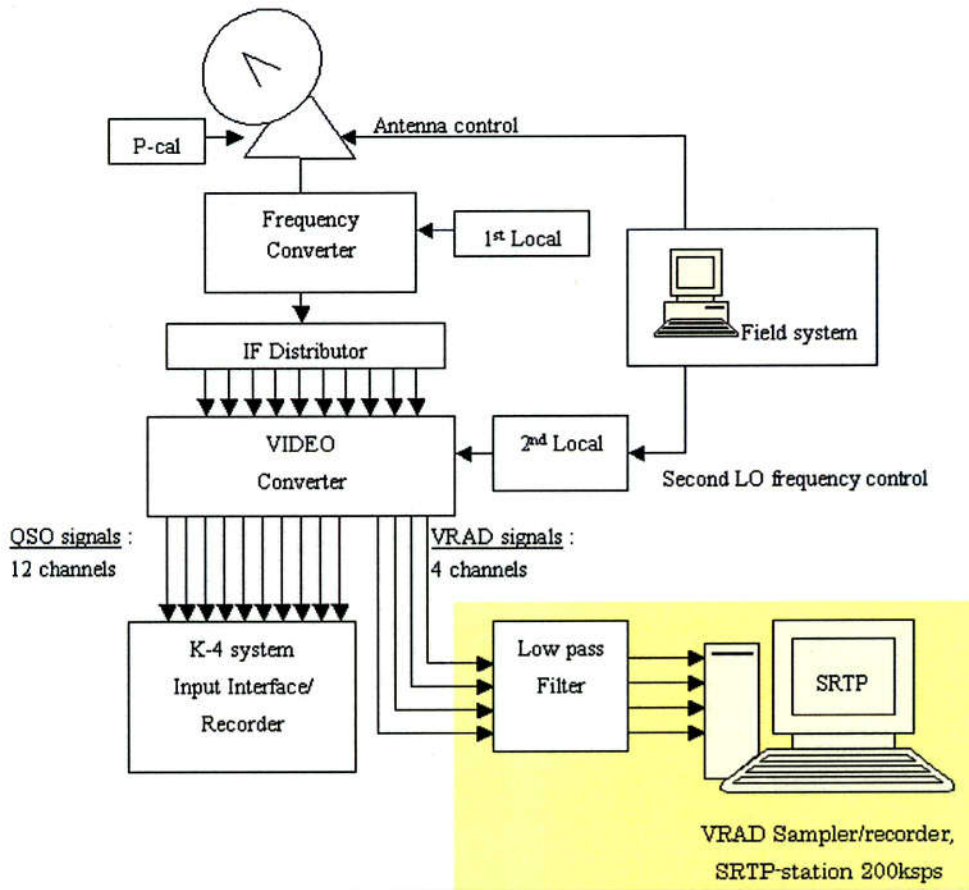

Figure 5.4: The VLBI system of the Lunar Prospector experiment

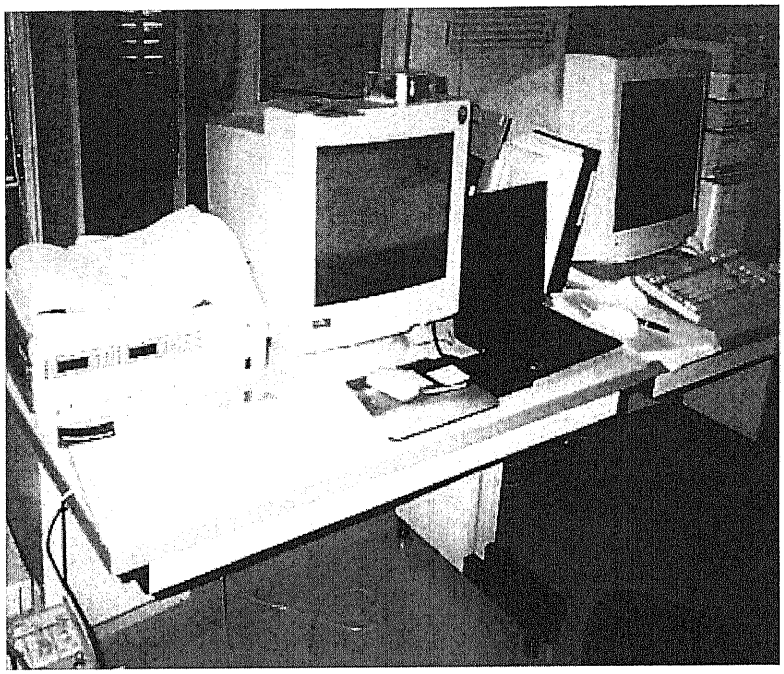

Figure 5.5: Recording and data acquisition system

Kashima 34m-diameter antenna and those of Mizusawa 10m-diameter antenna was processed.

5.3.1 Prediction of the geometric delay

The first step in processing the observed data is prediction of a geometric delay. As mentioned in Chapter 3, error of the predicted geometric delay should be less than 8.3×10^{-8} seconds to resolve the ambiguity in the first wide lane [s1-s2] of the Multi-Frequency VLBI. It depends on various kind of models used, for example, the Earth rotation, lunar gravity field, an ephemeris of the Moon etc as well as orbital elements of the spacecraft. The models for the prediction is summarized in Table 5.1. The ephemeris[2] of Lunar Prospector was calculated for the period nearest to the observation period (00:00, Sep. 21, 1998 in Universal Time Coordinated (UTC)).

[2]the internet address is http://wufs.wustl.edu/missions/lunarp/

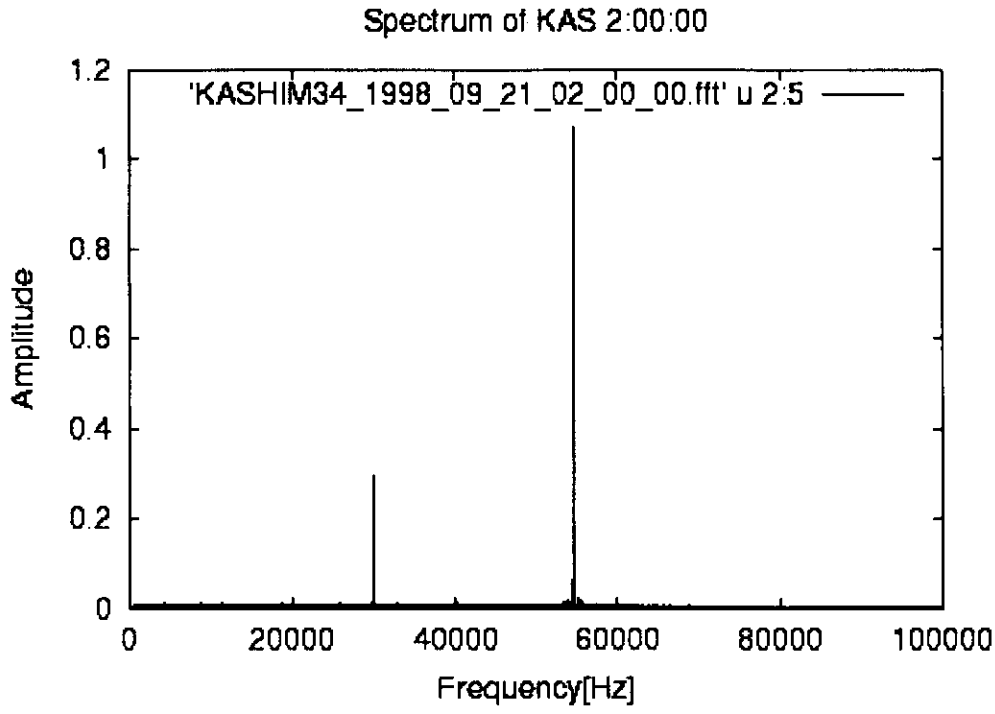

Figure 5.6: Spectrum of Lunar Prospector's signal received at Kashima 34m-diameter antenna. The largest peak shows the signal from Lunar Prospector and the other is a phase calibrator signal.

Table 5.1: The models and the software used to predict the geometric delay

Positions of ground stations	ITRF1997
Parameters of precession and nutation	IERS Conventions1996
EOP	IERS Bulletin A
Initial orbital parameters of LP	Definitive ephemeris on a website
Software for orbits estimation	GEODYN-II
The lunar gravity field	LP75G
Ephemeris of the Moon	DE403

5.3.2 Cross correlation

Cross correlation between signals recorded at Kashima 34m-diameter antenna as a reference station and those at Mizusawa 10m-diameter antenna as a slave station has been carried out. In the processing, the integration period is set at about 1.3 seconds which corresponds to 262,144 time-series data. Although interval of antenna switching is 120 seconds, successive data for only about 90 seconds are processed eliminating data for antenna slew time loss of 30 seconds.

The residual fringe phases from 01:00 to 07:00 on Sep. 21, 1998 in UTC are shown in Figure 5.7. A series of the successive residual fringe phases for 90 seconds could be connected continuously for about one hour, a half period of Lunar Prospector's orbit, by the following way. We obtained the residual fringe phase for the first period of 90 seconds with the cycle ambiguity, and then calculated its derivative in time. The derivative enabled us to predict the next successive residual fringe phases 240 seconds later. The residual fringe phase in the second period, therefore, could be determined nearest the predicted phase. The third residual fringe phase could be also determined from the derivative of the residual fringe phase in the second period in the same way, and finally a series of successive residual fringe phases were determined without ambiguity of 2π for about one hour of the path. Although a series of residual fringe phases were obtained, we could not estimate the cycle ambiguity of the residual fringe phases in the first period because Lunar Prospector emitted only one carrier wave. If Lunar Prospector had transmitted four carrier waves of appropriate frequencies mentioned in Chapter 3, we could have resolved the cycle ambiguity and obtained phase delay without ambiguity of 2π for all the period.

We can find linear trend in Figure 5.7. This trend seems to be the effect of clock rate which comes from frequency difference between frequency standards at the two VLBI stations. This trend corresponds to 13 ps/s of the clock rate. Subtracting the linear component from the trend, the residuals are obtained in Figure 5.8. There remains a variation of fringe phases with a period around a few thousand seconds.

5.4 Correction for the ionospheric fluctuation

Fringe phases are fluctuated by the troposphere as well as the ionosphere. The tropospheric fluctuation has been studied so far [e.g., Rogers et al., 1981, Asaki et al., 1996, Kawaguchi et al., 2000]. The Allan standard deviation of the tropospheric fluctuation reported by Rogers et al. (1981) is shown in Figure 5.9. From this figure, the tropospheric phase fluctuation for 1000 second period is esti-

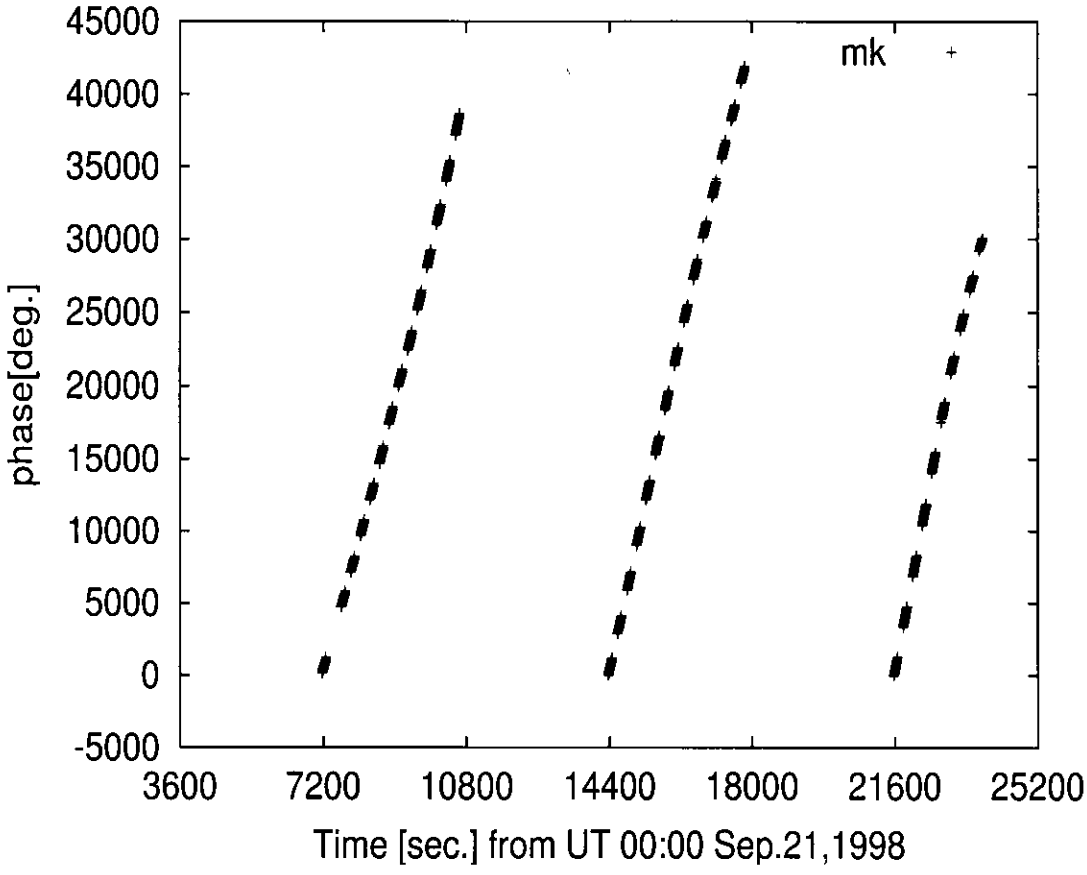

Figure 5.7: Residual Fringe phases

mated at a few degrees. This fluctuation is almost cancelled out in the differential VLBI [e.g., Asaki et al., 1996], so that we do not consider the tropospheric fluctuation as a source which causes the fluctuation shown in Figure 5.8 in this section.

In order to correct the ionospheric fluctuation, GPS observations are useful. Recently, global IGS (International GPS Service) sites have begun to monitoring of the ionosphere, and have opened results to the public. The Center for Orbit Determination in Europe (CODE), University of Berne, Switzerland has modeled the TEC with a spherical harmonic expansion up to twelve degrees and eight orders at every two hours referring to the solar-geomagnetic reference frame. An example of the TEC snapshot is shown in Figure 5.10[3]. The TEC's at Kashima and Mizusawa along the line-of-sight of Lunar Prospector can be calculated from coefficients of the TEC model, and the result are shown in Figure 5.11. The difference between ionospheric phase fluctuation at Kashima and that of Mizusawa calculated from the TEC's are shown in Figure 5.12. Finally the residual fringe

[3]http://www.aiub.unibe.ch/ionosphere.html

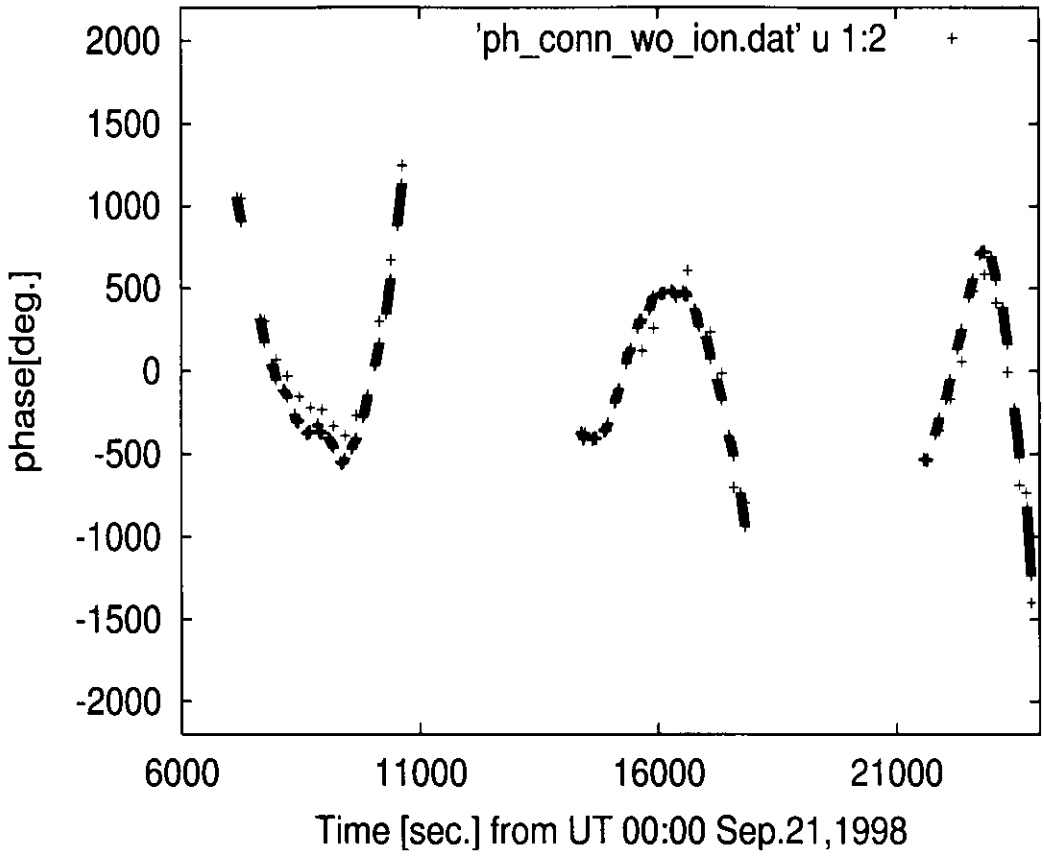

Figure 5.8: Residual fringe phases. Linear components are removed.

phase variation is corrected for the ionospheric fluctuation, as shown in Figure 5.13.

5.5 Modification of the initial orbit by the residual fringe phases

In order to investigate effects of the initial orbit error, we calculate the residual fringe phase by adding some small offset to each initial orbital element. This processing makes it possible to judge if there are errors in the initial orbital elements roughly. The offsets added to the initial orbital elements are listed in Table 5.2. Figure 5.14 through Figure 5.25 show how to the offset affect the residual fringe phase.

As the results shown in Figure 5.14 through Figure 5.25, the variation is minimized for the orbital element of $\Omega + 0.08$ degrees (see Figure 5.20).

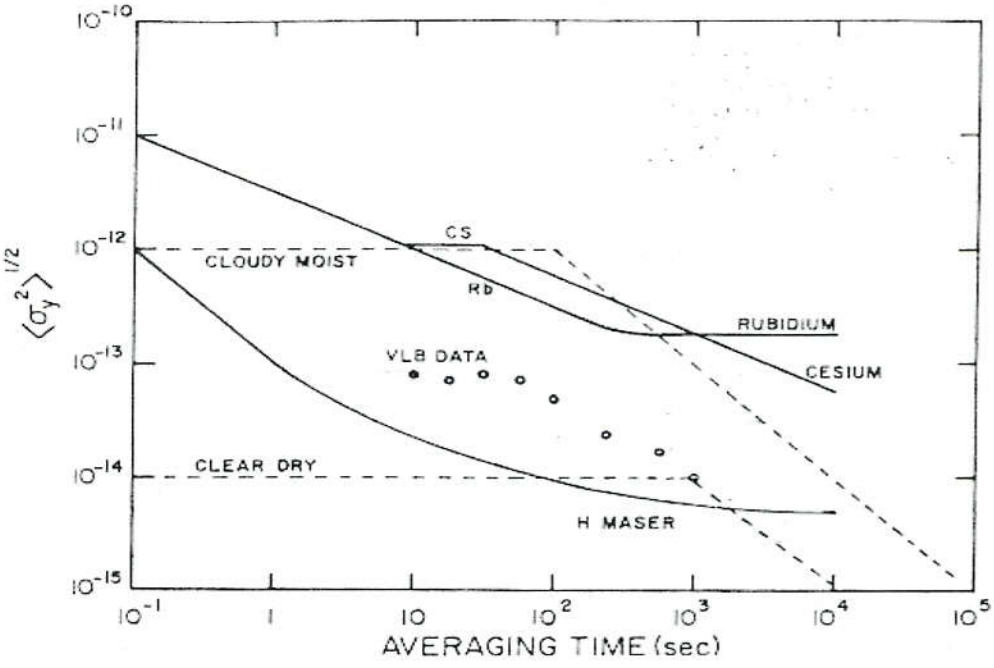

Figure 5.9: Allan standard deviations of the frequency standards and the tropospheric fluctuation.

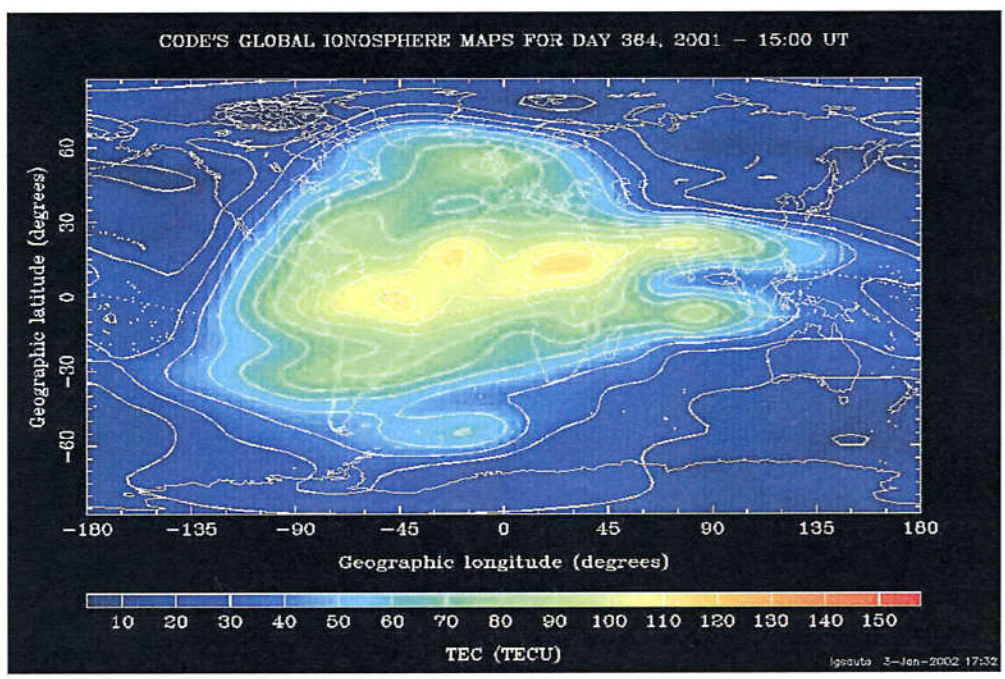

Figure 5.10: An example of Global TEC Model by CODE

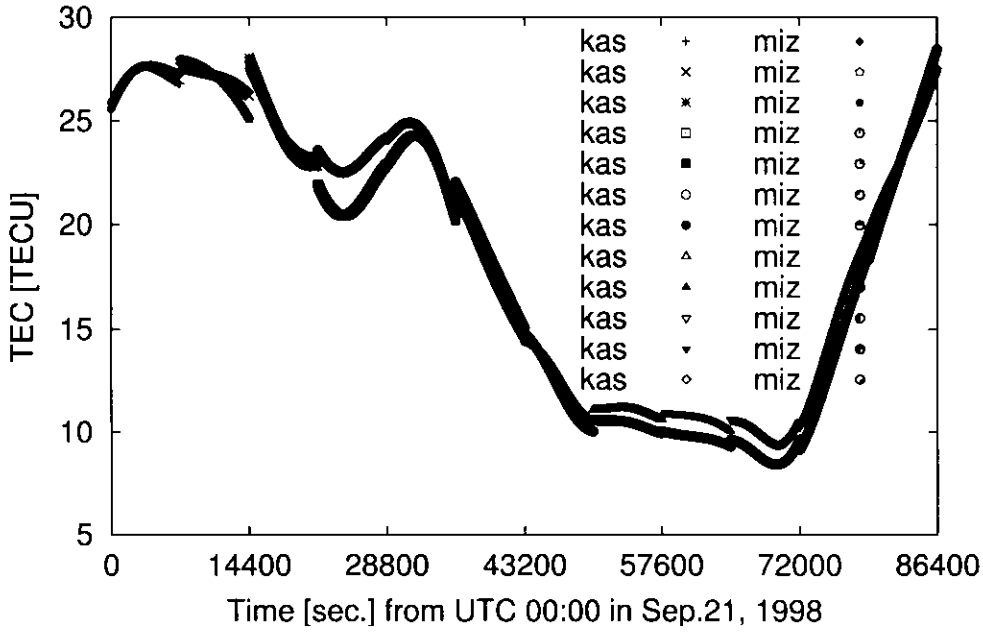

Figure 5.11: TEC values in line of sight to the Lunar Prospector from each station

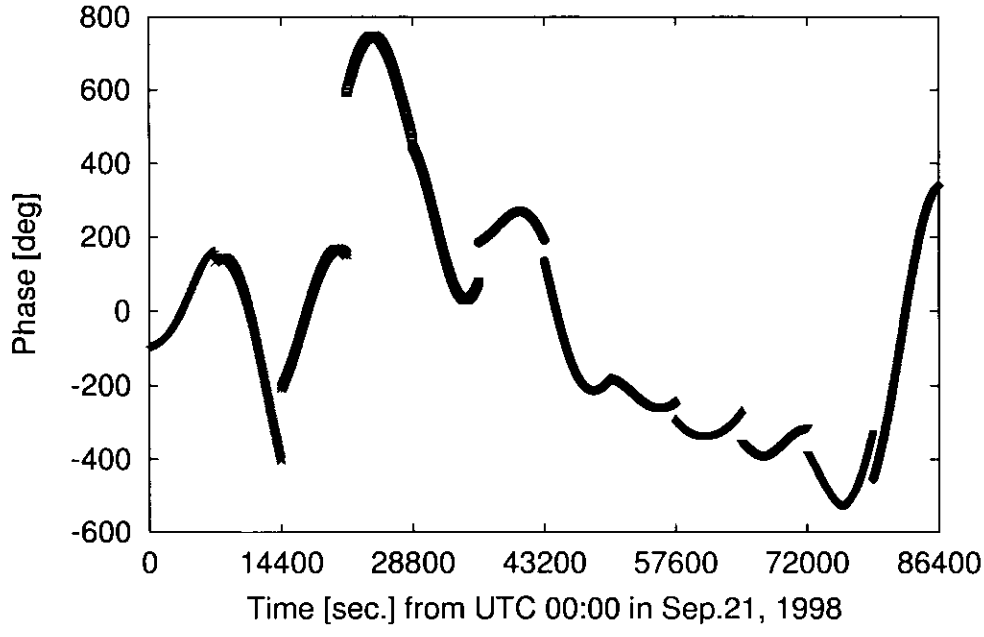

Figure 5.12: Residual fringe phase variations perturbed by TEC

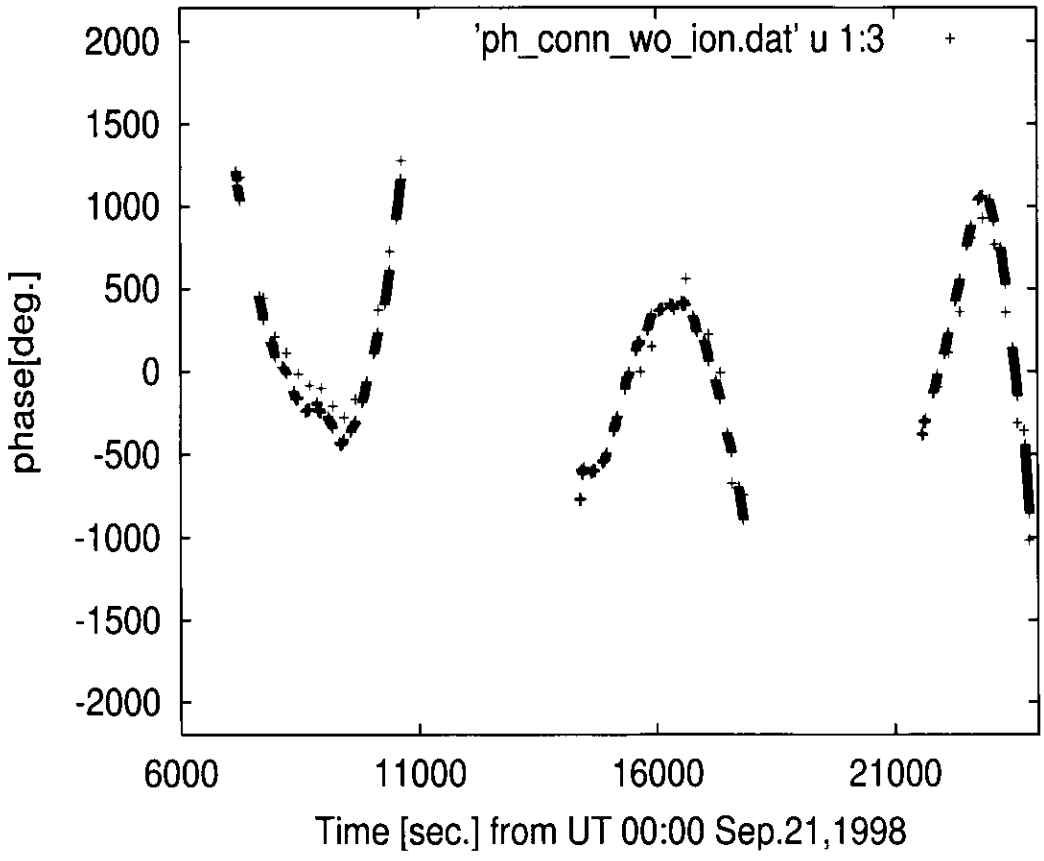

Figure 5.13: Residual fringe phases after the correction of the ionospheric fluctuation

5.6 The short period variation of the residual fringe phase

Finally, the precision of the residual fringe phase determined by the developed hardware and software is estimated. The precision can be essentially obtained by residual fringe phases after fit by models which include orbital elements, the lunar gravity field, EOP and so on. Unfortunately the orbital elements and the gravity field could not be estimated in this experiment, and therefore we cannot strictly estimate the precision of this system. If the orbital elements and the lunar gravity field are estimated and if all the models used in this analysis software such as EOP has enough accuracy, any long period variation will disappear from the residual fringe phase, and therefore we can try to calculate the short period variation in the residual fringe phases. An example of the residual after removal of long period variation is shown in Figure 5.26. The short periodic residual fringe phase variations in all observation period are shown in Figure 5.27. The RMS

Table 5.2: List the offsets of the initial orbital elements and the figure of the results

Orbital elements	offset	unit	result
Semi-major axis of ellipse (A)	+50	[m]	Figure 5.14
	-50	[m]	Figure 5.15
Eccentricity (e)	+0.0003		Figure 5.16
	-0.0003		Figure 5.17
Inclination (I)	+0.02	[deg.]	Figure 5.18
	-0.02	[deg.]	Figure 5.19
Longitude of ascending node (Ω)	+0.08	[deg.]	Figure 5.20
	-0.08	[deg.]	Figure 5.21
Mean Anomaly (M.A.)	+0.02	[deg.]	Figure 5.22
	+0.04	[deg.]	Figure 5.23
Ω & M.A.	+0.08 -0.02 (respectively)	[deg.]	Figure 5.24
Ω & M.A.	+0.08 +0.02 (respectively)	[deg.]	Figure 5.25

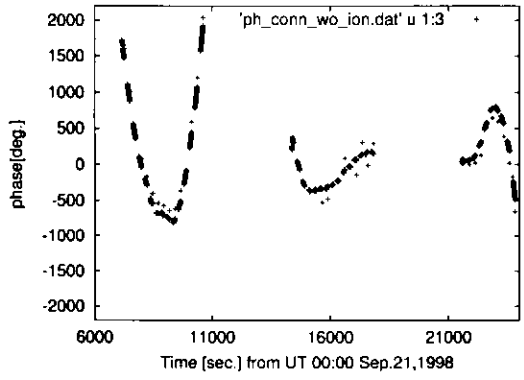

Figure 5.14: Residual fringe phase for the orbital element offset: A+50 [m]

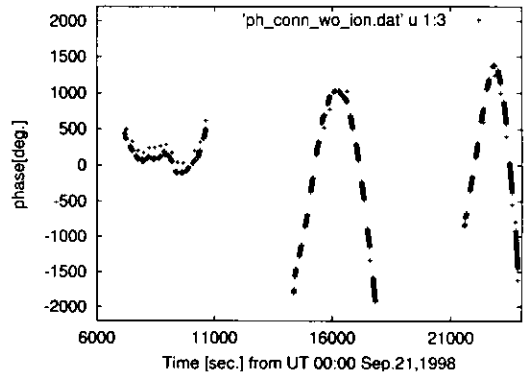

Figure 5.15: Residual fringe phase for the orbital element offset: A-50 [m]

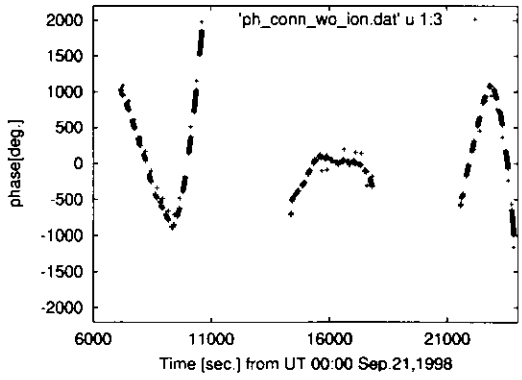

Figure 5.16: Residual fringe phase for the orbital element offset: e +0.0003

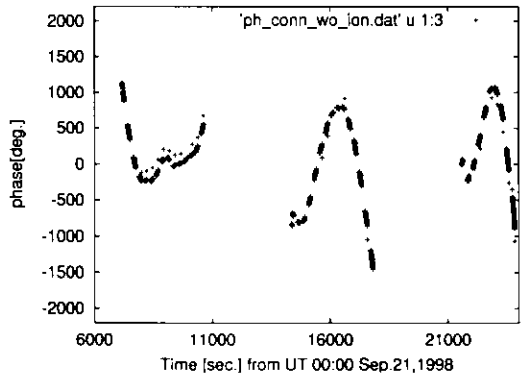

Figure 5.17: Residual fringe phase for the orbital element offset: e -0.0003

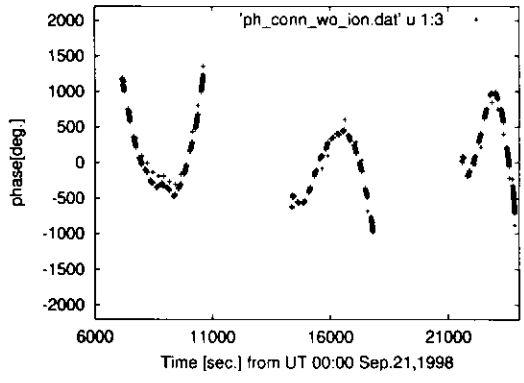

Figure 5.18: Residual fringe phase for the orbital element offset: I +0.02 [deg.]

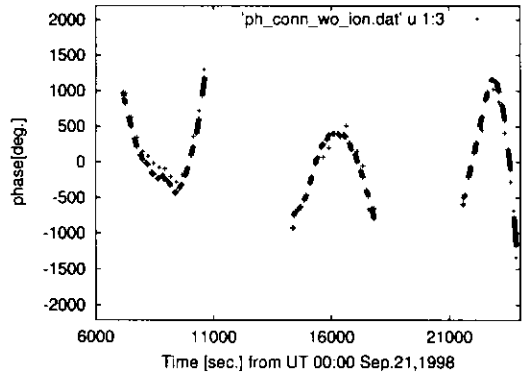

Figure 5.19: Residual fringe phase for the orbital element offset: I -0.02 [deg.]

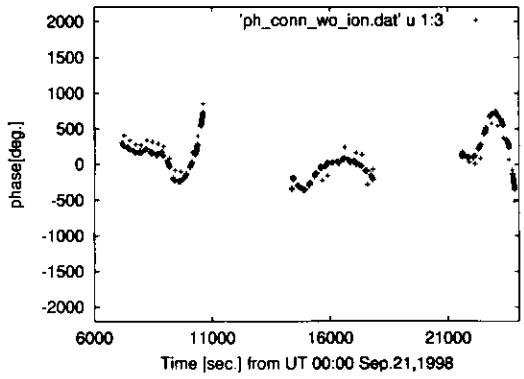

Figure 5.20: Residual fringe phase for the orbital element offset: Ω+0.08 [deg.]

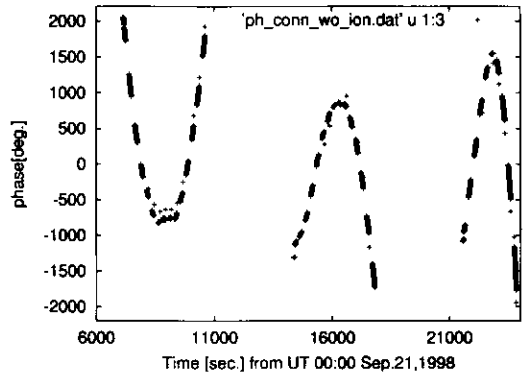

Figure 5.21: Residual fringe phase for the orbital element offset: Ω-0.08 [deg.]

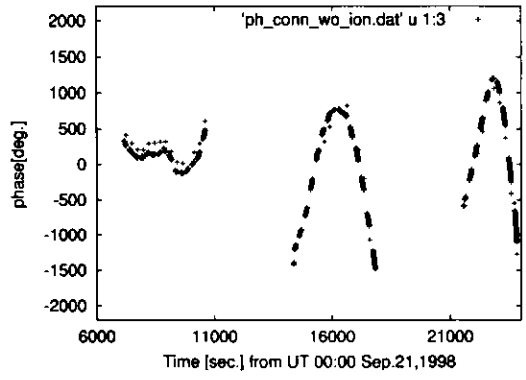

Figure 5.22: Residual fringe phase for the orbital element offset: MA+0.02 [deg]

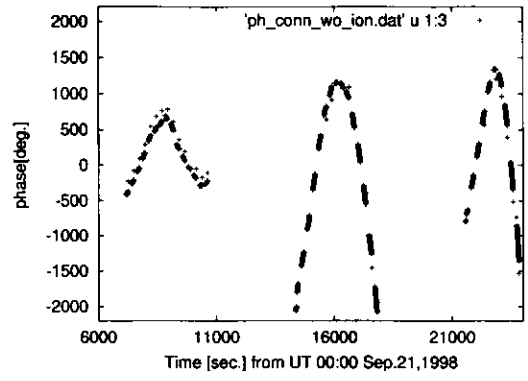

Figure 5.23: Residual fringe phase for the orbital element offset: MA+0.04 [deg]

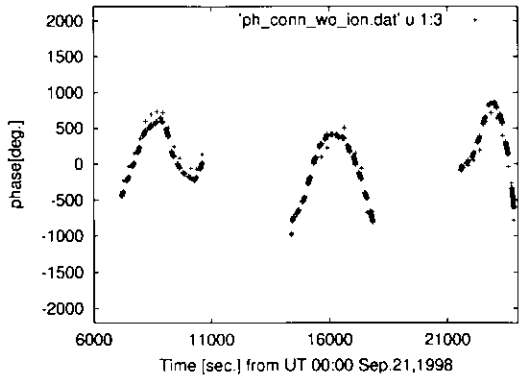

Figure 5.24: Residual fringe phase for the orbital element offset: Ω+0.08, MA+0.02 [deg.]

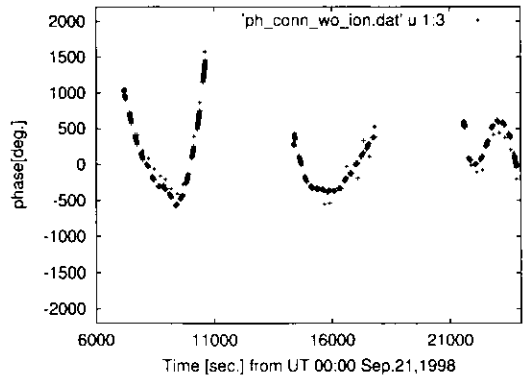

Figure 5.25: Residual fringe phase for the orbital element offset: Ω+0.08, MA-0.02 [deg.]

(Root-Mean-Square) in all observation periods is obtained as

$$RMS \;=\; 4.4 \quad degrees$$

On assumption that the cycle ambiguity of the phase is resolved and the atmospheric fluctuation is corrected by the multi-frequency VLBI, the RMS of 4.4 degrees corresponds to position error of 1.5m around the Moon for 360 km baseline such as Kashima-Mizusawa baseline. The error is smaller than compared with the position error of 30 m by the Doppler measurement [Konopliv et al., 1998].

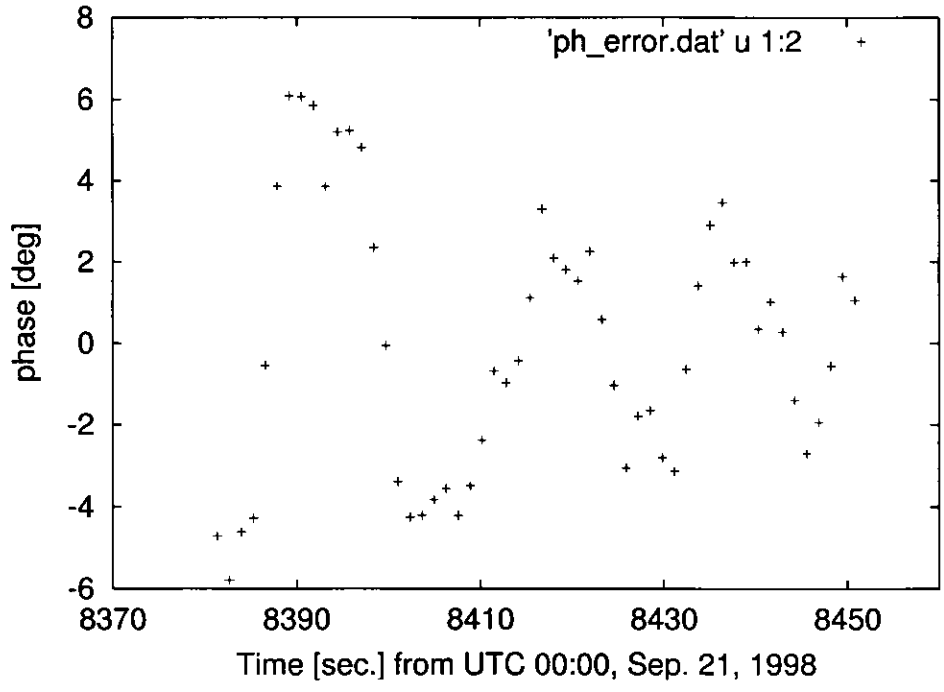

Figure 5.26: The short period variation of the residual fringe phase

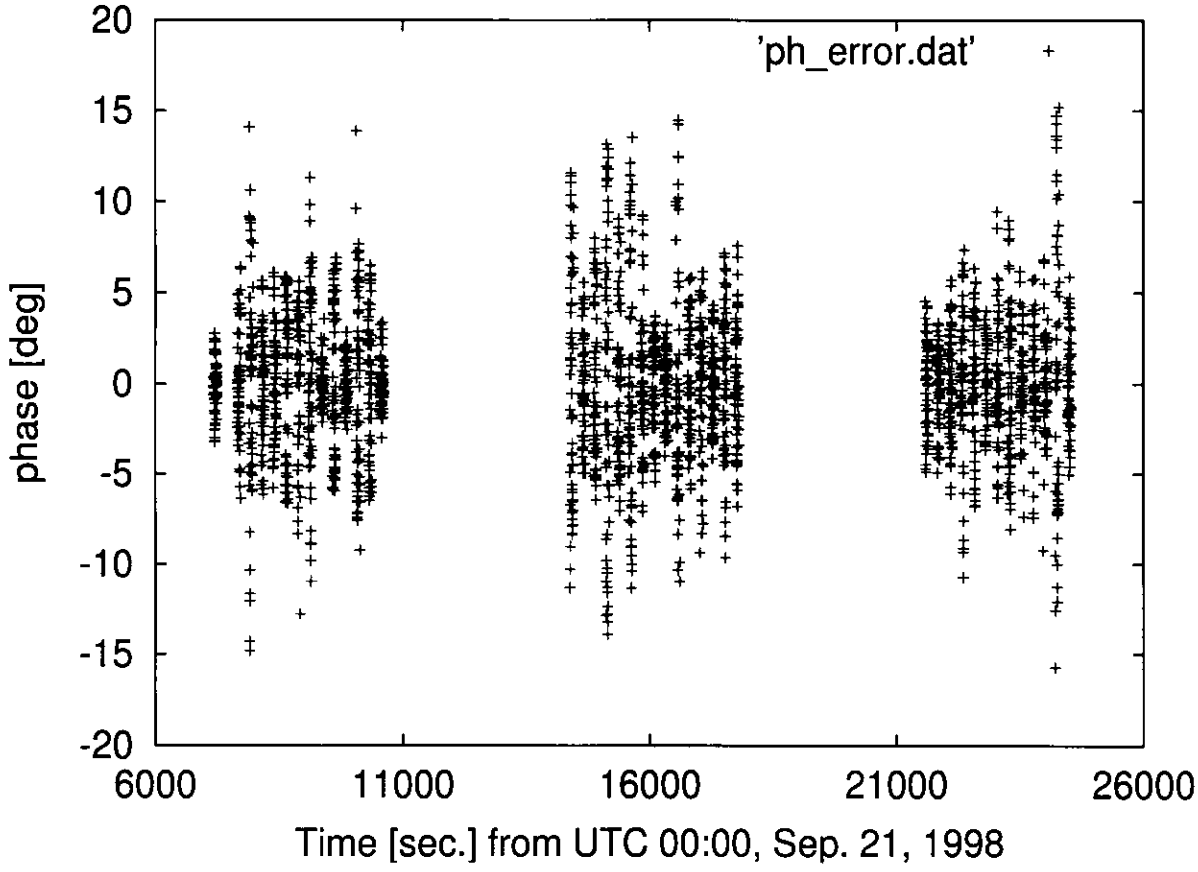

Figure 5.27: The short period variation of the residual fringe phase

Chapter 6

Conclusion and discussions

Wide band radio waves are received to measure the group delay in conventional VLBI, however a spacecraft usually transmits very narrow carrier waves to save electric and mass resources. Fringe rate or a group delay between two carrier waves has been only measured in the VLBI observation of a spacecraft, because the observed fringe phases contain the cycle ambiguity. It is well-known that the positioning accuracy is drastically improved if the cycle ambiguity is resolved from fringe phases and if the total fringe phases called the phase delays are obtained without the ambiguity. Kawano et al. [1994] and Hanada et al. [1999] made the idea on the method to resolve the ambiguity, that is, transmission of a few carrier waves from a spacecraft. There have remained, however, a lot of problems such as the algorithm to resolve the ambiguity and the realization of the complicated hardware and software.

In this thesis, the new VLBI method "Multi-frequency VLBI" was proposed, and the hardware and software system of a ground station were developed as a part of precise three-dimensional positioning of a spacecraft. In order to test the system, the preliminary experiment was carried out using NASA's Lunar Prospector.

The algorithm to resolve the ambiguity is completed for the developed equipment onboard SELENE by "Multi-frequency VLBI" method. It transmits three carrier waves in S-band and one in X-band. The two sets of group delays obtained from the three carrier waves in S-band are used to resolve the ambiguity of fringe phases for a highest RF (radio frequency) signal in S-band. After the phase delay (total fringe phase) is once determined from the two sets of group delays for S-band RF signal, it can predict the phase delay of the observed fringe phase for the RF signal of X-band from the relation of the phase proportional to the frequency. These processes to resolve the ambiguity and to obtain the phase delay can be applied under some conditions about the level of system noise, number of frequencies and the configuration of them, and the prediction accuracy of TEC. These conditions

are shown in this thesis. We also confirmed that the developed system was almost optimized to "Multi-frequency VLBI" for a spacecraft, and was satisfied all these conditions.

The preliminary experiment was carried out by using Lunar Prospector. Unfortunately it transmitted only one carrier wave, so that the test for resolving the ambiguity of the fringe phase could not be achieved. The residual fringe phases after the correction for the ionospheric delay have systematic variations of about 1000 deg. with period of about one hour. Since the period of the variations is same as the one of the orbit of about two hours, the variation suggests the existence of the error in the initial orbital elements. The residual fringe phases are re-calculated for small change of all orbital elements. The RMS of them decreased to about 360 deg. when the longitude of ascending node is slightly changed by 0.08 deg., but the residual fringe phases still have systematic variations with long periods. These variations is supposed to be caused by,

1) Reminder of the errors in the initial orbital elements,

2) Model errors of the lunar gravity fields used,

Although these long period variations can not be estimated in this experiment, they will be estimated in SELENE mission by multi-frequency VLBI. The short period variations of the residual fringe phases will remain even if the two variations are estimated. In this point of view, the short period variations mean the potential in an accuracy of the system. The RMS of the residual fringe phases averaged for several ten seconds reaches 4 deg., which corresponds to 1.5 m in the positioning error around the Moon. The target of the development would be to achieve the accuracy of 1.5m in positioning around the Moon. It is confirmed that the hardware and software system have enough availability to achieve the expected accuracy in "Multi-frequency VLBI".

The accuracy in Doppler frequency measurements was also improved. The effects caused by spin of a spacecraft and a phase pattern of an antenna have not been discussed so far. We pointed out that the spin and the phase pattern of the antenna considerably affect the Doppler measurements and these effects must be removed from observed Doppler frequency data for precise gravity estimation. The correction method for the effect was proposed, and its validity was confirmed by the observations of "NOZOMI".

All the multi-frequency VLBI and corrected Doppler frequency data will be combined with the big orbit and lunar gravity estimation software of GEODYN-II as three dimensional observables, and analyzed for three-dimensional positioning of the spacecraft.

Furthermore, the amount of recorded data is far less than that in conventional VLBI, because very narrow bandwidth signals are received. These two advantages

lead to a new applications and a new technique. The correction method for the spin effect will be available to any software to process Doppler data. On the other hand, small amount of recorded data makes real time VLBI in a tracking station possible. The total bandwidth to be recorded for a spacecraft would be a few hundred kHz in our Multi-frequency VLBI, so that all the sampled data can be sent to a reference station from slave stations via "INTERNET" and on-line data processing can be conducted with a small scale computer. Figure 6.1 shows concept of an Internet VLBI system. VLBI is a technique superior to detect a weak radio signal. This system can be applied to positioning of a spacecraft which can not transmit a signal high enough to make range or range rate observation [Yoshikawa et al., 2001], though the position error increases somewhat because of observation of one carrier wave. Thus, this technique will be widely used for tracking of a spacecraft in the near future.

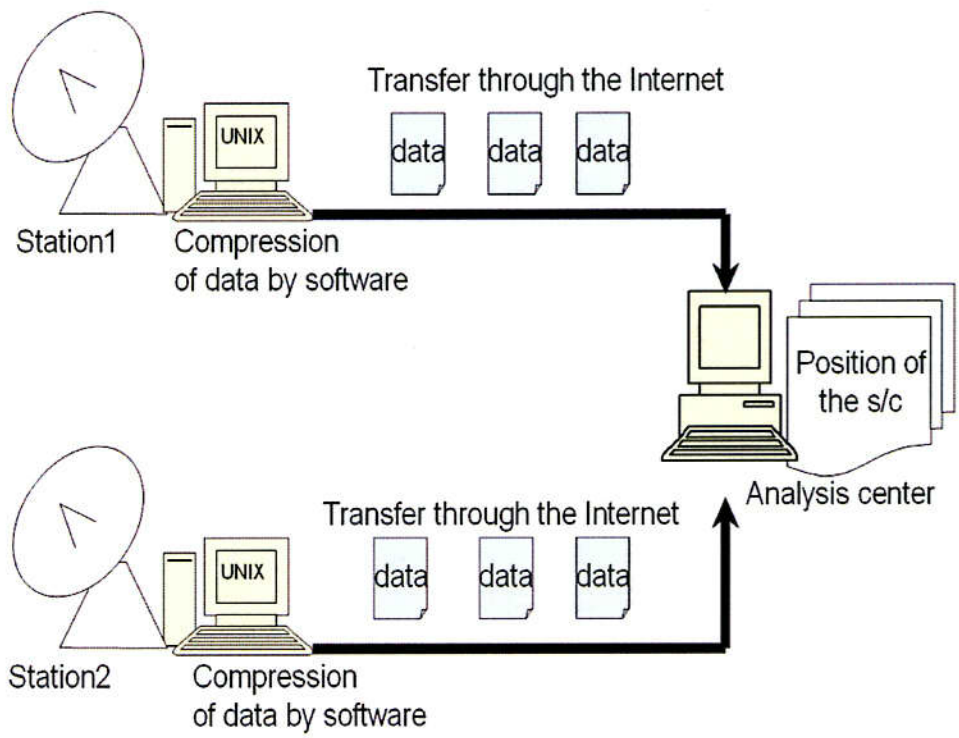

Figure 6.1: Concept of an Internet VLBI system

Acknowledgment

First of all, I would like to express my sincere gratitude to my supervisor Professor Nobuyuki Kawano of National Astronomical Observatory (NAO), Mizusawa for many helps and the guidance of my thesis. I started and continue to study VLBI methods under the direction for over four years. Without his helpful advice, my thesis cannot be completed.

I also would like to express an acknowledgement to Professor Hideo Hanada of NAO for the continuous encouragements and helpful suggestion. He has totally supported this thesis as a sub-supervisor.

I also thank Dr. Ping Jinsong of NAO for his help in writing this thesis and his beneficial suggestion. I always respect his stance to study, and it encourages me to make efforts.

I wish to thank Dr. Takahiro Iwata of National Space Development Agency for his helpful suggestion about the relay satellite of SELENE project. He has also supported the author mentally.

Dr. Koji Matsumoto kindly has helped me to handle GEODYN-II software. Dr. Takaaki Jike has supported data processing of QSO data by NAOCO.

Fortunately I could observe the Lunar Prospector at Kashima 34m-diameter antenna of the Communication Research Center (CRL) , Tsukuba 3.8m-diameter antenna of the Geographical Survey Institute (GSI) and Mizusawa 10m-diameter antenna of NAO by supports of Dr. Koyama of CRL, Dr. Fukuzaki of GSI and Mr. Kenzaburo Iwadate of NAO. I could also analyzed Doppler data of 'Nozomi' observed at Kagoshima Space Center of the Institute of Space and Astronautical Science (ISAS). I wish to thank to Drs. Takaji Kato and Tsutomu Ichikawa of ISAS.

The author wishes to express his appreciation to Dr. Hiroshi Imai of NAO, Mr. Fuyuhiko Kikuchi of NAO, Dr. Yoshiharu Asaki of ISAS and stuff members of RISE group in NAO.

I have to also thank to Mr. Toshiaki Ishikawa and Dr. Yoshiaki Tamura to reconstruct my VLBI software.

I am financially supported by the Research Fellowship of the Japan Society for

the Promotion of Science for young scientists (No. 03411).

Finally, I want to deeply acknowledge my family and friends of mine.

References

[Akim et al., 1966] Akim, E. L.,"Determination of the gravitational field of the Moon from the motion of the artificial lunar satellite 'Lunar-10' ", Dokl. Akad. Nauk SSSR 170, 799, 1966.

[Asaki et al., 1996] Asaki,Y., M. Saito, R. Kawabe, K. Morita, T. Sasao, "Phase compensaton experiments with the paired antenna method", Radio Sci., 31, 1615-1625, 1996.

[Bhaskaran 1995] Bhaskaran, s., "The Application of Noncoherent Doppler Data Types for Deep Space Navigation", NASA Code 315-90-81-41-06,TDA Progress Report 42-121 May 15, 1995.

[Binder et al., 1998] Binder A. B., "Lunar Prospector: Overview", Science, 281, 1475-1476, 1998.

[Border et al., 1982] Border, J. S., F. F. Donivan, S. G. Finley, C. E. Hildebrand, B. Moultier, and L. J. S.kjerve, "Determination spacecraft angular position with delat VLBI: The voygaer demonstration", AIAA-82-1471, 1982.

[Border et al., 1992] Border, J. S., W. M. Folkner, R. D. Kahn, and K. S. Zukor, "Precise Tracking of the Magellan and Pioneer Venus Orbiters by Same-Beam Interferometry, Part I: Data Accuracy Analysis", NASA Code 310-10-60-91-01, 992.

[Cameron 1997] A. G. W. Cameron, "The origin of the Moon and the single impact hypothesis V", Icarus, 126, 126-137, 15, 1997.

[Cameron and Ward 1976] Cameron, A. G. W., and W. R. Ward, "The origin of the Moon", Proc. Lunar Planet. Sci. Conf 7th, 120-122, 1976.

[Counselman et al., 1973] Counselman III, C. C., Hinteregger, H. F., King, R. W., and Shapiro, I. I., "Precision selenodesy via differential interferometry", Science, vol. 181, pp. 772-774, August 24, 1973.

Counselman III, C. C., Hinteregger, H. F., King, R. W., and Shapiro, I. I., "Lunar baselines and libration from differential VLBI observations of ALSEPs", The Moon, vol. 8, pp. 484-489, 1973.

[Edwards et al., 1990] Edwards, C. D., "Goldstone Intracomplex Connected Element Interferometry", TDA PR 42-101, January-March 1990, pp. 1-12, May 15, 1990.

[Edwards et al., 1991] Edwards,C., D. Rogstad, D. Fort, L. White, B. Iijima, "A Demonstration of Real-Time Connected Element Interferometry for Spacecraft Navigation", 1179 AAS 91-517, 1991.

[Edwards et al., 1992] Edwards, Jr., C., and J. S. Border, "Spacecraft-Spacecraft Very Long Baseline Interferometry, Part l: Error Modeling and Observable Accuracy" TDA PR 42-110, April-June 1992, 63-76, August 15, 1992.

[Ferrari et al., 1980] Ferrari, A. J., Sinclair, W. S., Sjogren, W. L., Williams,J. G. and Yoder, C. F.,"Geophysical parameters of the Earth-Moon system", J. Geophys. Res., 85, 3,939-3,951, 1980.

[Hanada et al., 1993] Hanada, H., M. Ooe, N. Kawaguchi, N. Kawano, S. Kuji, T. Sasao, S. Tsuruta, M. Fujishita, M. Morimoto, "Study of the Lunar Core by VLBI Observations of Artificial Radio Sources on the Moon", J. Geomag. Geoelectr., 45, 1405-1414, 1993.

[Hanada et al., 1999] Hanada, H., T. Iwata, N. Kawano, K. Heki, S. Tsuruta,T. Ishikawa, H. Araki, K. Matsumoto,Y. Kono, Y. Kaneko, M. Ogawa, Y. Iijima, Y. Koyama,M. Hosokawa, T. Miyazaki, Noriyuki Namiki, Arata Sengoku, Y. Fukuzaki,T. Ikeda, F. Fuke and RISE group, "Observation system of radio sources on the Moon by VLBI in SELENE project", Proceedings of the International Workshop on GEMSTONE, jun. 25-28, 126-130,1999.

[Hanada et al., 2000] Hanada, H., K. Heki, T. Iwata, M. Ooe, K. Matsumoto, H. Araki, and ILOM group, "Scientific goal of In-situ Orientation Measurement (ILOM)", ISTS 00-j-26p, 2000.

[Hanada et al., 2001] Hanada, H., T. Iwata, F. Fuke, "SELENE Instrument Interface Control Document(IICD)", B00-VRAD-001-01, 2001.

[Hartmann and Davis 1975] Hartmann, W. K., AND D. R. DAVIS "Satellite-sized planetesimals and lunar origin", Icarus, 24, 504-5, 1975.

[Hatch 1982] Hatch, R.R., "The synergism of GPS code and carrier measurements", Proc. 3rd Int. Symp. on "Satellite Doppler Positioning", New Mexico, 8-12 February, 1982, 1213-1231, 1982.

[Heki et al., 1999] Heki, K., K. Matsumoto and R. Floberghagen, "Three-dimensional tracking of a lunar satellite with differential very-long-baseline-interferometry", Adv. Space Res., 23, 1821-1824, 1999.

[Hinteregger et al., 1972] Hinteregger, H. F., I. I. Shapiro, D. S. Robertson, C. A. Knight, R. A. Ergas, A. R. Whitney, A. E. E. Rogers, J. M. Moran, T. A. Clark, and B. F. Burke, "Precision geodesy via radio interferometry", Science, 178, 396-398, 1972.

[Honma et al., 2000] Honma, M., T. Oyama, K. Hachisuka, S. Sawada-Satoh, K. Sebata, M. Miyoshi, O. Kameya, S. Manabe, N. Kawaguchi, T. Sasao, S. Kameno, K. Fujisawa, K. Shibata,T. Bushimata, T. Miyaji, H. Kobayashi, M. Inoue, H. Imai, H. Araki, H. Hanada, K. Iwadate, Y. Kaneko, S. Kuji, K. Sato, S. Tsuruta, S. Sakai, Y. Tamura, K. Horiai, T. Hara, K. Yokoyama, J. Nakajima, E. Kawai, H. Okubo, H. Osaki, Y. Koyama, M. Sekido, T. Suzuyama, R. Ichikawa, T. Kondo, K. Sakai, K. Wada, N. Harada, N. Tougou, M. Fujishita, R. Shimizu, S. Kawaguchi, A.Yoshimura, M. Nakamura, W. Hasegawa, S. Morisaki, R. Kamohara, T. Funaki, N.Yamashita, T. Watanabe, T. Shimoikura, M. Nishio,T. Omodaka, and A. Okudaira, "J-Net Galactic Plane Survey of VLBI Radio Sources for VLBI Exploration of Radio Astrometry (VERA)", Publ. Astron. Soc. Japan, 52, 631-643, 2000.

[Iwata et al., 2001] Iwata, T., M. Takahashi, N. Namiki, H. Hanada, N. Kawano, K. Heki, K. Matsumoto and T. Takano," Mission Instruments for Lunar Gravity Measurements using SELENE Sub-satellites", Journal of the Geodetic Society of Japan, 47, 1, 558-563, 2001.

[Kawaguchi et al., 1983] Kawaguchi, N., "Coherence loss and delay observation error in Very-Long-Baseline Interferometry", Journal of the Radio Research Laboratories, 30, 129, 58-87, March, 1983.

[Kawaguchi et al., 2000] Kawaguchi,N, M. Ono, H. Hirosawa, Z. Yamamoto, "HALCA Phase Transfer and Statistical Property of Atmospherical Phase Fluctuations", Advances in space science, 26, 617-623, 2000.

[Kawano et al., 1994] Kawano, N., S. Kuji, S. Tsuruta, K-H. Sato, K. Iwadate, H. Hanada, M. Ooe, N. Kawaguchi, H. Mizutani and A. Fujimura, "Development

of the artificial radio source on the Moon", J. Jap. Soc. Planet. Sci., 3, 159-169, 1994 (in japanese).

[Kawano et al., 2000] Kawano, N. H. Hanada, T. Iwata, Y. Koyama, "Differential VLBI Observations among a Lunar Orbiter, the Moon and a QSO", in International VLBI Service for Geodesy and Astrometry 2000 General Meeting Proceedings, edited by Nancy R. Vandenberg and Karen D. Baver, NASA/CP-2000-209893, 2000.

[King et al., 1974] King, R. W., Counselman III, C. C., Hinteregger, H. F., and Shapiro, I. I., "Study of lunar librations using differential very-long-baseline observations of ALSEPs", Rec. Adv. Sci., 8, . 431-438, 1974.

[Kiuchi et al., 1993] Kiuchi, H., S. Hama, J. Amagai, Y. Hanado, A. Kaneko and M. Imae, Proc. Int. Workshop for Reference Frame Establishment and Technical Development in Space Geodesy, 69-76, 1993.

[Kono et al., 2000] Kono, Y., H. Hanada, K. Iwadate, H. Araki, No. Kawano, Y. Koyama, Y. Fukuzaki, "Differential VLBI observation of the Lunar Prospector", in International VLBI Service for Geodesy and Astrometry 2000 General Meeting Proceedings, edited by Nancy R. Vandenberg and Karen D. Baver, NASA/CP-2000-209893, 2000.

[Kono et al., 2001] Kono, Y., J. Ping, T. Kato, T.Ichikawa and N. Kawano, "Analysis of short period variations of Doppler frequency caused by the spin of Mars spacecraft, Nozomi", IEICE Tran. communication, E84-B, No.6, 1971-1078, 2001 (in japanese).

[Konopliv et al., 1998] Konopliv A. B., A. B. Binder, L. L. Hood, A. B. Kucinskas, W. L. Sjogren and J. G. Williams, "Improved gravity field of the Moon from Lunar Prospector", Science, 281, 1476-1480, 1998.

[Konopliv et al., 2001] A. S. Konopliv, S. W. Asmar, E. Carranza, W. L. Sjogren and D. N. Yuan, "Recent gravity models as a result of the lunar prospector mission", Icarus, 150, 1-18, 2001.

[Marini 1972] Marini, J. W., "A test of the effect of satellite spin on two-way doppler range rate measurements IEEE trans. on Aerospace and Electronic System", AES-8, No3, 1972.

[Milani et al., 1996] Milani, A., M. Luise and F. Scortecci, "The lunar sub-satellite experiment of the ESA MORO mission: goals and performances", Planet. Space Science, 44, 10, 1065-1076, 1996.

[Namiki et al., 1999] Namiki, N. H. Hanada, T. Tsubokawa, M. Ooe, K. Heki, T. Iwata, M. Ogawa, T. Takano, and RSAT/VRAD/LALT mission groups, "Selenodetic experiments of SELENE:Relay subsatellite, differential VLBI and laser altimeter", Adv. Space Res., 23, 1817-1820, 1999.

[Pavlis et al., 1998] Pavlis, D. E., S. Luo, P. Dahiroc, J. J. McCarthy, and S. B. Luthke, "GEODYN-II,Operations Manual", 428 ., Greenbelt, Maryland, 1998.

[Ping et al., 2000] Ping, J., Y. Kono, A. Tsuchiya and N. Kawano, "Effects on Doppler freuency measurement due to the spin and a phase pattern of an antenna onboad a spacecraft", Jour. Geod. Soc. of Japan, 46, No.3, 187-202, 2000.

[Ping et al., 2001] Ping, J., F. Weischede, Y. Kono, H. Hanada and N. Kawano, "High frequency components in LP Doppler data", Artificial Satellites, 36, 1, 15-23, 2001.

[Rogers et al., 1981] Rogers, E. E. Alan, James M. Moran Jr., "Coherence limits for Very-Long-Baseline interferometry", IEEE Tran. Vol. IM-30, No. 4, Dec. 1981.

[Russell et al.,1981] Russell, C. T., P. J. Coleman Jr., B. E. Goldman, "Measurements of the Lunar Induced Magnetic Moment in the Geomagnetic Tail: Evidence For a Lunar Core?", Proc. Lunar Planet. Sci., 12B, 831-836, 1981.

[Sagdeyev et al., 1986] Sagdeev, R. Z., and Coauthors,"Overview of VEGA Venus balloon in situ meteorological measurements", Science, 231, 1411-1414, 1986.

[Sagdeyev et al.,1992] Sagdeyev, R.Z., Kerzhanovitch, V.V., Kogan, L.R., Kostenko, V.I., Linkin, V.M., Matveyenko, L.I., Nazirov, R.R., Pogrebenko, S.V., Struckov, I.A. Preston, R.A., Purcel, J., Hildebrand, C.E., Grishmanovskiy, V.A., Kozlov, A.N., Molotov, E.P., Blamont, J.E., Boloh, L., Laurans, G., Kaufmann, P., Galt, J., Biraud, F., Boischot, A., Ortega-Molina, A., Rosolen, C., Petit, G., Mezger, P.G., Schwartz, R., Ronnang, B.O., Spencer, R.E., Nicolson, G., Rogers, A.E.E., Cohen, M.H., Martiroysan, R.M., Moiseyev, I.G., and Jatskiv, J.S., "Differential VLBI measurements of the Venus atmosphere dynamics by balloons: VEGA project", Astron. and Astrophys. 254, 387-392, 1992.

[SELENE project team 2000] SELENE project team, "Scientific research in SELENE mission", Sep., 2000.

[Shiomi et al., 1984] Shiomi, T., S. Kozono, Y. Arimoto, S. Nagai, M. Isogai, "Precise orbit determination of a geosynchronous satellite by d-VLBI method", Journal of the Radio Research Laboratories, 30, 155, 185-198, June, 1984 (in Japanese).

[Sovers and Jacobs 1996] Sovers,C. J., Jacobs. C. S., "Observation model and Parameter partials for the JPL VLBI parameter estimation software 'modest' -1996", 1996.

[Takahashi et al., 2001] Takahashi, F., T. Kondo, Y. Takahashi, and Y. Koyama " Very Long Baseline Interferometer" 96-108, IOS Press, 2001.

[Takanezawa et al., 2000] Takanezawa, T., H. Hanada, S. Tsuruta, T. Tsubokawa, Y. Kono, and ILOM research group,"Design of ILOM telescope operating on the moon", ISTS2000-j-12, 1-5, 2000.

[Tsuchiya and Tsuji 1995] Tsuchiya, A. and H. Tsuji,"GPS Sokuryo-no Kiso", Japan Surveying Association, 11-170, 1995 (in Japanese).

[Yoshikawa et al., 2001] Yoshikawa, M., M. Sekido, N. Kawaguchi, K. Fujisawa, H. Hanada, Y. Kono, H. Hirabayashi, Y. Murata, S. Sawada-Satoh, K. Wajima, Y. Asaki, J. Kawaguchi, H. Ya-makawa, T. Kato, T. Ichikawa, and T. Ohnishi, "Present status and future problems of the orbit determination for Nozomi spacecraft", Proceedings of the 1st CRL TDC Symposium, Sep., 2001.

[Weischede et al., 1999] Weischede F., E. Gill, O. Montenbruck and R. Floberghagen, "Lunar Prospector orbit determination and gravity field modeling based on Weilheim 3-way Doppler measurements", in Proceedings of the 14th International Symposium on Space Flight Mechanics, Iguassu, Brazil, Feb. 8-12, 1999.

[Whitney 1974] Whitney, A. R., "Precision geodesyand astrometry via Very-Long-Baseline-Interferometry", Doctor thesis at the Massachusetts Institute of Technology, 1974.

Appendix A

Integrated Doppler measurement

The received frequency f_r is slightly shifted from the transmitted frequency f_0 by Doppler frequency δf_d, then the frequency is,

$$f_r = f_0 + \delta f_d \tag{A.1}$$

$$\delta f_d = -\frac{v}{c}, \tag{A.2}$$

where v is a line-of-sight velocity and c is the velocity of light. The received signal $x(t)$ at the ground station at time t is expressed is an ideal case as follows,

$$x(t) = e^{i2\pi f_r t}. \tag{A.3}$$

Amplitude is normalized for simple descriptions. Since an antenna onboard on the spacecraft has an antenna phase pattern, the transmitting phase is fluctuated at $\phi_a(t)$. Its received signal $x_p(t)$ is re-written as follows,

$$x_p(t) = e^{i2\pi f_r t + i\phi_a(t)}. \tag{A.4}$$

The measurements of the received frequency are mainly performed by several hardware which are a receiver, down-convertors, a PLL(Phase Lock Loop), a binary counter and a register of the binary counter. A block diagram of the integrated Doppler measurement is shown in Figure A.1. The received signal is frequency-converted by several down-converters. Here a case that the system has a one down-converter is considered to simplify descriptions. The received signal $x'_p(t)$ after the down-converter is written as

$$x'_p(t) = e^{i2\pi(f_r - f_l)t + i\phi_a(t) + i\phi_l}, \tag{A.5}$$

where f_l and ϕ_l are the frequency and the initial phase of the local oscillator of the down-converter, respectively. The down-converted signal is inputted to the PLL

which multiply the phase of the signal by a factor of n_m. The signal $x_p''(t)$ passed through the PLL is given as,

$$x_p''(t) = e^{i2\pi n_m(f_r - f_l)t + in_m\phi_a(t) + in_m\phi_l}. \tag{A.6}$$

This signal is inputted to the binary counter. The binary counter counts the number of the inputted wave. When the number of the wave is counted by the counter from $t = 0$ to $t = T$, the number $N_{bc}(T)$ is given as follows,

$$\begin{aligned} N_{bc}(T) &= \int_0^T \frac{1}{2\pi}\frac{d}{dt}\{2\pi n_m(f_r - f_l)t + n_m(\phi_a(t) + \phi_l)\}dt + N_{bc}(0) \quad \text{(A.7)} \\ &= \int_0^T n_m\{f_r - f_l + \frac{1}{2\pi}\dot{\phi}_a(t)\}dt + N_{bc}(0), \quad \text{(A.8)} \end{aligned}$$

where $N_{bc}(0)$ is the initial value of the counter at $t = 0$, $\dot{\phi}_a(t)$ is the time derivative of $\phi_a(t)$, and ϕ_l is assumed to be constant during the observation.

If the Doppler frequency is constant during the twice integration time, the number $N_{bc}(2T)$ for the next integration time is given as,

$$N_{bc}(2T) = \int_T^{2T} n_m\{f_r - f_l + \frac{1}{2\pi}\dot{\phi}_a(t)\}dt + N_{bc}(T). \tag{A.9}$$

The Doppler frequency δf_d is obtained, subtracting Equation (A.9) from Equation (A.8),

$$\delta f_d = \left[\frac{N_{bc}(2T) - N_{bc}(T)}{n_m T}\right] + (f_l - f_0) - \frac{1}{2\pi T}\int_T^{2T} \dot{\phi}_a(t)dt. \tag{A.10}$$

As mentioned in Chapter 2, the Doppler frequency variation $\dot{\phi}_a(t)/2\pi$ is described by harmonics of the spin frequency f_{spin} as follows,

$$\frac{\dot{\phi}_a(t)}{2\pi} = \sum_n A_n \cos(2\pi n f_{spin} t + \theta_n), \tag{A.11}$$

where A_n and θ_n are the amplitude and the initial phase for the n-th harmonics, respectively. The third term $\delta f_{a,n}$ of Equation (A.10) for n-th harmonics is given as,

$$\delta f_{a,n} = -\left[\frac{\sin(\pi n f_{spin} T)}{(\pi n f_{spin} T)}\right] A_n \cos(3\pi n f_{spin} T + \theta_n). \tag{A.12}$$

Thus, the Doppler frequency variations due to the antenna phase pattern and the spin are included in the Doppler frequency in spite of the integration.

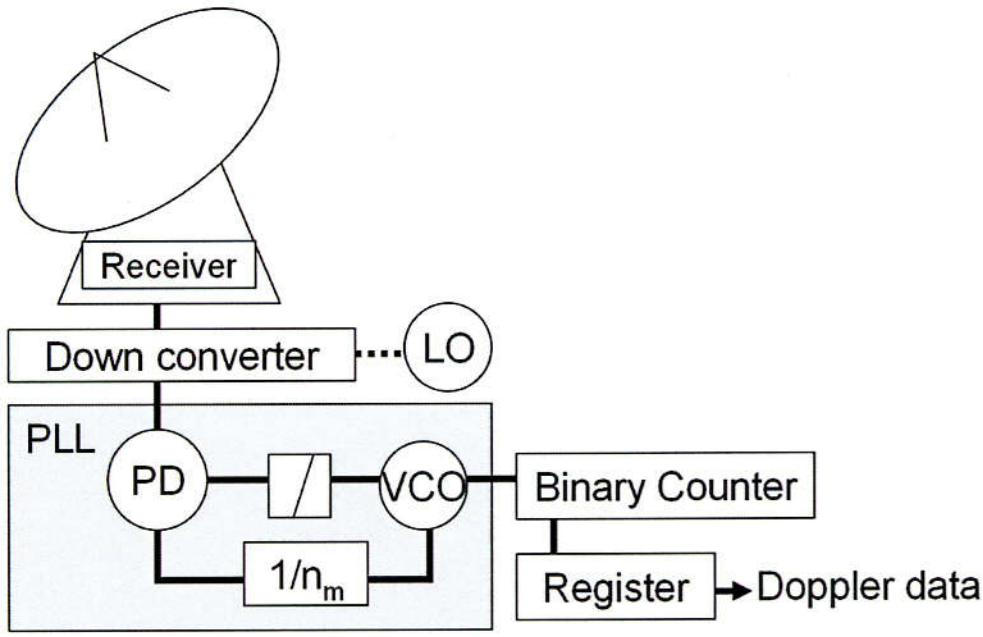

Figure A.1: Block diagram of integrated Doppler system